RADIO TO GAMMA-RAY EMISSION FROM SHELL-TYPE SUPERNOVA REMNANTS: PREDICTIONS FROM NON-LINEAR SHOCK ACCELERATION MODELS

Matthew G. Baring
Laboratory for High Energy Astrophysics
NASA Goddard Space Flight Center
Greenbelt, MD 20771, U.S.A.

Donald C. Ellison and Stephen P. Reynolds
Department of Physics
North Carolina State University
Raleigh, NC 27695, U.S.A.

Isabelle A. Grenier and Philippe Goret
EUROPA-Université Paris, Paris VII
and DAPNIA/Service d'Astrophysique
Centre d'Etudes de CE-Saclay
Gif-sur-Yvette, France

Accepted for publication in the Astrophysical Journal, Vol 513, March 1999.

RADIO TO GAMMA-RAY EMISSION FROM SHELL-TYPE SUPERNOVA REMNANTS: PREDICTIONS FROM NON-LINEAR SHOCK ACCELERATION MODELS

Matthew G. Baring[1]
Laboratory for High Energy Astrophysics, Code 661,
NASA Goddard Space Flight Center, Greenbelt, MD 20771, U.S.A.
baring@lheavx.gsfc.nasa.gov

Donald C. Ellison & Stephen P. Reynolds
Department of Physics, North Carolina State University,
Box 8202, Raleigh NC 27695, U.S.A.
don_ellison@ncsu.edu, steve_reynolds@ncsu.edu

and

Isabelle A. Grenier & Philippe Goret
Service d'Astrophysique, CEA, DSM, DAPNIA,
Centre d'Etudes de Saclay, 91191 Gif-sur-Yvette, France
isabelle.grenier@cea.fr, goret@sapvxg.saclay.cea.fr

ABSTRACT

Supernova remnants (SNRs) are widely believed to be the principal source of galactic cosmic rays, produced by diffusive shock acceleration in the environs of the remnant's expanding blast wave. Such energetic particles can produce gamma-rays and lower energy photons via interactions with the ambient plasma. The recently reported observation of TeV gamma-rays from SN1006 by the CANGAROO Collaboration, combined with the fact that several unidentified EGRET sources have been associated with known radio/optical/X-ray-emitting remnants, provides powerful motivation for studying gamma-ray emission from SNRs. In this paper, we present results from a Monte Carlo simulation of non-linear shock structure and acceleration coupled with photon emission in shell-like SNRs. These non-linearities are a by-product of the dynamical influence of the accelerated cosmic rays on the shocked plasma and result in distributions of cosmic rays which deviate from pure power-laws. Such deviations are crucial to acceleration efficiency considerations and impact photon intensities and spectral shapes at all energies, producing GeV/TeV intensity ratios that are quite different from test particle predictions. The Sedov scaling solution for SNR expansions is used to estimate

[1]Universities Space Research Association

important shock parameters for input into the Monte Carlo simulation. We calculate ion (proton and helium) and electron distributions that spawn neutral pion decay, bremsstrahlung, inverse-Compton, and synchrotron emission, yielding complete photon spectra from radio frequencies to gamma-ray energies. The cessation of acceleration caused by the spatial and temporal limitations of the expanding SNR shell in moderately dense interstellar regions can yield spectral cutoffs in the TeV energy range that are consistent with Whipple's TeV upper limits on those EGRET unidentified sources that have SNR associations. Supernova remnants in lower density environments generate higher energy cosmic rays that produce predominantly inverse Compton emission observable at super-TeV energies, consistent with the SN1006 detection. In general, sources in such low density regions will be gamma-ray dim at GeV energies.

Subject headings: acceleration of particles — cosmic rays — supernova remnants — radiation mechanisms: non-thermal — gamma-rays: theory — ISM: individual (IC 443)

1. INTRODUCTION

It is widely believed that supernova remnants (SNRs) are the primary sources of cosmic-ray ions and electrons up to energies of at least $\sim 10^{15}$ eV, where the so-called *knee* in the spectrum marks a deviation from almost pure power-law behavior. Such cosmic rays are presumed to be generated by diffusive (also called first-order Fermi) acceleration at the remnants' forward shocks. These cosmic rays can generate gamma rays via interactions with the ambient interstellar medium, including nuclear interactions between relativistic and cold interstellar ions, by bremsstrahlung of energetic electrons colliding with the ambient gas, and inverse Compton (IC) emission off background radiation. Rudimentary models of gamma-ray production in supernova remnants involving nuclear interactions date back to the early work of Higdon & Lingenfelter (1975) and Chevalier (1977), and later Blandford & Cowie (1982). These preceded the first tentative associations of two COS-B gamma-ray sources (Pollock 1985) with the remnants γ Cygni and W28. The study of gamma-ray SNRs remained quietly in the background until the ground-breaking observational program of the EGRET experiment aboard the Compton Gamma Ray Observatory (CGRO). This provided a large number of unidentified sources in the super-50 MeV band, seen both in and above the galactic plane, which led to the suggestion (e.g. Sturner & Dermer 1995) of a possible supernova origin (see Mukherjee, Grenier, & Thompson 1997 for a discussion of this population). A handful of these EGRET sources have significant associations with relatively young SNRs (Esposito et al. 1996).

Following the EGRET advances, the modeling of gamma-ray emission from supernova remnants began in earnest with the paper of Drury, Aharonian, & Völk (1994), who computed (as did Naito and Takahara 1994) the photon spectra expected from the decay of neutral pions generated

in collisions of shock-accelerated ions with those of the interstellar medium (ISM). These works assumed that the ions have power-law spectra extending to $\sim 10^{14}$ eV or beyond. Since then, a number of alternative models examining other (i.e. electromagnetic) radiation processes have been presented. These include the work of Gaisser, Protheroe, & Stanev (1998) and Sturner et al. (1997), who did not treat non-linear effects from efficient particle acceleration, and the recent analysis of Berezhko & Völk (1997), who solved the fully momentum-dependent diffusion-convection equation and included non-linear effects, but treated ion injection in a parametric fashion. Here, we include the injection and acceleration of both ions and *thermal electrons* in non-linear shocks and describe cases where emission from energetic electrons is likely to dominate ion emission, as expected in low density regions where flat inverse Compton gamma-ray components become important. This fact was exploited by Mastichiadis & de Jager (1996) and Pohl (1996) to propose that SN1006 should exhibit such a component, a timely prediction given the subsequent report of a spatially-resolved (to the NW rim of the shell) detection of SN1006 by the CANGAROO experiment (Tanimori et al. 1997) at energies above 1.7 TeV. Non-linear spectral models of diffusive shock acceleration that include the back-reaction of the accelerated particles on the shock structure do not produce exactly power-law particle distributions, and generate electron and ion spectra which differ considerably from each other. Central to predictions of photon emission from SNR shock acceleration are the details of this spectral curvature, the maximum energies of the ions and electrons, their relative abundances, and the enhancements of density of heavy ions relative to protons caused by non-linear shock modification.

In this paper, we calculate *both* the ion and electron spectra resulting from *non-linear*, cosmic ray-modified SNR shocks and, using these, compute photon emission over the entire range of the electromagnetic spectrum from radio waves to gamma-rays. The non-linear shock model we use is described in detail in Ellison, Jones, & Reynolds (1990), Jones & Ellison (1991) and Ellison, Baring, & Jones (1996), and consists of a Monte Carlo simulation of the transport of particles through a steady-state, plane-parallel shock. The chief advantage this technique has over other non-linear shock models is that particle injection can be treated in a largely self-consistent fashion, and this feature has been tested against particle distributions observed at the Earth's bow shock (Ellison, Möbius, & Paschmann 1990) and in linear applications to interplanetary shocks (e.g. Baring, et al. 1997). The non-linear aspects of shock acceleration have been shown to be consistent with the spectral index and curvature inferred for relativistic electrons emitting radio synchrotron radiation in the Tycho and Kepler remnants (Reynolds & Ellison, 1992), and have very recently been shown to produce the observed cosmic ray chemical composition if normal (i.e. cosmic abundance) ISM gas and dust are accelerated in smoothed SNR shocks (Meyer, Drury, & Ellison 1997; Ellison, Drury, & Meyer 1997). By imposing mass, momentum, and energy conservation, we obtain a steady-state solution which self-consistently includes *ion* injection and acceleration and simultaneously yields the average shock structure and complete particle distribution functions. As with previous applications of our Monte Carlo technique, we assume that the scattering properties of the particles, thermal and energetic, obey simple scattering laws, in accord with heliospheric shock observations and results of plasma simulations. Via this prescription, our ion injection model embodies the essential plasma

properties at least as far as gross observables are concerned.

A new feature included here is a parametric model for *thermal electron* injection and suprathermal scattering. With two additional parameters, we calculate the complete distributions and absolute acceleration efficiencies of both ions and electrons in shocks capable of accelerating particles to TeV and super-TeV energies. This allows us to simultaneously describe photon emission from ions and electrons, over a wide range of photon energies, in a single shock with a single set of environmental and shock parameters. The electron-to-proton ratio at energies above $\sim$ 1 GeV depends strongly on these parameters and, in conjunction with multi-wavelength observations of SNRs, permits us to constrain these parameters. Our model spectra include synchrotron radiation, bremsstrahlung, inverse Compton scattering off the cosmic microwave background, and the decay of neutral pions produced in collisions of nucleons. In this latter nuclear process, we find that contributions from accelerated alpha particles are comparable to those from protons despite a cosmic abundance ratio of ~ 0.1, mostly since heavier elements are accelerated more efficiently by the Fermi mechanism in non-linear shocks.

The steady-state Monte Carlo technique precludes an exact dynamical description for a remnant as it expands into the ISM. To model such time dependence, we use standard Sedov solutions for SNR evolution in homogeneous media to estimate the shock speed $V_{\rm sk}$ and radius $R_{\rm sk}$ at any age. We then calculate the maximum energy $E_{\rm max}$ to which particles can be accelerated according to the well-known Fermi acceleration formula resulting from the diffusion approximation. Our best-approximation steady-state model is then obtained by including an upstream free escape boundary set by the diffusion length of the particles with $E_{\rm max}$. In this way we incorporate into our Monte Carlo simulation the most essential aspects and consequences of time-dependence in SNR expansions: $V_{\rm sk}$ and $E_{\rm max}$ are the two key quantities for any non-linear model of acceleration in expanding SNR shocks. This simple picture using the Sedov evolution does not account for the energy from cosmic rays escaping upstream from the expanding shock: hence a real SNR shock will expand less rapidly than the Sedov solution predicts. In addition, our picture omits adiabatic gains/losses interior to the shock, which can be influential in determining $E_{\rm max}$ (Berezhko & Völk 1997). Despite these shortcomings, we argue that this hybrid technique overcomes the major deficiencies of our steady-state and plane shock approximations and contains the essential non-linear effects that are expected in efficient particle acceleration. Work is currently in progress (Berezhko & Ellison 1998, in preparation) to detail the differences between this steady-state, planar Monte Carlo model and the time-dependent, spherical SNR shock model of Berezhko, Yelshin, & Ksenofontov (1996). Preliminary results suggest the differences are small.

We report here the parameters required for the maximum particle energies obtained by diffusive shock acceleration to be consistent with current upper limits from the Whipple and HEGRA atmospheric Čerenkov telescopes on remnants with putative EGRET source associations. We find that maximum particle energies of a few TeV for ISM densities near ~ 1 proton cm^{-3} are not inconsistent with Fermi acceleration at supernova remnant shocks. At the same time, our models predict relatively weak emission in the 100 MeV–10 TeV range for low upstream densities, $\lesssim 1\,{\rm cm}^{-3}$, which

poses no problem if the unidentified EGRET sources catalogued by Esposito et al. (1996) are not connected with shell emission. This scenario permits acceleration to much higher energies, though we find it difficult, in accord with many previous papers, to accelerate up to the *knee* in the cosmic ray spectrum at $\sim 10^{15}$ eV without resorting to unrealistically low ISM densities. The lower density models may be most appropriate to sources out of the galactic plane like SN1006, where super-50 TeV electrons are inferred from both X-ray (presumably synchrotron) and TeV gamma-ray (probably inverse Compton) observations (see Koyama et al. 1995 and Tanimori et al. 1998, respectively). Taken together, these complementary results illustrate a general property of our modeling, and also of non-linear shock acceleration theories in general, namely an anti-correlation between the EGRET band flux and the maximum energy of cosmic ray acceleration. We also produce broad-band emission spectra for a range of parameters and specifically compare our results to observations of IC 443. In the gamma-ray band, we have little trouble reproducing the spectral index and flux of the EGRET source 2EG J0618+2234 provided that inverse Compton emission is relatively unimportant, a conclusion reached by Gaisser, Protheroe, & Stanev (1998). However, we find that the unusually flat radio spectrum of IC 443 is *not* well modeled with standard Fermi acceleration without resorting to extremely inefficient electron scattering. If this flat radio spectrum cannot be attributed to thermal contamination or free-free absorption, then it is probable that some source other than particle acceleration at the SNR blast wave is responsible for the photon emission.

The results and discussions of this paper identify a number of important issues that should form focuses of future theoretical research, including the radial/angular extent of X-ray and gamma-ray emission, the modeling of flat spectrum radio sources, spatial variations in radio, X-ray and gamma-ray spectral indices, identifying which physical processes are responsible for the non-thermal X-ray and gamma-ray flux, the role of magnetic-field obliquity around the shell, the e/p ratio and a more complete description of electron injection, and cosmic ray abundances and production up to the knee. Efforts in this direction should anticipate the expected improvements in the near future in sensitivity and angular resolution of ground-based and satellite X-ray and gamma-ray telescopes.

2. FERMI ACCELERATION IN SUPERNOVA REMNANTS

2.1. The Monte Carlo Calculation of Fermi Acceleration

Apart from the electron injection model introduced here, the Monte Carlo simulation we use to model the diffusive shock acceleration of ions has been described in detail elsewhere (e.g. Jones & Ellison 1991; Baring, Ellison, & Jones 1993; Ellison, Baring, & Jones 1996). It is a kinematic model, closely following Bell's (1978) approach to diffusive acceleration, where the simulation is used to calculate, in effect, solutions to a Boltzmann equation for particle transport involving a collision operator, without making any assumption concerning the isotropy of particle distributions. Particles are injected at a position far upstream and allowed to convect into the shock (i.e.

mimicking the interstellar medium exterior to a remnant that is overtaken by the blast wave), diffusing between postulated scattering centers (presumably magnetic irregularities in the background plasma and self-generated turbulence) along the way. As particles diffuse between the upstream and downstream regions, they continually gain energy (for a simulation example, see Fig. 3 of Baring, Ellison, & Jones 1994) in accord with the Fermi mechanism. Our models here are restricted to infinite plane, steady-state, *parallel* shocks where the angle Θ_{Bn} between the upstream magnetic field and the shock normal is assumed to be zero everywhere. As detailed below, the maximum linear scale in the shock, the diffusion length of the highest-energy particles, is always less than 1/4 of the shock radius, R_{sk}, and almost all of the flow deceleration (in the shock frame) occurs within $\Delta R/R_{sk} < 0.1$. In a Sedov spherical blast wave, post-shock expansion and velocity gradients can also affect the particle distribution, causing adiabatic losses (Berezhko 1996); we expect these effects to be confined to the highest-energy particles, so that the maximum energies we obtain at later times may be slightly inaccurate. However, at earlier times the diffusion length scale is even less than $0.1R_{sk}$, and the plane-shock approximation should be accurate. The non-linear Monte Carlo technique has been generalized to oblique shock geometry (i.e. shocks with $\Theta_{Bn} > 0°$; e.g. Ellison, Baring, & Jones 1996), and shock obliquity undoubtedly plays an important role in supernova remnant considerations, for example in the work of Fulbright & Reynolds (1990) and Reynolds (1996); treatment of it is deferred to future work.

2.1.1. Particle Scattering

We assume that particles of speed v (measured in the local plasma frame) scatter isotropically in this plasma frame with an exponential distribution about a collision time $t_c = \lambda/v$ for mean free paths λ. The particles make large angle scatterings, mimicking diffusion in strongly turbulent plasmas where $|\delta\mathbf{B}|/|\mathbf{B}| \sim 1$. Such strong turbulence is commonly observed in heliospheric shock environments (e.g. Hoppe et al. 1981; Tsurutani, Smith, & Jones 1983; Balogh et al. 1993), and has been inferred near young supernova remnants (Achterberg, Blandford, & Reynolds 1994). Note that Ellison, Baring, & Jones (1996) observed that the acceleration process was only weakly dependent on the type of the scattering as long as Θ_{Bn} is not close to 90°: pitch-angle diffusion (small-angle scattering) and large-angle scattering generated similar particle distributions for a wide range of shock parameters. In the upstream region, the scattering centers move at a speed, v_A relative to the bulk flow speed $u(x)$, where $v_A = B/\sqrt{4\pi n_p m_p} \simeq 2.2\,(B/\mu\mathrm{G})(n_p/\mathrm{cm}^{-3})^{-1/2}$ km s^{-1}, is the Alfvén speed (here, B is the magnetic field, n_p is the proton number density, and m_p is the proton mass. Thus, the scattering is inelastic in the plasma frame (unless particle speeds far exceed the Alfvén speed) and energy can be transferred from the superthermal population to the background thermal gas. This effect is discussed in more detail in Section 2.1.3.

We adopt a phenomenological mean free path to describe the complicated plasma microphysics in a very simple prescription. Specifically, we take the scattering mean free path parallel to the mean magnetic field, λ_i, of *all* ions, thermal and super-thermal, including both protons and heavier

species, to be

$$\lambda_i = \eta r_g \,, \tag{1}$$

where $r_g = pc/(QeB)$ is the gyroradius and η is a constant, independent of ion species, energy, and position relative to the shock. Here, p is the particle momentum measured in the local plasma frame, Q is the charge number, and $-e$ is the electronic charge. The *spatial diffusion coefficient* along the field is then $\kappa = \lambda_i v/3$. Note that for shocks of speed V_{sk}, κ/V_{sk} approximates the upstream diffusion length scale. The minimum value of η is unity, the so-called Bohm limit, where diffusion is comparable along and perpendicular to the mean magnetic field: this corresponds to strong turbulence, $|\delta\mathbf{B}|/|\mathbf{B}| \sim 1$. The aptness of a power-law prescription, $\lambda_i \propto p^\alpha$, to shocked plasma environments is supported by particle observations at the Earth's bow shock (where $1/2 < \alpha < 3/2$, Ellison, Möbius, & Paschmann 1990), deductions from ions accelerated in solar particle events (Mason, Gloeckler, & Hovestadt 1983, where $1/2 < \alpha < 4/5$), and also from turbulence in the interplanetary magnetic field (Moussas et al. 1992). On the theoretical side, plasma simulations (Giacalone, Burgess, & Schwartz 1992) suggest a mean free path obeying $\lambda_i \propto p^\alpha$ with $\alpha \sim 2/3$. We believe that the assumption of $\lambda_i \propto p$ is simple, physically realistic, and representative of the Fermi acceleration process.

2.1.2. Electron Scattering and Injection Model

The injection of thermal electrons into the Fermi process is poorly understood. This is a prominent problem in astrophysics in general, and for supernova remnants in particular, given few or no palpable radiative signatures of energetic ions. In contrast, evidence of non-thermal electrons in remnants is common, including ubiquitous observations of radio synchrotron emission, and now detections of non-thermal X-rays (Koyama et al. 1995; Keohane et al. 1997; Allen et al. 1997) from three SNRs and the report of gamma-rays from SN1006 (Tanimori et al. 1997, 1998). While protons resonantly create and scatter off Alfvén waves at all energies from thermal upwards, and so have a ready supply of magnetic turbulence for providing spatial diffusion (for example see Lee's 1982 model of the Earth's bow shock), it is unclear whether there is a significant presence in shocked plasmas of the much shorter wavelength waves, i.e. whistlers, that resonate with thermal and suprathermal electrons. Levinson (1992, 1996) included whistlers in his quasi-linear theory description of wave generation and electron diffusion and acceleration at kinetic energies between $\sim$ 5 keV and 3 MeV. Levinson's model therefore may not describe electron injection from truly thermal energies in the case of old SNRs, where the plasma temperatures are well below 5 keV, but may apply to younger remnants with shock velocities of several thousand km s^{-1}. Galeev, Malkov & Völk (1995) have suggested that oblique, lower hybrid waves can be excited by ion beams and that these waves can then accelerate thermal electrons. However, this mechanism remains highly speculative and is restricted, in any case, to quasi-perpendicular shocks. Hence, below a few keV, the situation remains inconclusive, being complicated by the fact that whistlers can be strongly damped in warm or hot plasmas; Alfvén modes usually escape this fate. We note that the

low energy electron injection issue can be circumvented in alternative scenarios, such as that put forward by Ellison, Jones, & Ramaty (1990) and Chan & Lingenfelter (1993), where the decay of nucleosynthetic material provides an injection of MeV leptons into the Fermi process.

Our electron model assumes that, at high electron momenta, the electron mean free path λ_e is proportional to the electron gyroradius, exactly as in equation (1). At lower momenta, however, we modify equation (1) by introducing an arbitrary momentum, $p_{\rm crit}$ [or, equivalently, kinetic energy $E_{\rm crit} = \sqrt{p_{\rm crit}^2 c^2 + (m_e c^2)^2} - m_e c^2$], below which electrons have a constant mean free path, i.e.

$$\lambda_e = \begin{cases} \eta\, r_{g,e}(p_{\rm crit}) \;=\; \text{constant}\,, & p \le p_{\rm crit} \\ \eta\, r_{g,e}(p)\,, & p > p_{\rm crit}\ , \end{cases} \tag{2}$$

where $r_{g,e}(p) = pc/(eB)$ is the electron gyroradius for the electron momentum p. Keeping λ_e constant below $p_{\rm crit}$ is one way of describing inefficient scattering at low energies. In addition, we inject electrons, not with typical upstream thermal energies (e.g. $kT \sim$ few eV) or downstream Rankine-Hugoniot temperatures, but at some fraction of the *downstream proton* temperature $T_{\rm p,DS}$ which results from the thermalization over the *subshock velocity jump*: $kT_{\rm p,DS} \sim m_{\rm p}(V_{\rm sub} - u_2)^2$, where $V_{\rm sub}$ is the flow speed at the subshock, $u_2 = V_{\rm sk}/r$ is the downstream flow speed, and r is the overall shock compression ratio. In plasma shocks, electrons are in fact heated at the subshock by plasma processes (e.g. Cargill & Papadopoulos 1988) such as electric fields induced by particle motions and electron-proton charge separations, Given that this heating takes place mainly at the subshock, which can be much weaker than the overall shock (e.g. $r_{\rm sub} \sim 2.5$, see Figure 4 below), we parameterize the electron heating by setting the downstream thermal electron temperature, $T_{\rm e,DS}$, to

$$\frac{3}{2}\, k\, T_{\rm e,DS} \;=\; f_{\rm e}\, \frac{1}{2}\, m_{\rm p}\, (\Delta V_{\rm sub})^2\ , \tag{3}$$

where $\Delta V_{\rm sub} = V_{\rm sub} - u_2$. In principle, the parameter $f_{\rm e} \le 1$ can be varied to match X-ray observations. In practice, we inject electrons in our simulation far *upstream* with a temperature $T_{\rm e,inj} \equiv T_{\rm e,DS}$, since the energy the electrons gain in their first crossing of the shock from compression is generally much less than $k\,T_{\rm e,DS}$. This prescription results in electron temperatures consistent with those deduced from observations of thermal X-ray emission in SNRs (for a recent collection of observational studies, see Zimmermann, Trümper, & Yorke 1996). Note that we treat electrons as test particles and do not include any influence they have on the shock dynamics. The relaxation of this approximation is deferred to future work, though electrons are dynamically unimportant for most of our models and likely to be so for most astrophysical conditions.

We believe that equations (2) and (3) constitute a simple model for electron injection that addresses the most salient features of Levinson's (1992) developments, without adding unnecessary parameters whose determination is beyond current observational capabilities. In particular, equation (2) models the expected inefficiency of electron scattering compared to ions at thermal and suprathermal energies. Our prescription guarantees, through the parameters $p_{\rm crit}$ and $f_{\rm e}$, acceptable injection efficiencies for thermal electrons in smoothed non-linear shocks, primarily because

they need to sample long length scales in order to experience the greatest possible compressive power of the shock. [1]

Since this is the first presentation of our electron injection model, we give a simple example to illustrate its basic properties. Using the artificial shock flow profile shown in Figure 1, we inject and accelerate electrons and protons keeping the shock profile fixed, i.e. we are doing a test-particle example and do not attempt to find a self-consistent solution. Both electrons and protons are injected at $x = 0$ in this test case with δ-function distributions at 1 keV; in our self-consistent models addressed later, we always inject particles far upstream. The protons are scattered using equation (1) and the electrons using equation (2). The densities in scalar momentum space, $f(|\mathbf{p}|)$, are shown in Figure 2, where we plot $|\mathbf{p}|^{2.5} f(|\mathbf{p}|)$ to flatten the spectra. The top curve (solid line) is the proton distribution, while the lower dashed curve is the electron distribution with $p_{\rm crit} = 0$ (i.e. for this example, electrons and protons have identical functions for their mean free paths). From test-particle Fermi acceleration theory (e.g. Blandford & Ostriker 1978), we expect that

$$f(|\mathbf{p}|)\, d|\mathbf{p}| \propto |\mathbf{p}|^{-\sigma}\, d|\mathbf{p}| \qquad \text{with} \qquad \sigma = \frac{r_{\rm eff} + 2}{r_{\rm eff} - 1}\,, \tag{4}$$

where $f(|\mathbf{p}|)d|\mathbf{p}|$ is the number density between $|\mathbf{p}|$ and $|\mathbf{p}|+d|\mathbf{p}|$ and $r_{\rm eff}$ is the effective compression ratio "felt" by particles with a particular upstream diffusion length. For a spatial diffusion coefficient $\kappa = \lambda v/3$, the upstream diffusion length, $L_{\rm D}$, is approximated by

$$L_{\rm D} \simeq \frac{\kappa}{u(x)} \simeq \frac{\lambda v}{3u(x)} = \frac{\eta r_g v}{3u(x)}\,. \tag{5}$$

For low energy particles with $-0.2\,\eta\, r_{\rm g1} < -L_{\rm D} < 0$, $r_{\rm eff} = 2$ ($\sigma = 4$) (note that we define the upstream direction to be negative in Figure 1). As particles increase in energy, the magnitude of $L_{\rm D}$ increases and for $-10\,\eta\, r_{\rm g1} < -L_{\rm D} < -0.2\,\eta\, r_{\rm g1}$, particles will feel $r_{\rm eff} \simeq 3$ ($\sigma = 2.5$). For $-L_{\rm D} < -10\,\eta\, r_{\rm g1}$, $r_{\rm eff} = 4$ ($\sigma = 2$). The different $r_{\rm eff}$'s translate into spectral breaks which are clearly visible in Figure 2. The heavy vertical lines are calculated from equation (5) and indicate the momenta corresponding to $L_{\rm D} = -0.2\,\eta\, r_{\rm g1}$ and $-10\,\eta\, r_{\rm g1}$ for electrons and protons. The spectral breaks occur within a factor of two of $L_{\rm D}$ predicted by equation (5). Note that the distributions plotted are calculated downstream from the shock and the fact that the proton "thermal" peak is at a much higher momentum than the electron peak reflects both the fact that if protons and

---

[1] We note that the results we present here for electron injection efficiencies are in partial disagreement with our earlier results in Ellison & Reynolds (1991). In that paper (specifically Figure 7 in that paper), we claimed that electron injection efficiencies were extremely sensitive to the injection energy and that electrons injected with energies less that several 10's of keV would fall many orders of magnitude below protons in the super-GeV domain. Our current results for the electron injection efficiency, are somewhat less sensitive to injection parameters and do not show the strong decrease in electron normalization compared to protons we claimed earlier. We believe our current results are correct and that our previous claim was an error. In any case, this error is restricted to the lowest energy electrons and the *shape* of the electron spectra above $\sim$ 100 keV is unaffected. In particular, our modeling of the radio synchrotron emission (Reynolds & Ellison 1992) is unaffected by this since only the shape of the electron spectrum at relativistic energies was used.

electrons have the same energy, the proton momentum will be $\sqrt{m_p/m_e}$ greater, and that protons receive a much larger energy boost in a single shock crossing than do electrons. The dotted curve in Figure 2 shows $f(|\mathbf{p}|)$ for electrons with $p_{crit} = 1.5 \times 10^{-3}\, m_p c$ (i.e. $E_{crit} = 3$ MeV). With this p_{crit}, and keeping $E_{inj} = 1$ keV, the upstream electron diffusion length, at injection, is

$$L_D \simeq \frac{\eta r_g(p_{crit}) v_{inj}}{3u(x)} \simeq -0.26\, \eta\, r_{g1} \,. \tag{6}$$

The position $-0.26\,\eta\, r_{g1}$ is indicated in Figure 1 by an arrow. Thus, the lowest energy electrons will have an upstream diffusion length such that $r_{eff} = 3$ and this is reflected in the fact that the spectrum at the lowest energies has $\sigma \simeq 2.5$. Once electrons obtain $-L_D < -10\,\eta r_{g1}$, their slope flattens to $\sigma = 2$, as occurred with the dashed curve.

One important consequence of our choice of $\lambda \propto r_g$ is that, except for the possibility that the values for η may differ, non-relativistic electrons and protons of a given energy E have *the same upstream diffusion length*, feel the same effective compression ratio, and hence will attain the same slope (provided $E \geq E_{crit}$, since then $\eta_e = \eta_p$); such equality is true also for fully relativistic particles. Deviations from this behavior arise in the trans-relativistic regime, thereby generating an adjustment in the relative normalizations of the distributions of electrons and protons. Electrons at $E < E_{crit}$ will possess steeper distributions than those at $E > E_{crit}$. This simple picture can be altered by other injection conditions if, for example as indicated in Figure 2, the proton energy after a single shock crossing is well above the electron energy. Note that in a smooth shock, the *less* efficiently electrons are scattered, the *more* efficiently they will be accelerated. This behavior is clearly illustrated in Figure 2, where the slope obtained at a particular energy is determined by the effective compression ratio that a particle feels as it scatters back and forth across the shock. The further upstream a particle diffuses, the greater the effective compression ratio and the flatter the subsequent spectrum at a given energy, corresponding to greater acceleration efficiency. At electron energies well above an MeV, the combined effect of E_{crit} and f_e is just to scale the intensity of the electron spectrum: the larger E_{crit} (corresponding, say, to greater damping of whistler waves) and/or f_e, the more efficiently the electrons are injected and accelerated, but the spectral shape stays constant at high energies.

2.1.3. Smoothed, Non-Linear Shocks

While most applications of shock acceleration theory to astrophysics are *test-particle* ones (e.g. see Jones and Ellison 1991; Baring 1997, for discussions), non-linear effects become important in strong shocks when the energy density in accelerated particles is comparable to the thermal gas pressure. If this is the case, the flow hydrodynamics are modified by the backpressure of the accelerated particles, forcing the upstream plasma to decelerate forming a precursor to the discontinuous viscous subshock. In our Monte Carlo simulation, the spatial structure of the shock is determined by iteration of both the average flow speed throughout the shock and the overall compression ratio, until the mass, momentum, and energy fluxes are constant everywhere; typical

velocity profiles are depicted in Figure 4 (discussed below). The non-linearity of this problem is manifested through the feedback of the particles on the flow velocity, which in turn determines the shape of the particle distribution. The net effect that emerges is one where the overall compression ratio, from far upstream to far downstream of the discontinuity, *exceeds* that of the test-particle scenario. This phenomenon was identified by Eichler (1984), and Ellison & Eichler (1984), and arises because (i) high energy particles escape from the shock which reduces the overall energy density and pressure allowing the compression of the downstream gas to increase, and (ii) production of relativistic particles softens the equation of state of the gas, also allowing the net compression to increase. Losses due to cooling can also generate very large compression ratios during the radiative phase of supernova remnant evolution. As far as shock dynamics are concerned, radiative cooling via the escape of photons is completely analogous to the escape of particles.

We note that the results presented here include non-adiabatic heating of the upstream thermal gas through the generation and dissipation of Alfvén waves in a manner similar to that assumed by McKenzie & Völk (1984) and Markiewicz, Drury, & Völk (1990). The overall acceleration efficiency depends critically on the strength of the subshock which, in turn, depends on the amount of heating in the precursor. If heating is minimal, as with adiabatic compression, the subshock will be strong and the injection and acceleration of particles at the subshock will be efficient. This will result in a large escaping energy flux at the highest energies and a large overall compression ratio. On the other hand, if heating beyond that from adiabatic compression takes place, the subshock will be weaker, injection and acceleration will be less, and the escaping energy flux and overall compression ratio will be lower. This effect is discussed in detail in Berezhko, Yelshin, & Ksenofontov (1996) and we use their technique for approximating the heating due to Alfvén wave dissipation. Briefly, it is assumed that cosmic rays generate Alfvén waves which rapidly saturate. At this point, the background gas is heated *at the same rate* as energy from the cosmic rays is transfered to the Alfvén waves, independent of the details of the damping mechanism. In addition, we follow Berezhko, Yelshin, & Ksenofontov and assume that the upstream Alfvén waves propagate primarily toward the shock so that the speed of the upstream scattering centers responsible for particle acceleration is reduced by the Alfvén speed. Downstream, we assume the waves are frozen in the fluid. An important difference between our treatment of Alfvén wave dissipation and that of Berezhko, Yelshin, & Ksenofontov is that they assume that the Alfvén waves saturate at $\delta B \sim B$, i.e. the Bohm limit, while we keep η in equation (1) a free parameter. As Berezhko, Yelshin, & Ksenofontov describe, the effects of this heating are most important at high Alfvén Mach numbers and can dramatically reduce the overall compression ratio from values $\sim$ 100 in weak magnetic field conditions to values not much above the test-particle value in strong magnetic fields. A paper detailing the implementation of this effect in the Monte Carlo simulation is in preparation (Berezhko & Ellison 1998).

As long as the diffusion coefficient is an increasing function of energy, pure power laws are not produced in non-linear shocks. Since higher energy particles have longer diffusion lengths, they sample a broader portion of the flow velocity profile, and feel larger compression ratios.

Consequently, these particles have a flatter power-law index than those at lower energies, thereby driving the pressure in a non-linear fashion. The severity of the non-linearity is determined by the overall scale of the shock-precursor which couples to the diffusion length $d_{\rm max} \sim \kappa(E_{\rm max})/u_{\rm sk}$ of the highest energy particles in the system. This defines the scale of the turbulent foreshock region, beyond which waves generated by the shocked plasma do not penetrate into the ISM. We discuss how the maximum energy $E_{\rm max}$ is determined in Section 2.3 below; for now, we remark that acceleration can be limited by particles escaping if they diffuse sufficiently far ahead of the shock, of the order of a few tenths of the shock radius. More commonly for young SNRs such as Cas A, the finite age of a SNR shock limits the time available for particle acceleration, giving a lower maximum energy.

In the Monte Carlo simulation, we limit the acceleration by introducing an upstream free escape boundary (FEB) at the distance, $d_{\rm FEB} = d_{\rm max}$, ahead of the shock. Shocked particles reaching the FEB stream freely across it and are lost from the system (i.e. to the interstellar medium outside) effectively truncating the acceleration process. This boundary could correspond to the finite curvature of a real SNR shock, in which case it would scale as some fraction of the shock radius, or it could correspond to the finite-age limit as we discuss below. Note that the relevant size of the acceleration region could be further constrained by the presence of dense neutral or incompletely ionized material (Drury, Duffy, & Kirk 1996), since such regions strongly suppress wave generation. We model the downstream region as a uniform flow, ignoring the radial dependence of the flow speed that emerges from scaling solutions (e.g. Sedov 1959). This approximation is acceptable as long as $d_{\rm max} \ll R_{\rm sk}$, and if this applies, adiabatic losses/gains are small, so we neglect them in this paper. Note that Berezhko (1996) finds that downstream adiabatic heating and geometrical effects in a spherical blast wave increase the maximum energy somewhat above the finite-age limit in a plane shock. Berezhko contends that such increases arise implicitly because $d_{\rm max}$ approaches $\sim 0.1 R_{\rm sk}$. Such modifications to our approach may prove necessary at late times, as discussed in Section 2.3.2.

2.2. SNR Blast Waves and the Sedov Solution

Initial ejection velocities in supernovae are of order $5 \times 10^3 - 2 \times 10^4$ km s^{-1} (e.g. Chevalier 1981), and the ejecta push a blast wave into the ISM. Initially, the forward moving blast wave expands relatively freely, but the actual evolution depends on the spatial density profile of the ejecta and of the surrounding, pre-supernova material; for power-law variations of ejecta density with radius, Chevalier (1982) found a self-similar driven wave solution in which the outer blast wave radius, $R_{\rm sk}$, varies as a power, m, of time between 0.57 and 1 (i.e. $R_{\rm sk} \propto t^m$ and $V_{\rm sk} \propto t^{m-1}$) depending on the power-law exponents in ejecta and circumstellar medium. As the swept-up mass, $M_{\rm swept}$, increases, eventually this self-similar evolution is broken, and a gradual transition takes place toward a full Sedov self-similar solution, i.e. $m = 0.4$ (e.g. Cioffi, McKee, & Bertschinger 1988). Such a transition, at times $t \sim t_{\rm trans}$, marks the epoch where the mass, $4\pi R_{\rm sk}^3 \rho_1/3$, of the

interstellar medium (of mass density ρ_1) that has been swept up by the blast wave has come to dominate the mass, $M_{\rm ej}$, of the supernova ejecta.

While the evolution of any real SNR may be extremely complex, particularly due to variations in the pre-supernova environment, the gross features of the evolution after $t_{\rm trans}$ can be modeled simply with the standard Sedov (1959) relations for shock speed and radius. For times $t_{\rm SNR} > t_{\rm trans}$, but before the shock becomes radiative, we assume the outer shock radius, $R_{\rm sk}$, and speed, $V_{\rm sk}$, obey these relations, i.e.

$$R_{\rm sk} \simeq \xi \left(\frac{\mathcal{E}_{\rm SN}}{\rho_1}\right)^{1/5} t_{\rm SNR}^{2/5} , \qquad V_{\rm sk} \simeq \frac{2}{5}\xi \left(\frac{\mathcal{E}_{\rm SN}}{\rho_1}\right)^{1/5} t_{\rm SNR}^{-3/5} ; \qquad t_{\rm SNR} > t_{\rm trans} . \tag{7}$$

In these expressions, $\mathcal{E}_{\rm SN}$ is the energy of the supernova explosion $\xi = 1.15$ (e.g. Shu 1992), and energy losses from cosmic rays escaping from the shock are neglected. We then make the following definitions for the transition between the quasi-free expansion and Sedov phases, using the criterion that the swept-up mass equal the ejected mass: $M_{\rm swept} \simeq (4\pi/3)\, R_{\rm trans}^3 \rho_1 = M_{\rm ej}$, defining $R_{\rm trans}$ as the radius of the outer forward shock at the transition, and where $\rho_1 = 1.4\, n_{\rm p,1} m_{\rm p}$ is the unshocked ISM density ($n_{\rm p,1}$ is the unshocked proton number density and hereafter we assume the ISM has cosmic abundances). It follows that

$$R_{\rm trans} \equiv \left(\frac{3}{4\pi}\frac{M_{\rm ej}}{\rho_1}\right)^{1/3} \simeq 1.9 \left(\frac{n_{\rm p,1}}{\rm cm^{-3}}\right)^{-1/3} \left(\frac{M_{\rm ej}}{M_\odot}\right)^{1/3} \ {\rm pc} . \tag{8}$$

Using $R_{\rm trans}$, we define the time of the transition from the standard Sedov solution, i.e.

$$t_{\rm trans} \equiv \left(\frac{R_{\rm trans}}{\xi}\right)^{5/2} \left(\frac{\mathcal{E}_{\rm SN}}{\rho_1}\right)^{-1/2} \simeq 90 \left(\frac{n_{\rm p,1}}{\rm cm^{-3}}\right)^{-1/3} \left(\frac{\mathcal{E}_{\rm SN}}{10^{51}{\rm erg}}\right)^{-1/2} \left(\frac{M_{\rm ej}}{M_\odot}\right)^{5/6} \ {\rm yr} , \tag{9}$$

and the shock speed at the transition as,

$$V_{\rm trans} \equiv \frac{2}{5}\xi \left(\frac{\mathcal{E}_{\rm SN}}{\rho_1}\right)^{1/5} t_{\rm trans}^{-3/5} \simeq 8200 \left(\frac{\mathcal{E}_{\rm SN}}{10^{51}{\rm erg}}\right)^{-1/2} \left(\frac{M_{\rm ej}}{M_\odot}\right)^{-1/2} \ {\rm km\ s^{-1}} . \tag{10}$$

If we assume that $\mathcal{E}_{\rm SN} = 10^{51}$ erg and $n_{\rm p,1} = 1$ cm^{-3}, then SN Ia with ejected mass of $M_{\rm ej} \sim M_\odot$ have $V_{\rm trans} \sim 8000$ km s^{-1}, while SN II with $M_{\rm ej} \sim 4M_\odot$ have $V_{\rm trans} \sim 4000$ km s^{-1}.

While the above definitions are clearly approximations and alternative ones could be made, these are simple, they model the most prominent features of SNRs in homogeneous media, and they are appropriate to the accuracy of current observations and model approximations.

2.3. Acceleration Times and Maximum Particle Energies

The maximum energy that can be attained by ions in diffusive shock acceleration is determined by one of two approaches: (i) by equating the acceleration time as a function of energy to the age of the remnant (for the free expansion or early Sedov phase), or (ii) if the diffusion length of the highest energy particles is comparable to the shock radius (which occurs later in the Sedov phase), by capping that length at some fraction of the shock radius, namely 25%.

2.3.1. *Maximum Energy as a Function of Time*

Consider particles (possibly thermal) injected into the acceleration process at a momentum p_i in a shock with u_1 (u_2) representing the upstream (downstream) component of flow speed normal to the shock in its rest frame (which is uniquely defined since we consider plane-parallel shocks), and κ_1 and κ_2 being the upstream and downstream spatial diffusion coefficients in the direction normal to the shock. Here and elsewhere, the subscript 1 (2) always implies quantities determined far upstream (downstream) from the shock, and the negative x-direction will denote the shock normal. Using the diffusion equation, the standard form for the acceleration time, τ_a, to a given momentum $p_{\rm max}$, is found to be (e.g. Forman & Morfill 1979; Drury 1983)

$$\tau_a(p) \;=\; \frac{3}{u_1 - u_2} \int_{p_i}^{p_{\rm max}} \left(\frac{\kappa_1}{u_1} + \frac{\kappa_2}{u_2} \right) \frac{dp'}{p'} \;. \tag{11}$$

Since the interstellar medium is effectively stationary in the observer's frame relative to the expanding shock front, $u_1 \simeq V_{\rm sk}$. Equation (11) is strictly valid only in the diffusion approximation (i.e. for $v \gg u_1$) and hence is appropriate for our applications to relativistic energies here.

If we use equation (1), relate the upstream and downstream diffusion coefficients via $\kappa_2 = g\kappa_1$ (defining g), and assume that $V_{\rm sk}$ is constant in time (corresponding, for example, to the free expansion phase of a SNR), the inversion of equation (11) yields a rate of energy gain

$$\frac{dE}{dt} \;\simeq\; 300\, \frac{r-1}{r(1+gr)}\, \frac{Q}{\eta} \left(\frac{B_1}{3\mu{\rm G}} \right) \left(\frac{V_{\rm sk}}{10^3\,{\rm km\ s^{-1}}} \right)^2 \ {\rm eV\ s^{-1}} \;. \tag{12}$$

Here B_1 is the far upstream (interstellar) magnetic field and we have assumed $\eta =$ constant across the shock. For a maximum energy $E_{\rm max}$ (much larger than the injection energy) corresponding to $p_{\rm max}$, this integrates to give an acceleration time

$$\tau_a \;\simeq\; 106\, \frac{r(1+gr)}{r-1}\, \frac{\eta}{Q} \left(\frac{B_1}{3\mu{\rm G}} \right)^{-1} \left(\frac{V_{\rm sk}}{10^3\,{\rm km\ s^{-1}}} \right)^{-2} \left(\frac{E_{\rm max}}{1{\rm TeV}} \right) \ {\rm yr} \;, \tag{13}$$

For $g = 0$, particles spend virtually no time in the downstream region; for $g = 1$ the mean free path is independent of the upstream or downstream region; and for $g = 1/r$ ($r = u_1/u_2$ is the shock compression ratio), the mean free path is inversely proportional to the background density, so that particles spend similar times on either side of the shock. Generally we favor $g = 1/r$, which assumes that the field turbulence that is responsible for particle diffusion traces the plasma density. Such an assumption (adopted for example by Draine & McKee 1993) is suggested by the expected field compression ($B_2/B_1 = r$) at quasi-perpendicular shocks, and appears to be supported by Ulysses magnetometer data at highly oblique interplanetary shocks (Baring et al. 1997). Note, however, that particles of the highest energies would be expected to spend somewhat more time diffusing in the upstream region outside the expanding shell due to its convex shape, thereby favoring $g > 1/r$ scenarios. Note also that the proportionality $\tau_a \propto E_{\rm max}$ is a consequence of the $\lambda \propto r_g$ assumption. It follows that if the shock speed is constant, the maximum energy

obtainable for a SNR shock of an age $t_{\rm SNR}$ is

$$E_{\rm max}(t_{\rm SNR}) \simeq E_{\rm trans}\frac{t_{\rm SNR}}{t_{\rm trans}} ; \qquad t_{\rm SNR} < t_{\rm trans} , \tag{14}$$

where

$$E_{\rm trans} \equiv 60\,\frac{r-1}{r(1+gr)}\,\frac{Q}{\eta}\left(\frac{B_1}{3\mu{\rm G}}\right)\left(\frac{n_{\rm p,1}}{1\,{\rm cm}^{-3}}\right)^{-1/3}\left(\frac{\mathcal{E}_{\rm SN}}{10^{51}{\rm erg}}\right)^{1/2}\left(\frac{M_{\rm ej}}{M_\odot}\right)^{-1/6}{\rm TeV} \tag{15}$$

is the maximum energy ions achieve at $t_{\rm trans}$ and is obtained from equation (13) using our definitions of $V_{\rm trans}$, $t_{\rm trans}$, and $R_{\rm trans}$. As an example, for $r = 9$, $g = 1/r$, $\eta = 10$, $\mathcal{E}_{\rm SN} = 10^{51}$ erg, $M_{\rm ej} = M_\odot$, $B_1 = 3 \times 10^{-6}\,{\rm G}$, and $n_{\rm p,1} = 1\,{\rm cm}^{-3}$, we find that $V_{\rm trans} \simeq 8200$ km s^{-1}, $t_{\rm trans} \simeq 90$ yr, and $E_{\rm trans} \simeq 2.6$ TeV for protons *and* electrons. Berezhko (1996) obtains a similar form to equation (15), with a slightly larger coefficient because of his treatment of expansion and the associated adiabatic effects.

From equation (15) it is clear that particularly energetic supernova explosions or large ISM field strengths are required to generate cosmic rays above 10^{14} eV and subsequently populate the "knee" in the cosmic ray distribution. Note also, that $E_{\rm trans}$ has a fairly weak dependence on the ISM density, but one which becomes important at very low densities. Furthermore, equation (15) depends on the charge of the species but not the mass and hence is identical for protons and electrons, provided that $p_{\rm max}$ far exceeds the critical electron momentum $p_{\rm crit}$ discussed above. The maximum energy in equation (14) does not result in abrupt cutoffs to the distributions of the accelerated populations, but rather marks the energy about which quasi-exponential turnovers appear: spatial diffusion near the FEB smears out the energy of the cutoffs. If we use Equations (9), (14), and (15) to estimate $E_{\rm max}$ for very young remnants like SN1987A, it quickly becomes clear that these remnants will take several decades to accelerate particles to energies beyond a few TeV. For $\mathcal{E}_{\rm SN} \sim 10^{51}$ erg, $M_{\rm ej} \sim M_\odot$, and $t_{\rm SNR} = 10$ yr, $E_{\rm max} \sim 7$ TeV. Protons of this energy produce pion-decay photons of substantially lower energy (by a factor of a few); similarly, electron bremsstrahlung photons are on average about one-third the energy of the primary electrons. IC photons produced by 7 TeV electrons have energies of less than 1 TeV. Thus we expect that SN1987A will not be a bright TeV gamma-ray source anytime in the next decade, contrary to the suggestion of Kirk, Duffy, & Ball (1995).

In determining $E_{\rm max}$ at any time, it must be noted that it is some weighted function of the injection history, as well as the acceleration history of the highest energy particles. Hence, besides the unknowns in the shock processes, the SNR remnant environment and its evolution, the fact that the rate per unit area at which particles are injected into the shock is dependent on a remnant's evolutionary phase complicates the picture. This rate is proportional to $R_{\rm sk}^2 V_{\rm sk}$, an intrinsic variation that provides a rapid increase in injection during the free expansion phase. However, in the Sedov phase, the number of protons per unit time that are crossed by the shock is

$$\frac{dN_{\rm p}}{dt} \simeq 6 \times 10^{47}\left(\frac{n_{\rm p,1}}{{\rm cm}^{-3}}\right)^{2/5}\left(\frac{\mathcal{E}_{\rm SN}}{10^{51}{\rm erg}}\right)^{3/5}\left(\frac{t_{\rm SNR}}{10^3{\rm yr}}\right)^{-1/5} \qquad {\rm sec}^{-1} , \tag{16}$$

a slowly decaying function of time. For purposes of our $E_{\rm max}$ estimate, we will *neglect* particles accelerated during the free expansion phase and assume that the rate at which the shock overtakes ambient particles in the Sedov phase is independent of time. This assumption marks an important distinction between our calculation and Berezhko's (1996). He obtains considerably higher maximum energies because of strong acceleration in the free-expansion phase, which we neglect here because of the relatively small number of particles injected then. Hence, in the Sedov phase, if we continue to assume that $\lambda = \eta\, r_{\rm g}$, equation (12) yields:

$$E_{\rm max}(t_{\rm SNR}) \simeq 5\, E_{\rm trans}\left[1 - \left(\frac{t_{\rm SNR}}{t_{\rm trans}}\right)^{-1/5}\right] \; ; \qquad t_{\rm SNR} > t_{\rm trans} \; , \tag{17}$$

where we have assumed that $(r-1)/[r(1+gr)]$ is a weakly varying function of time. In fact, the compression ratio, r, will vary with time as the shock Mach number and $E_{\rm max}$ change, but this variation will become smaller at later times. This solution for $E_{\rm max}$ includes the acceleration history of particles at all times during the Sedov phase, and asymptotically approaches $5\, E_{\rm trans}$ at late times. The further inclusion of particles accelerated during the free expansion phase would only modify this formula to $E_{\rm trans}[6 - 5(t_{\rm SNR}/t_{\rm trans})^{-1/5}]$, a small change, but one that encompasses the highest energy cosmic rays. The reader is referred to Berezhko & Völk (1997) for an estimate of how these highest energy particles influence the γ-ray emission.

2.3.2. Maximum Energy as a Function of Shock Precursor Scale

As the remnant evolves, the maximum extent of the precursor outside the outer shock will be determined by the diffusion length ahead of the shock, $d_{\rm FEB}$, of the highest energy particles in the system at its current age, whose energy is $E_{\rm max}(t_{\rm SNR})$ (as determined from equation [17]). Since the diffusion scale is $\sim \kappa_1/V_{\rm sk}$, one obtains, for fully relativistic particles,

$$d_{\rm FEB} \sim \frac{\eta r_{\rm g,max} c}{3 V_{\rm sk}} = \frac{\eta}{3QeB_1}\frac{E_{\rm max}^{\rm age}}{V_{\rm sk}} \quad , \quad E_{\rm max}^{\rm age} = E_{\rm max}(t_{\rm SNR}) \; , \tag{18}$$

where we have used the superscript 'age' to indicate that the maximum energy is determined by the age of the remnant. The distance to the FEB defines the full width of the shock precursor, and must be a small fraction of $R_{\rm sk}$ in order for the plane-parallel shock simulation to be applicable to quasi-spherical shells. In the Sedov phase, the combination of equations (7), (15), and (17) yields

$$\frac{d_{\rm FEB}}{R_{\rm sk}} \simeq \frac{2}{3}\frac{r-1}{r(1+gr)}\left(\frac{t_{\rm SNR}}{t_{\rm trans}}\right)^{1/5}\left[1 - \left(\frac{t_{\rm SNR}}{t_{\rm trans}}\right)^{-1/5}\right] \; , \tag{19}$$

and it is clear that if this phase lasts long enough, $d_{\rm FEB}/R_{\rm sk}$ will become greater than unity, rendering our scheme for the termination of acceleration inconsistent. A similar $t_{\rm SNR}^{1/5}$ dependence was noted by Kang & Jones (1991). The precise age at which $d_{\rm FEB}/R_{\rm sk} = 1$ is a strong function of the assumed value of g, and to a lesser extent of r. In practice, we place our upstream free

escape boundary at a distance $d_{\rm FEB}$ (equation [18]) ahead of the shock if $d_{\rm FEB}/R_{\rm sk} < f < 1$. If $d_{\rm FEB}/R_{\rm sk} > f$, we set $d_{\rm FEB} = fR_{\rm sk}$. In this case, the maximum energy is given by

$$\begin{aligned} E_{\rm max}^{\rm size} &\simeq f\frac{3Qe}{\eta}B_1 V_{\rm sk} R_{\rm sk} \\ &\sim 270\, f\frac{Q}{\eta}\left(\frac{B_1}{3\mu{\rm G}}\right)\left(\frac{n_{\rm p,1}}{{\rm cm}^{-3}}\right)^{-2/5}\left(\frac{\mathcal{E}_{\rm SN}}{10^{51}{\rm erg}}\right)^{2/5}\left(\frac{t_{\rm SNR}}{10^3{\rm yr}}\right)^{-1/5}{\rm TeV}\ , \end{aligned} \tag{20}$$

where we use the superscript 'size' to indicate that this energy is constrained by the remnant size.

The arbitrary factor f, which we set equal to 1/4 in all of the work here, is included to ensure that the self-generated magnetic turbulence from the highest energy particles is localized (as discussed just below) to the precursor of the spherical shock. The transition at $d_{\rm FEB}/R_{\rm sk} = f = 1/4$ is, in effect, a transition from age-limited acceleration at early times to size-limited acceleration at late times. By our definitions, this transition occurs when $d_{\rm FEB}/(fR_{\rm sk}) = 1$, that is, when $t_{\rm SNR}/t_{\rm trans} = (3fr^2g + 3fr + 2r - 2)^5/(2r-2)^5$. For $r \sim 9$, $f = 1/4$, and $g = 1/r$, the transition occurs at $t_{\rm SNR}/t_{\rm trans} \gtrsim 20$, i.e. acceleration of the highest-energy particles ceases when their diffusion lengths approach $fR_{\rm sk}$ for much of the Sedov phase, the scenario that Berezhko, Yelshin, & Ksenofontov (1994) prefer. However, if $g = 1$, the acceleration is age-limited for a much larger range of times (up to $t_{\rm SNR}/t_{\rm trans} \sim 3 \times 10^3$), as in the considerations of Lagage & Cesarsky (1983). We do not attempt to model acceleration into the radiative phase which begins at approximately $t_{\rm rad} \simeq 2.9 \times 10^4\,(n_{\rm p,1}/{\rm cm}^{-3})^{-9/17}\,(\mathcal{E}_{\rm SN}/10^{51}{\rm erg})^{4/17}$ yr (Blondin et al. 1997), and therefore is well beyond the ages of the young remnants considered here.

Hence, the combination of size-limited and space-limited acceleration is implemented in our steady-state Monte Carlo model by placing a free escape boundary at a distance, $d_{\rm FEB}$, upstream from the shock, where

$$d_{\rm FEB} = \min\left\{\frac{\eta}{3QeB_1}\frac{E_{\rm max}^{\rm age}}{V_{\rm sk}}\ ,\ fR_{\rm sk}\right\}\ ,\quad f = \frac{1}{4}\ . \tag{21}$$

The maximum energies produced by this procedure are shown in Figure 3. The lower three thick curves all have $\eta = 10$, $B_1 = 3 \times 10^{-6}$ G, $n_{\rm p,1} = 1$ cm^{-3}, $\mathcal{E}_{\rm SN} = 1 \times 10^{51}$ erg, and $M_{\rm ej} = M_\odot$ with choices for g as indicated. The thick solid line labeled (b) has the same η, B_1, $\mathcal{E}_{\rm SN}$, and $M_{\rm ej}$ parameters as above with $g = 1/r$ and $n_{\rm p,1} = 0.01{\rm cm}^{-3}$. For the uppermost solid line labeled (c), which shows maximum energies well above 10^{15} eV, we have selected parameters that are especially tuned to yield a high maximum energy, i.e. are appropriate for particle acceleration up to the "knee" in the cosmic ray spectrum. In this case, we have used $\eta = 1$ (i.e. Bohm diffusion with $\lambda \sim r_{\rm g}$), $g = 1/r$, $B_1 = 10 \times 10^{-6}$ G, $n_{\rm p,1} = 10^{-3}{\rm cm}^{-3}$, $\mathcal{E}_{\rm SN} = 10 \times 10^{51}$ erg, and $M_{\rm ej} = 10M_\odot$. For convenience, we have taken $r = 8.5$ in all plots although the actual r will depend on the particular parameters used.

While clearly an approximation, we believe this scheme for setting the maximum energy by converting the time-dependent effects of Sedov dynamics into size-limited acceleration is accurate enough to allow us to describe the essential non-linear effects in a convenient and realistic fashion.

It differs qualitatively from the time-dependent analyses of Berezhko (1996) and other researchers (e.g. Drury, Markiewicz, & Völk 1989; Kang & Jones 1991; Berezhko, Yelshin, & Ksenofontov 1994), principally because of omissions such as adiabatic energy gains in the decelerated remnant interior downstream of the outer shock, the complex interplay between geometry and acceleration history, and the contributions of free expansion phase cosmic ray acceleration to that in the Sedov epoch. Berezhko (1996) observes that these additional features can increase the maximum energy of acceleration by factors of 2–3, which will in turn affect the non-linear feedback between the Fermi process and the hydrodynamics. However, we note that a significant contribution to this increase in $E_{\mathbf{max}}$ above our estimates may be due to Berezhko's assumption that cosmic rays find the interior of the remnant impenetrable due to the establishment of large scale hydrodynamic turbulence via Raleigh-Taylor instabilities, and Berezhko's consequent imposition of a downstream reflecting boundary. In fact, it is probable that the presence of such turbulence and associated field amplification (e.g. see Jun & Norman 1996) will reduce the scale-length for diffusion, thereby increasing downstream escape of cosmic rays and lowering the maximum energy. Therefore, clearly there is some degree of subjectivity in the choice of $E_{\mathbf{max}}$, being not tightly-constrained by observations; our own choice is motivated by its convenience.

2.3.3. Loss Processes for Electrons

Of the various loss processes that influence the particles accelerated at young SNRs, only synchrotron and inverse Compton losses for electrons are important for a wide range of parameters (Coulomb losses only become important for old remnants, e.g. Sturner et al. 1997). The rate of synchrotron energy loss in a field B is given by Lang (1980). For inverse Compton (IC) losses under the conditions we envision, the most important source of seed photons is the primordial cosmic microwave background radiation; other radiation fields contribute less than 20% (e.g. Gaisser, Protheroe, & Stanev 1998) to IC cooling. The IC loss rate is given by a similar expression to the synchrotron loss rate, obtained simply by substituting the radiation energy density for magnetic field energy density. The field strength with the same energy density as the 2.73 K background radiation is $B_{\mathrm{cbr}} \simeq 3.32 \times 10^{-6}$ G, leading to the compact formula describing both synchrotron and inverse Compton losses:

$$\left(\frac{dE}{dt}\right)_{\mathrm{tot}} \simeq -0.034 \left(\frac{\sqrt{B^2 + B_{\mathrm{cbr}}^2}}{3\mu\mathrm{G}}\right)^2 \left(\frac{E}{1\mathrm{TeV}}\right)^2 \mathrm{eV\ s^{-1}}\ . \tag{22}$$

In oblique shocks, a particle undergoing acceleration spends time both upstream and downstream in magnetic fields of varying strength. This makes it impossible to get a precise measure of the loss rate without detailed knowledge of the shock geometry. In the general oblique case, we can set $B = \Gamma B_1$ with $1 \leq \Gamma \leq r$, and $\Gamma = r$ gives an upper limit to the loss rate. Here, however, we model only parallel shocks where the mean magnetic field doesn't vary through the shock and equation (22) can be used directly with $B = B_1$. By comparing equations (12) and (22) we obtain

an upper limit to the electron cutoff energy in the Sedov phase, i.e.

$$E_{\rm cutoff} \simeq 180 \left[\frac{r-1}{r(1+gr)}\frac{Q}{\eta}\right]^{1/2}\left(\frac{B_1}{3\mu{\rm G}}\right)^{1/2}\left(\frac{\sqrt{\Gamma^2 B_1^2 + B_{\rm cbr}^2}}{3\mu{\rm G}}\right)^{-1}\left(\frac{n_{\rm p,1}}{\rm cm^{-3}}\right)^{-1/5} \times \left(\frac{\mathcal{E}_{\rm SN}}{10^{51}{\rm erg}}\right)^{1/5}\left(\frac{t_{\rm SNR}}{10^3{\rm yr}}\right)^{-3/5} {\rm TeV}\ . \quad (23)$$

For our Monte Carlo calculations, we implement equation (23) with $\Gamma = 1$. A similar cutoff energy was obtained by Sturner et al. (1997). In Figure 3 we show equation (23) as light dotted lines. The leftmost dotted line gives the electron cutoff energy for the lower solid line example (a), the middle dotted line gives $E_{\rm cutoff}$ for the $n_{\rm p,1} = 0.01$ cm^{-3}, $\eta = 10$ example (b), and the rightmost dotted line gives $E_{\rm cutoff}$ for the $n_{\rm p,1} = 10^{-3}$ cm^{-3}, $\eta = 1$ example (c). Clearly, electron acceleration will be essentially unaffected in the high density ISM throughout the Sedov phase, but can be severely truncated in lower density regions at all times. In the highest $E_{\rm max}$ example in Figure 3, where parameters were chosen to optimize cosmic ray production, protons can obtain energies two orders of magnitude higher than electrons during most of the SNR evolution.

3. PHOTON PRODUCTION MECHANISMS

Having outlined the relevant processes involved in energetic particle production, we now describe how photons are produced once particle distributions are obtained. Unless otherwise stated, all photon energies are expressed as ε_γ, the gamma ray energy in units of $m_{\rm e}c^2$, and we assume cosmic abundance for helium (i.e. $n_{\rm He,1} = 0.1 n_{\rm p,1}$) and that the helium is fully ionized so that the electron number density is $n_{\rm e,1} = 1.2\, n_{\rm p,1}$. For the purposes of this paper, we neglect contributions from species other than protons, fully stripped helium ions, and electrons. For a shock-accelerated distribution of electrons or ions, $(dJ/dE)_{\rm e,i}$, the number density per unit *kinetic* energy is $(4\pi/v_{\rm e,i})(dJ/dE)_{\rm e,i}$, and the number of photons emitted per unit volume per second in the range ε_γ to $\varepsilon_\gamma + d\varepsilon_\gamma$ takes the form

$$\frac{dn_\gamma(\varepsilon_\gamma)}{dt} = \int_0^\infty \frac{dn_\gamma(E_{\rm e,i},\,\varepsilon_\gamma)}{dt}\left[\left(\frac{4\pi}{v_{\rm e,i}}\right)\left(\frac{dJ}{dE}\right)_{\rm e,i}\right] dE_{\rm e,i}\ , \quad (24)$$

where $dn_\gamma(E_{\rm e,i},\,\varepsilon_\gamma)/dt$ is the emissivity of a single particle, either an electron or an ion, of kinetic energy $E_{\rm e,i}$. We consider four processes: pion decay emission, bremsstrahlung, inverse Compton scattering, and synchrotron radiation, and note that, as discussed in Section 3.1 below, emission due to secondary electrons (i.e. pairs produced via the decay of $\pi^\pm$ created in ion-ion collisions) is negligible. If a source is at a distance $d_{\rm SNR}$, with an emission volume $V_{\rm SNR}$, the number of photons per unit area per second per unit photon energy arriving at Earth is $[dn_\gamma(\varepsilon_\gamma)/dt]V_{\rm SNR}/(4\pi d_{\rm SNR}^2)$.

3.1. Pion Decay Radiation

We first consider π^0 decay emission resulting from pions generated in ion–ion collisions: $p + p \rightarrow \pi^0 \rightarrow \gamma + \gamma$, etc. This process has been popular in discussions of gamma-ray emission from supernova remnants dating from the early work of Higdon & Lingenfelter (1975) to the more extensive analyses of Drury, Aharonian, & Völk (1994) and Naito & Takahara (1994), and plays a prominent role in the modeling of the diffuse galactic gamma-ray background (Bertsch et al. 1993, Hunter et al. 1997). Here, we adopt a modified scaling model for pion production, the details of which can be found in Baring & Stecker (1998).

The scaling concept, originally devised by Feynman (1969), is usually invoked at cosmic ray hadron energies above 10 GeV. It assumes that the Lorentz invariant differential cross-section $E\,d^3\sigma/dp^3$ approaches a function that is independent of the fast hadron's energy as it tends to infinity. A variety of scaling descriptions exist, and all of them, including ours, determine this function via empirical fits to experimental data. Scaling models work well for kinetic energies up to hundreds of GeV, beyond which quantum chromodynamics (QCD) becomes important and scaling violations ensue. Such deviations from scaling behavior in this regime are accounted for in a fairly simple manner in the model of Baring & Stecker (1998) by adopting non-scaling corrections to the total cross-section which extend the usefulness into the super-TeV range. At low hadron kinetic energies, corresponding to photons produced between $\sim$ 20 MeV and 200 MeV, an isobaric model (Stecker 1971) that is discussed at length in Baring & Stecker (1998) is appropriate. We adopt non-scaling corrections in this regime also, so that our computations only underestimate photon spectra by $\sim$ 20–30%. Minor improvements to this can be achieved using a hybrid scaling-isobaric approach (see Dermer 1986a,b; Baring & Stecker 1998).

Consider first proton–proton collisions. Baring & Stecker (1998) use a *radial scaling* (RS) model, where the Lorentz invariant differential cross-section $E\,d^3\sigma/dp^3$ is approximated by a function that depends on two variables: (i) the component of pion momentum p_t^* transverse to the cosmic ray proton (or ion) beam direction, and (ii) the radial scaling variable $x_{\rm R}$, which is the ratio of the center-of-mass (CM) frame pion Lorentz factor γ_π^* to $\gamma_{\pi,\rm max}^*$, the maximum possible value of γ_π^*. Note that hereafter, asterisks denote quantities evaluated in the CM frame of the colliding protons. Pion production kinematics dictate that $\gamma_{\pi,\rm max}^* = [2(\gamma_{\rm p}-1)+\mu_\pi^2]/[2\mu_\pi\sqrt{2(\gamma_{\rm p}+1)}]$ for $\mu_\pi = m_\pi/m_{\rm p} = 0.1438$. Baring & Stecker (1998) adopt the form for $E\,d^3\sigma/dp^3$ obtained by Tan & Ng (1983), which was applied separately to π^+ and π^- production data: the average of these is taken as the cross-section for π^0 creation by invoking isospin conservation in strong interactions. For given transverse momentum p_t^* and γ_π^*, there are two solutions for the pion Lorentz factor γ_π, namely $\gamma_\pi^\pm = \gamma_{\rm cm}\,(\gamma_\pi^* \pm \beta_{\rm cm}\,p_l^*)$, where $p_l^* = \sqrt{(\gamma_\pi^*)^2 - 1 - (p_t^*)^2}$. Here p_l^* is the *longitudinal* momentum of the pion, i.e. along the direction defined by one of the incoming protons. The Lorentz factor $\gamma_{\rm cm} = \sqrt{(\gamma_{\rm p}+1)/2}$ is that corresponding to the boost between the CM and laboratory (i.e.

ISM) frames. The expression for the differential photon production rate is then

$$\frac{dn_\gamma(\varepsilon_\gamma)}{d\varepsilon_\gamma} = 4\pi\, n_{\rm p}\, \gamma^*_{\pi,\max}\, c\, \frac{m_{\rm e}}{m_\pi} \int_{\gamma_{\rm TH}}^{\infty} d\gamma_{\rm p}\, \beta_{\rm p}\, \psi(\gamma_{\rm p})\, N_{\rm p}(\gamma_{\rm p}) \int dp_l^*\, dx_{\rm R} \left\{ \frac{\theta(\gamma_\pi^+ - \gamma_-)}{\sqrt{(\gamma_\pi^+)^2 - 1}} + \frac{\theta(\gamma_\pi^- - \gamma_-)}{\sqrt{(\gamma_\pi^-)^2 - 1}} \right\} \left(E\, \frac{d^3\sigma}{dp^3} \right)_{\rm RS} (x_{\rm R},\, p_t^*)\ , \tag{25}$$

where $n_{\rm p}$ is the ambient proton density, and $\gamma_- = (m_{\rm e}/m_\pi)\,[\varepsilon_\gamma + m_\pi^2/(4m_{\rm e}^2\varepsilon_\gamma)]$ is the minimum pion Lorentz factor permitted by kinematics for pions decaying to produce photons of energy ε_γ. The θ functions in equation (25) are Heaviside step functions that are zero for $x < 0$ and unity otherwise. The proton distribution in equation (25) can be obtained from omni-directional fluxes produced in the Monte Carlo shock simulations via $N_{\rm p}(\gamma_{\rm p}) = [4\pi m_{\rm p} c^2/v_{\rm p}](dJ/dE)_{\rm p}$. Also, $\gamma_{\rm TH} \simeq 1.298$ is the proton Lorentz factor corresponding to the threshold of pion production. The limits on the $x_{\rm R}$ integration are defined by $1/\gamma^*_{\pi,\max} \le x_{\rm R} \le 1$, while those for p_l^* are given by the constraints that $\gamma_\pi^\pm \ge \gamma_-$, according to the appropriate term in equation (25). For monoenergetic protons, this differential spectrum closely resembles results produced by the PYTHIA code (described in Stöstrand & van Zijl 1987) in the range $10 < \gamma_{\rm p} < 1000$, and for power-law protons it compares well with predictions of Gaisser, Protheroe, & Stanev (1998).

In the strong interaction, neutrons interact with virtually the same properties as protons. Hence heavier species such as alpha particles basically provide additional supplies of *nucleons*, and the collisions of individual nucleons can be described in the above manner. However, care must be taken to account for the nuclear binding of heavier elements. Orth & Buffington (1976) posited that the inclusive cross-section for cosmic rays of mass number $A_{\rm cr}$ colliding with ISM target nuclei of mass number $A_{\rm ISM}$ is

$$\sigma \sim \left(A_{\rm cr}^{3/8} + A_{\rm ISM}^{3/8} - 1 \right)^2 \sigma_{pp\to\pi^0 X}\ . \tag{26}$$

While experimental data on inelastic collisions involving nuclei heavier than hydrogen are sparse, this prescription is appropriate for proton-helium interactions, but its accuracy is unclear for heavier nuclei such as Fe, which are therefore omitted from consideration here.

3.1.1. Secondary electron production

Primary electrons, i.e. those directly accelerated by the Fermi process, dominate the contributions of electron emission. Secondary electrons and positrons are produced via the decay of charged pions that are created in pp and $p\alpha$ collisions, and the cross-section for these modes is comparable to that of the neutral pion modes. Hence, the rate of pair production in pp collisions is roughly $dn_\pm(E_{\rm e})/dt \sim n_{\rm p}^2 c\, \sigma_{pp\to\pi^0 X}(fE_{\rm e})$, where f is a factor of the order of a few that accounts for the pion production inelasticity. If the pairs are permitted to build up without escape for the entire remnant lifetime, then one obtains the maximal estimate for the secondary pair density: $n_\pm(E_{\rm e}) \sim t_{\rm SNR}\, n_{\rm p}^2 c\, \sigma_{pp\to\pi^0 X}(fE_{\rm e})$. Remembering that the timescale for pp collisions

is $t_{\rm pp} \sim (n_{\rm p} c \sigma_{pp\to\pi^0 X})^{-1}$, and that the primary electron density is $n_{\rm e} \sim n_{\rm p}$, then the accumulated pair density can be written as $n_{\pm} \sim n_{\rm e} t_{\rm SNR}/t_{\rm pp}$. The timescale $t_{\rm pp}$ for collisions involving 1 GeV–1 TeV protons is typically of the order of 10^7 years, immediately leading to the conclusion that the primary electron density far exceeds that of the secondaries in young SNRs. Hence the contribution of secondaries to the bremsstrahlung, inverse Compton and synchrotron emission can be neglected. This fact was pointed out by Mastichiadis (1996) for the specific case of synchrotron radiation.

3.2. Bremsstrahlung

Electrons will produce bremsstrahlung radiation as they scatter off the ambient gas. Hence, the rate of photon production, $dn_\gamma(E_{\rm e}, \varepsilon_\gamma)/dt$, in the energy interval between ε_γ and $\varepsilon_\gamma + d\varepsilon_\gamma$ by an electron of *kinetic energy* $E_{\rm e}$ takes the standard form

$$\frac{dn_\gamma(E_{\rm e}, \varepsilon_\gamma)}{dt} = v_{\rm e}\Big[(n_{\rm p} + 4n_{\rm He})\, \sigma_{\rm e-p}(E_{\rm e}, \varepsilon_\gamma) + n_{\rm e}\sigma_{\rm e-e}(E_{\rm e}, \varepsilon_\gamma) \Big] , \qquad (27)$$

where ε_γ is the gamma-ray energy in units of $m_{\rm e}c^2$. Here the electron-ion cross-section, $\sigma_{\rm e-p}(E_{\rm e}, \varepsilon_\gamma)$, differential in photon energy (i.e. integrated over photon and final electron angles), is the famous Bethe-Heitler cross-section (Bethe & Heitler 1934; see also Jauch & Rohrlich 1980), evaluated in the Born approximation; it is used for any electron energy, relativistic or non-relativistic. We note that the ultrarelativistic form for the e-p cross-section [e.g. see equation (15-101) of Jauch & Rohrlich 1980] is the same as σ_1 given in equation (A2) in the Appendix. The electron speed $v_{\rm e}$ is the relative velocity in bremsstrahlung collisions. The Bethe-Heitler formula applies to both protons and alpha particles, with a charge-dependence $\sigma_{\rm e-p} \propto Z^2$. This leads to the $n_{\rm p} + 4n_{\rm He}$ factor multiplying $\sigma_{\rm e-p}$ in equation (27). Coulomb corrections to the Bethe-Heitler cross-section, such as through the Sommerfeld-Elwert factor (Elwert 1939), become important only for projectile electron speeds considerably less than $c/10$; we omit them from our considerations since they are only marginally important given our electron temperatures of a few keV.

The situation for the electron-electron cross-section, $\sigma_{\rm e-e}(E_{\rm e}, \varepsilon_\gamma)$, is more complicated. The full quantum electrodynamical expression for the angle-integrated cross-section, differential in photon energy, was first derived by Haug (1975). The result is extremely long (over a page of algebra), and is numerically cumbersome given that it contains terms that are individually divergent (to several orders) in photon energy as $\varepsilon_\gamma \to 0$. This unwieldiness motivates us to use other expressions that are derived from asymptotic limits for non-relativistic (Fedyushin 1952; Garibyan 1953) and ultrarelativistic (Baier, Fadin, & Khoze 1967) electrons. These are presented in detail in the Appendix, and we choose to switch between the two asymptotic regimes at an energy of $E_{\rm e} = 2\,{\rm MeV}$.

The relative importance of electron-electron and electron-ion bremsstrahlung in the gamma-ray range can be quickly deduced from the cross-sections listed in the Appendix. For $\gamma_{\rm e} \gg 1$ and $\varepsilon_\gamma \gg 1$, the e-e cross-section in equation (A1) is dominated by the σ_1 term, which coincides with

the ultrarelativistic limit of the e-p cross-section [see equation (15-101) of Jauch & Rohrlich 1980]. Hence the emissivities depend only on the target's charge, not its mass. The ratio of electron-electron to electron-ion contributions to bremsstrahlung is then simply $(n_{\rm p,1} + 2n_{\rm He,1})/(n_{\rm p,1} + 4n_{\rm He,1}) \simeq 0.86$ for photon energies above ~ 10 MeV. When the bremsstrahlung collisions involve non-relativistic species (i.e. for X-ray production), the situation changes and the electron-ion contributions dominate the emission, since the dipole contribution to non-relativistic electron-electron bremsstrahlung vanishes. Note also that *inverse bremsstrahlung*, i.e. radiation produced in collisions between high energy protons and ISM electrons, contributes insignificantly to the emissivity. This can be seen from the formulae of Jones (1971): for photon energies $\varepsilon_\gamma \ll 1$, the differential cross-section for inverse bremsstrahlung is $\sigma_{\rm p-e} \simeq (16\,\alpha\, r_0^2/3\varepsilon_\gamma)\,\log\,(0.68\,\gamma_{\rm p}/\varepsilon_\gamma)$. This can be compared with the Bethe-Heitler cross-section (e.g. Jauch & Rohrlich 1980) for normal bremsstrahlung, which in the $\varepsilon_\gamma \ll 1$ limit for $\gamma_{\rm e} \gg 1$ becomes $\sigma_{\rm e-p} \simeq (16\,\alpha\, r_0^2/3\varepsilon_\gamma)\,\log(2\,\gamma_{\rm e}^2/\varepsilon_\gamma)$; it is clear that for $m_{\rm e}\gamma_{\rm p}/m_{\rm p} \sim \gamma_{\rm e} \gg 1$, inverse bremsstrahlung provides only minor contributions, unless the e/p cosmic ray ratio is quite small.

3.3. Inverse-Compton Production of Gamma-Rays

Inverse-Compton (IC) radiation is dominated by cosmic microwave background (CMB) photons, with the less well-determined IR/optical backgrounds that are local to typical remnants contributing generally about 10%–15% of the IC flux (e.g. see Gaisser, Protheroe, & Stanev 1998). For electrons below ~ 10 TeV, the scatterings always occur well in the Thomson limit and the photon energy in the electron rest frame is much less than the electron rest energy: $4\gamma_{\rm e}\varepsilon_s \ll 1$, where the seed photon energy (in the lab frame) is $\varepsilon_s m_{\rm e}c^2$. However, we must allow for higher energies than this. For the CMB, $\varepsilon_s m_{\rm e}c^2 \sim 3kT = 7.1 \times 10^{-4}\,{\rm eV}$ at the mean energy of the 2.73 K blackbody distribution, so the Thomson limit is strictly valid only for electron Lorentz factors obeying $\gamma_{\rm e} \ll 3.5 \times 10^8$ or $E_{\rm e} \ll 2 \times 10^{14}{\rm eV}$. While this is often satisfied for our calculations, Klein-Nishina corrections do become important for $E_{\rm e} \gtrsim 3 \times 10^{13}{\rm eV}$. This introduces both electron recoil effects, that limit the maximum energy of the upscattered photons to less than $\gamma_{\rm e}$, and a drop in the cross-section with increasing electron energy. In our calculations, we use the angle-integrated Klein-Nishina cross-section, differential in the final energy of the photons, as derived by Jones (1968, see also Blumenthal & Gould 1970), the standard result adopted by other authors (e.g. Sturner et al. 1997):

$$\sigma_{\rm K\text{-}N}(\varepsilon_s,\,\gamma_{\rm e};\varepsilon_\gamma) \;=\; \frac{2\pi r_0^2}{\varepsilon_s\gamma_{\rm e}^2}\left[2q\,\log_{\rm e} q + 1 + q - 2q^2 + \frac{\Gamma^2 q^2(1-q)}{2(1+\Gamma q)}\right], \qquad (28)$$

with $\Gamma = 4\varepsilon_s\gamma_{\rm e}$ being the parameter that governs the importance (when $\Gamma \gtrsim 1$) or otherwise of photon recoil and Klein-Nishina effects, and with

$$q \;=\; \frac{\varepsilon_\gamma}{4\varepsilon_s\gamma_{\rm e}(\gamma_{\rm e} - \varepsilon_\gamma)}\,, \quad 0 \le q \le 1\,, \qquad (29)$$

where $\varepsilon_s m_e c^2$ is the initial photon energy, $\varepsilon_\gamma m_e c^2$ is the upscattered (final) photon energy, and $\gamma_e = (E_e + m_e c^2)/m_e c^2$, as for bremsstrahlung. The constant $r_0 = e^2/(m_e c^2)$ is the classical electron radius ($\sigma_T = 8\pi r_0^2/3$ is the Thomson cross-section). This result assumes isotropic soft photon fields, the case for the CMB radiation. Clearly the Klein-Nishina decline is manifested through the last term in equation (28), while the recoil is embedded in the q parameter. For any seed-photon (dimensionless) energy ε_s, the maximum scattered photon energy is determined by setting $q = 1$, giving $\varepsilon_\gamma \leq \Gamma\gamma_e = 4\gamma_e^2\varepsilon_s$ in the Thomson limit and $\varepsilon_\gamma \leq \gamma_e$ in the extreme Klein-Nishina limit.

The inverse Compton emissivity for isotropic photon fields can then be written down quickly (e.g. Blumenthal & Gould 1970, or see Reynolds 1982, for representations in terms of frequency-dependent photon intensities):

$$\frac{dn_\gamma(\varepsilon_\gamma)}{dt} = c \int N_e(\gamma_e)\, d\gamma_e \int d\varepsilon_s n_\gamma(\varepsilon_s)\, \sigma_{K\text{-}N}(\varepsilon_s, \gamma_e; \varepsilon_\gamma) \,, \tag{30}$$

where $n_\gamma(\varepsilon_s)$ is the distribution of seed photons, and $N_e(\gamma_e)$ is the electron energy distribution, that can be expressed in terms of the $(dJ/dE)_e$ that is computed from our shock acceleration code: $N_e(\gamma_e) = [4\pi m_e c^2/v_e](dJ/dE)_e$. We use this expression with a blackbody photon distribution

$$n_\gamma(\varepsilon_s) = n_{BB}(\varepsilon_s) \equiv \frac{\varepsilon_s^2}{\pi^2 \lambda_c^3} \frac{1}{e^{\varepsilon_s/\Theta} - 1} \,, \quad \Theta = \frac{kT}{m_e c^2} \,, \tag{31}$$

with $T = 2.73$ K so that $\Theta = 4.6 \times 10^{-10}$. Here $\lambda_c = \hbar/(m_e c)$ is the Compton wavelength. This form of the blackbody distribution is most appropriate for gamma-ray applications, and is simply obtained (e.g. see Rybicki & Lightman 1979) from the more familiar textbook form that uses photon frequencies. By using the multi-component fit to background soft photon distributions in Figure 1 of Gaisser, Protheroe, & Stanev (1998), we determined that the CMB population contributes $\sim 90\%$ of the inverse Compton flux; for simplicity, hereafter, we use just this background in all our IC flux calculations.

3.4. Synchrotron Radiation

Using standard references such as Pacholczyk (1970) or Rybicki & Lightman (1979), the synchrotron emissivity from an electron Lorentz factor distribution $N_e(\gamma_e) = [4\pi m_e c^2/v_e](dJ/dE)_e$ can quickly be written down:

$$\varepsilon_\gamma \frac{dn_\gamma(\varepsilon_\gamma)}{dt} = \frac{\sqrt{3}}{2\pi} \alpha \frac{e B_\perp}{m_e c} \int_0^\infty N_e(\gamma_e)\, F(x)\, d\gamma_e \quad \mathrm{cm^{-3}\, s^{-1}} \,, \tag{32}$$

where

$$F(x) \equiv x \int_x^\infty K_{5/3}(z) dz \,; \quad x = \frac{\nu}{\nu_c} = \frac{\varepsilon_\gamma}{\varepsilon_c} \,, \tag{33}$$

is the well-known synchrotron spectral function for monoenergetic electrons, with $K_{5/3}$ being the modified Bessel function. Here $\varepsilon_c = 3.398 \times 10^{-14} B_\perp \gamma_e^2$ the critical synchrotron photon energy

($\nu_c = \varepsilon_c m_e c^2/(2\pi\hbar) = 4.199 \times 10^6 B_\perp \gamma_e^2$ is the critical frequency) for an electron of energy γ_e, with $B_\perp$ being the component of the magnetic field (in Gauss) perpendicular to the line of sight. For these calculations we assume that the magnetic field is highly tangled and essentially isotropic, as is indicated by the low polarized fractions observed at radio frequencies in most remnants (Reynolds & Gilmore 1993). We use Pacholczyk's tabulation of $F(x)$ to perform the integral numerically for shock acceleration distributions $N_e(\gamma_e)$, since commonly used approximations such as assuming that each electron radiates all its synchrotron power at ν_c can be poor for electron distributions with cutoffs (e.g. see Reynolds 1998).

4. RESULTS

The results of our calculations fall into two main categories. First, we discuss particle distributions generated by the Monte Carlo code: their evolution in the Sedov phase and issues of electron injection and cosmic ray production up to the "knee." Second, we present photon emission spectra, focusing first on predictions of gamma-rays, then considering the test case of the remnant IC 443, and finally extending the discussion to broad-band (radio to gamma-ray) spectra.

4.1. Particle Spectra During SNR Evolution

We first produce models where the environmental parameters are taken to be: $n_{p,1} = 1$ cm^{-3}, $\mathcal{E}_{SN} = 10^{51}$ erg, $M_{ej} = M_\odot$, and $B_1 = 3 \times 10^{-6}$ G. For these parameters, $V_{trans} \simeq 8.2 \times 10^3$ km s^{-1}, $R_{trans} \simeq 1.9$ pc, and $t_{trans} \simeq 90$ yr, and in addition, we have model parameters which we take to be $g = 1/r$ and $\eta = 10$. We compare results at three ages during the SNR lifetime: 300 years ($V_{sk} \simeq 4000$ km s^{-1}), 1000 years ($V_{sk} \simeq 2000$ km s^{-1}), and 10^4 years ($V_{sk} \simeq 490$ km s^{-1}). To obtain our steady-state shock solution, we must also know d_{FEB}. As indicated in equation (19), d_{FEB} depends on the shock compression ratio, r, and r is not known until the non-linear solution is found. Therefore, as we iterate toward a solution, changing both the shock structure and the overall compression ratio, d_{FEB} will be iterated with r using equation (19). For each of the three ages, we thus obtain the self-consistent shock structure and complete ion spectra which show the absolute injection and acceleration efficiency. With the additional parameter E_{crit} for electron injection and the observed downstream electron temperature, $T_{e,DS}$ (or our parameter f_e), we obtain the electron spectrum as well. The parameters for these models (a, b, and c) are listed in Table 1.

In Figure 4 we show the final smooth shock structure for the three ages with the parameters just listed. A fourth shock (heavy dotted line) will be discussed in Section 4.2 below. In each case, we have iterated to a solution for the shock profile, as well as the overall compression ratio, and the final smooth shock conserves (to within a few percent) mass, momentum, and energy fluxes at all positions from far upstream, through the nearly discontinuous subshock (at $x \sim 0$), into the downstream region where we hold all parameters constant (i.e. we do not include adiabatic

cooling). For a description of how the iteration process is performed, see Ellison & Reynolds (1991) or Ellison, Baring, & Jones (1996). The self-consistent compression ratios we obtain (see labels in Figure 4), which decline with $t_{\rm SNR}$, are well above the Rankine-Hugoniot value of four in all cases. The escape of particles at the FEB, as well as the lowering of the ratio of specific heats from the contribution of relativistic particles to the total pressure (see Ellison & Reynolds 1991), causes the increase in r. This increase is indicated by the downstream portions of the flow profiles where the test-particle speed (light dashed line) is $0.25\,V_{\rm sk}$ (i.e. $r = 4$), while the downstream flow speed for the non-linear shocks is always less than $0.25\,V_{\rm sk}$. For each age, the shock is smoothed on the diffusion length scale $\sim \kappa(E_{\rm max})/V_{\rm sk}$ of the highest energy particles in the system. This upstream precursor increases in size as the remnant evolves. Note that the distance scale is measured in units of $\eta\, r_{\rm g1}$, where $r_{\rm g1} = m_{\rm p} V_{\rm sk} c/(e\,B_1)$, so that distance *units* are proportional to $V_{\rm sk}$ and are different for each profile (see Table 1 for values of $d_{\rm FEB}$ in pc). Despite this extreme smoothing, a distinct subshock persists in all cases with an abrupt transition to the downstream state occurring over a length scale of about one thermal ion gyroradius. The subshock strength is the main determinant of the downstream thermal ion and electron temperatures.

In Figure 5 we plot omni-directional particle spectra, dJ/dE (i.e. particles per cm^2 per sec per steradian per MeV/A), obtained with the smooth shocks shown in Figure 4. This figure presents a time history of evolution of particle distributions during a remnant's expansion. In all panels, the solid and dashed histograms represent the proton and He^{+2} spectra, respectively, with the helium injected far upstream from the shock at cosmic abundances, i.e. $n_{\rm He,1}/n_{\rm p,1} = 0.1$. The shock structure is determined including the helium contribution self-consistently. All spectra are calculated in the shock reference frame at a position downstream from the shock, the region of enhanced density where the gamma-ray emission is expected to be greatest. The spectra here are all normalized such that $n_{\rm p,1} V_{\rm sk} = 1$ cm^{-2} s^{-1} ($n_{\rm p,1}$ is the far upstream proton number density). The number density per unit energy $N(E)$ is $(4\pi/v)dJ/dE$, where v is the particle speed. The dotted lines in Figure 5 are electron spectra accelerated by the same shock as the protons and helium (note that for electrons, the abscissa scale is energy, not energy per nucleon). Our approximation that the electrons are test particles will be valid as long as the e/p ratio at relativistic energies is much less than unity. All other assumptions concerning diffusion properties are the same for electrons and ions. Note that we have set $n_{\rm e,1} V_{\rm sk} = n_{\rm e,2} V_{\rm sk}/r = 1.2$ cm^{-2} s^{-1} (i.e., charge neutrality with fully-ionized helium is assumed), where $n_{\rm e,2}$ is the downstream number density of electrons and is calculated by integrating $(4\pi/v)dJ/dE$ over *all energies*. For all three electron examples, $E_{\rm crit} = 100$ keV and $f_{\rm e} = 1$.

The spectra in Figure 5 are "complete" in that they are entire distributions from thermal energies to the highest energies where the spectra turn over due to particles escaping at the FEB. Electron losses are not important in any of these examples, but we will show examples later where they are. The spectra possess an enhancement of He^{+2} that comes about because the smooth shock naturally accelerates particles with large mass-to-charge ratios more efficiently (e.g. Jones & Ellison 1991), as they possess longer diffusion lengths and therefore sample larger effective compression

ratios. This enhancement, which is discussed at length in Ellison, Drury, & Meyer (1997), permits He^{2+} to dominate the proton contribution to the energy density, except for the highest energies per nucleon. In general, and in agreement with other non-linear models (e.g. Berezhko, Yelshin, & Ksenofontov 1996), we find very high efficiencies, easily putting over 50% of the total energy density in particles above 1 GeV. Equally important, the contribution of He^{+2} to gamma-ray production is further enhanced by the factor in equation (26) and can be comparable to that from protons even though helium is injected far upstream with only 10% of the number density.

Another important feature of the spectra in Figure 5 is that they are not strictly power-laws (even if plotted on a momentum scale), but show an upward curvature, becoming harder at higher energies. This effect is masked somewhat for the ions because of the kinematic break at $\sim mc^2$, but shows up more dramatically for the electrons between $\sim$ 10 MeV and 10 GeV. The smooth shock, combined with our assumption that the upstream diffusion length is an increasing function of energy, causes high energy particles to be accelerated more efficiently than low energy ones, producing the upwardly curved spectra (e.g. Eichler 1984; Jones & Ellison 1991), and very different spectral shapes for protons and electrons below a few GeV. In general, when compared to test-particle results with $r = 4$, the non-linear spectra are considerably *steeper* at the lowest energies because of the weak subshock with compression ratios less than 4. At the highest energies, the non-linear spectra are flatter than the test-particle ones because the overall compression ratio is greater [2] than 4. At intermediate energies, between $\sim$ 1 MeV and 10 GeV (i.e. electron energies responsible for radio synchrotron emission), the non-linear spectra, particularly electrons, are considerably steeper than the test-particle predictions.

Finally, in Figure 5 the cutoff from the FEB occurs at energies proportional to the particle charge (equation 20) so the helium spectrum extends to a total energy a factor of two higher than the electrons or protons (a factor of two lower in energy per nucleon). Note also that in cases where electron cooling losses are important, cooling-generated structure can appear in the electron distribution just below the cutoff energy.

While our Monte Carlo implementation of non-linear shock acceleration uniquely includes the self-regulation of injection, giving the full ion spectrum self-consistently, some of the other results of our calculation will be properties of any non-linear shock model. In particular, the concave spectra will result in any modified shock if the diffusion length increases with energy, since more energetic particles will then see a larger effective compression ratio. Compression ratios larger than 4 should also always result from non-linear models that include particle escape, so that the asymptotic high-energy slope is flatter than the test-particle value.

---

[2]Note that the spectral indices at the highest energies, but below the cutoff from the FEB, are larger (i.e. the spectra are steeper) than $\sigma = (r+2)/(r-1)$, the value expected from unmodified shocks with a compression ratio of r. This is a purely non-linear effect from particle escape and our results are quite close to the analytic estimate of Berezhko (1996), i.e. $\sigma \simeq 3.5 + [(3.5 - r_{sub}/2)/(2r - r_{sub} - 1)]$. Malkov (1997) obtained a similar result.

4.2. Acceleration of Particles to 10^{15} eV

If SNRs are the main sources of galactic cosmic rays, they must be capable of accelerating ions up to at least $\sim 10^{15}$ eV where the so-called "knee" in the all-particle cosmic-ray spectrum is observed. Here we consider how acceleration to energies considerably higher than in our previous examples will influence the gamma-ray emission. This addresses the crucial question of whether shell-type remnants can both supply the observed galactic cosmic ray population and explain the emission from the handful of EGRET unidentified sources that have SNR associations. From equation (20) we see that $E_{\rm max}^{\rm size}$ will increase for increased magnetic field, increased $\mathcal{E}_{\rm SN}$, decreased ambient density, and/or decreased η. The sensitivity of the maximum energy to r, g, or $t_{\rm SNR}$ is relatively small. The dependence of $E_{\rm max}$ on density strongly suggests that it may be difficult for a given remnant to simultaneously generate cosmic rays out to the knee *and* radiate sufficiently to support the detections by EGRET.

To obtain a high maximum energy, we choose $\eta = 1$ (strong scattering), $g = 1/r$ (the scattering mean free path is inversely proportional to the plasma density), $n_{\rm p,1} = 10^{-3}$ cm^{-3}, $B_1 = 10^{-5}$ G, $\mathcal{E}_{\rm SN} = 10^{52}$ erg, and $M_{\rm ej} = 10 M_\odot$. These choices result in $V_{\rm trans} \simeq 8240$ km s^{-1}, $t_{\rm trans} \simeq 1950$ yr, and $R_{\rm trans} \simeq 41$ pc. Referring to Figure 3 (top curve), we determine our solution at $t_{\rm SNR} \simeq 4 \times 10^4$yr, near the peak in the maximum acceleration energy, where the acceleration changes from being time-limited to space-limited. This optimization gives a maximum energy of the cosmic rays of $E_{\rm max} \simeq 4 \times 10^{15}$ eV. At this age, $V_{\rm sk} \simeq 1340$ km s^{-1} and $R_{\rm sk} \simeq 137$ pc (Model *d* in Table 1), and our non-linear shock solution yields a compression ratio, $r \simeq 6.5$. Figure 3 shows that electrons will experience severe losses for these parameters, so that the contributions of bremsstrahlung and inverse Compton scattering at the highest energies will be suppressed. The maximum electron energy at $t_{\rm SNR} = 4 \times 10^4$ yr is about 3×10^{13} eV.

In Figure 6 we show the proton (solid line) and helium (dashed line) spectra for this cosmic ray knee energy example. We also depict the electron spectrum (dotted line) with $E_{\rm crit} = 0$ and $f_{\rm e} = 0.05$ (i.e. the electrons are injected with thermal distributions at $T_{\rm e,inj} = 1.0 \times 10^6$ K). These $E_{\rm crit}$ and $f_{\rm e}$ values have been chosen to provide an $(e/p)_{\rm 10GeV} \simeq 0.02$ consistent with cosmic ray observations (e.g. Müller et al. 1995). The cutoff in the electron spectrum from combined synchrotron and inverse Compton losses is clearly seen as is a slight pile-up of electrons just below the cutoff. Figure 6 reveals the important result that it is difficult to obtain much higher cosmic ray energies than these using normally-accepted ISM parameters. Significant juggling of the various parameters was necessary to increase $E_{\rm max}$ to above $\sim 10^{15}$ eV, including a requisite decrease in the density to an almost untenably low value. The accompanying increase in $E_{\rm max}$ came at the expense of large decreases in photon emissivity: pion decay and bremsstrahlung are proportional to $n_{\rm p,1}^2$ while inverse Compton is proportional to $n_{\rm p,1}$. Such trade-offs are inherent in the problem of simultaneously producing super-100 TeV cosmic rays and copious GeV-TeV gamma-ray emission in individual remnants. Hence, in accord with many previous expositions, we find it extremely difficult to generate cosmic rays beyond 10^{15} eV with normal Fermi acceleration in the homogeneous ISM.

The dotted line in Figure 4 shows the shock structure for Model *d* and it is quite different from the three other examples. The main reason for this, besides the much higher $E_{\rm max}$ and consequently, longer precursor, is the extremely low Alfvén Mach number that results from a high B_1 and a low ISM density. For this case, $\mathcal{M}_{\rm A} \simeq 2.3$, the Alfvén wave heating in the precursor is very strong, and $v_{\rm A}/V_{\rm sk} \simeq 0.5$. The combination of strong precursor heating and a high $v_{\rm A}$ (the scattering centers move through the upstream plasma at $v_{\rm A}$) results in a lowering of the acceleration efficiency and the overall compression ratio, which is only ~ 6.5 for this case. Furthermore, the subshock compression ratio is quite large; $r_{\rm sub} \simeq 4.4$. The combination of a large $r_{\rm sub}$ and relatively small r results in less shock smoothing than our previous examples which, in turn, results is little or no A/Q enhancement of helium over protons, as is evident in Figure 6.

4.3. Examples of Photon Production

In the top panel of Figure 7, we depict photon spectra produced by pion decay (dashed lines), bremsstrahlung (dot-dashed line), and inverse Compton scattering off the CMB radiation (dotted line) by particles with power-law momentum distributions, $dN/dp \propto p^{-2}$. We note that the p-He contribution to the pion decay emission is of the same shape as the p-p one illustrated, but with a simple multiplicative factor that combines the relative abundance of He and the factor in equation (26). Also, e-e bremsstrahlung contributes a virtually identical spectrum above 10 MeV to the e-p one shown. The "νF_ν" format of the figure is chosen to illustrate at what energy the peak power of the gamma-rays emerges. This depiction follows the work of Gaisser, Protheroe, & Stanev (1998), and to facilitate comparison with their results, we use the same spectral shape and normalization they use for their Figure 3, i.e.

$$\left(\frac{4\pi}{v}\right)\frac{dJ}{dE} = \frac{1}{V}\frac{dN}{d\mathcal{E}} = \frac{a}{V}\left(\frac{\mathcal{E}}{1\mathrm{GeV}}\right)\left(\frac{p}{1\mathrm{GeV/c}}\right)^{-3}\exp\left(-\frac{\mathcal{E}}{\mathcal{E}_{\rm cut}}\right) \quad \mathrm{GeV^{-1}\ cm^{-3}}\,, \qquad (34)$$

including an exponential cutoff with $\mathcal{E}_{\rm cut} = 80$ TeV. Here, $\mathcal{E}$ is the total particle energy, E is the kinetic energy, V is the volume of the emitting source, and the normalization of Gaisser et al. of $a/V = 1$ GeV^{-3} cm^{-3} for both electrons and protons is used (the electron to proton ratio is set to one at fully relativistic energies). For this example only, we neglect helium (or heavier ion species), as in Figure 3 of Gaisser et al. (1998). Alternatively, this distribution can be expressed as: $n(\gamma) = \mathcal{N}\gamma^{-2}\beta^{-3}\exp[-\gamma/\gamma_{\rm cut}]$, where γ is the particle Lorentz factor and the normalization constant is $\mathcal{N} = 1\ \mathrm{GeV}/(mc^2)$, i.e. $\simeq 1957$ for electrons and $\simeq 1.066$ for protons. A prominent feature of this particular example is that the radiation is dominated by inverse-Compton emission, which is intrinsically flatter than bremsstrahlung and pion decay radiation due to the Compton scattering kinematics. The relative importance of the various processes depends strongly on the ambient density, electron losses, and the (e/p) ratio, as discussed below.

The power-law portions of the particle distributions can be used to derive asymptotic limits as checks on our computations. For IC scattering, equation (7.31) of Rybicki & Lightman (1979) can be used to derive an analytic approximation to the spectrum. For e-p and e-e bremsstrahlung,

since both cross-sections asymptote to the expression for σ_1 in equation (A2) for ultrarelativistic electrons, this form can be integrated over the power-law to obtain $dn_\gamma(\varepsilon_\gamma)/dt \simeq 4\mathcal{N}\alpha r_0^2 c\,[7/2 + \log_e(2\varepsilon_\gamma)]\,\varepsilon_\gamma^{-2}$. For pion decay radiation, we note that well above threshold, the photon spectrum traces that of the parent proton population (e.g. see Baring & Stecker 1998), which results in an ε_γ^{-2} spectrum for the case in the top panel of Figure 7. The normalization of this tracing is called a *spectrum-weighted moment*, and is 0.16 for a γ^{-2} proton distribution (Gaisser 1990; see also Drury, Aharonian, & Völk 1994; Gaisser, Protheroe, & Stanev 1998). The asymptotic form for pion decay radiation is then $dn_\gamma(\varepsilon_\gamma)/dt \simeq 0.16\mathcal{N}\sigma_{pp\to\pi^0 X}\, c\,\varepsilon_\gamma^{-2}$. As $\gamma_{\rm cut} \to \infty$, our numerical results smoothly approach these asymptotic forms for all three processes, thereby providing confirmation that our integration routines were working correctly. Furthermore, we find good (though not perfect) agreement of our results with the curves in Figure 3 of Gaisser, Protheroe, & Stanev (1998), with the slight differences being attributable to assumptions made in the modeling of pion production and bremsstrahlung. Finally, note that Klein-Nishina corrections to inverse Compton scattering off CMB photons become important for electron energies exceeding around 20 TeV.

4.4. Gamma Ray Spectra and IC 443 as a Test Case

In the middle panel of Figure 7 we show the individual components for the $V_{\rm sk} = 2000$ km s^{-1} example of Figures 4 and 5 (Model *b*: $E_{\rm crit} = 100$ keV and $f_{\rm e} = 1$). In the lower panel we exhibit the photon emission for our extreme maximum energy example with $V_{\rm sk} = 1340$ km s^{-1} (i.e. Model *d*: Figure 6). It is clear that the relative importance of the various emission mechanisms can vary greatly depending on the parameters, with the two most important being the ambient density, $n_{\rm p,1}$, and the (e/p) ratio at fully relativistic energies, i.e. $(e/p)_{10\rm GeV}$. The cutoff energy, $E_{\rm max}$, is also important for fitting the constraints imposed by observations at TeV energies, and in particular the overall flux via more subtle feedback effects of the non-linearity of the Fermi acceleration process. It also influences the radio synchrotron cutoff which will be discussed below. The main determinant of $E_{\rm max}$ in our model is η, which is basically a free parameter within the broad range $1 \lesssim \eta \lesssim 100$, though evidence from a variety of origins suggests values of $\eta \sim 1 - 10$ apply to cosmic plasmas. In a particular source, it may be possible to restrict $n_{\rm p,1}$ somewhat from X-ray and gamma-ray observations and $(e/p)_{10\rm GeV}$ by EGRET observations (discussed below). An important feature of Model *b* is the importance of He^{2+} pion decay emission. The short dashed lines in Figure 7 show the gamma-ray emission from helium, while the long dashed lines show the contribution from protons. At photon energies below ~ 100 GeV, the helium contribution is approximately equal to the proton contribution for Model *b*. The same is not the case for Model *d* since little A/Q enhancement arises, as discussed above.

It is clear from the large number of parameters that only a limited amount of information will be obtained from fitting a particular source unless the parameters can be constrained either by better observations or improved understanding of the plasma physics of shock acceleration. Nevertheless, it is fruitful to investigate how the various parameters influence the overall photon spectrum. First, as

$n_{p,1}$ is *decreased*, the importance of inverse Compton increases relative to bremsstrahlung and pion decay since inverse Compton emission is proportional to the electron density, while bremsstrahlung and pion decay depend on the square of the ambient density. The strength of a pion decay bump at ~ 100 MeV gives important clues to $n_{p,1}$ and $(e/p)_{10GeV}$: a weak or non-existent bump implies a low $n_{p,1}$ and/or a large $(e/p)_{10GeV}$. The quality of the data in Esposito et al. (1996) for the EGRET unidentified sources with shell-type SNR "counterparts" is insufficient to confirm or exclude the existence of such a feature. For this reason, the approach of Gaisser, Protheroe, & Stanev (1998) in using this data to constrain the e/p ratio is presently unrealistic. Besides the existence (or otherwise) of a pion decay bump, the overall slope of the photon distribution gives information on the relative importance of inverse Compton radiation compared to bremsstrahlung since the inverse Compton component possesses a flatter slope. The cutoff energy, E_{max}, if it can be determined by TeV observations, also gives useful information: a low E_{max} implies some combination of large η, high $n_{p,1}$, and/or large $(e/p)_{10GeV}$. In principle, information on the background magnetic field strength can be obtained if electron losses become important and the electron spectrum cuts off at a lower energy than the proton spectrum, e.g. as in the bottom panel of Figure 7. In this case, the pion decay spectrum may extend beyond the inverse Compton and bremsstrahlung spectra and a spectral feature may be present. Furthermore, the consideration of X-ray synchrotron cutoffs (e.g. Reynolds 1996; Allen et al. 1997) can constrain **B**, and in conjunction with TeV gamma-ray data, can restrict the permissible regions of the density/magnetic field strength parameter space.

We now apply our model to one specific shell-type SNR with gamma-ray detections reported in the Esposito et al. (1996) collection, namely IC 443. While Gaisser, Protheroe, & Stanev (1998) also use γ Cygni as a test case, the likelihood that its counterpart EGRET source is truly associated with shell-related emission is reduced by the small EGRET error circle reported in Esposito et al. (1996), and all but discounted by the refined localization performed by Brazier et al. (1996). Hence, we regard γ Cygni as being a weak candidate for producing detectable shell-associated gamma-ray emission. Based on the discussion of Lozinskaya (1992), Gaisser, Protheroe, & Stanev (1998) estimate for IC 443 that the ambient density is $n_{p,1} \simeq 0.3$ cm^{-3}, the distance to IC 443 is about 1.5 kpc, the radius is about 10 pc, and the remnant age is $t_{SNR} \simeq 5000$ yr. With these parameters, we estimate (for standard SN parameters and expansion into a homogeneous medium, which is clearly not the case for IC 443) a current shock speed $V_{sk} \simeq 940$ km s^{-1} (Model e in Table 1), and an E_{max} somewhat below 10 TeV.

In Figure 8 we present a grid of nine models varying $n_{p,1}$ from 0.1 to 1 to 10 cm^{-3}, and $(e/p)_{10GeV}$ from 0.01 to 0.1 to 1. In these plots, we also depict the EGRET observations of the IC 443 region (2EG J0618+2234 data points: Esposito et al. 1996) plus the upper limits from the Whipple telescope (Buckley et al. 1997, see also Lessard et al. 1995) and the HEGRA array. Note that there exist upper limits above 10 TeV from the scintillator array experiment in Tibet (Amenomori et al. 1997); these are not displayed. All plots show the number of photons per cm^2 per sec incident at Earth (i.e., flux) assuming a standard normalization: a source at 1 kpc with an emitting volume of $V_{SNR} = 1$ pc^3. For the distance (1.5 kpc) and radius (10 pc) estimates of IC443

given above, the photon fluxes in Figure 8 should be multiplied by $\sim 10^3/(1.5)^2 \sim 400$ (assuming a fractional shell thickness of 0.1, or a volume filling factor of about 0.25). In all of these models, we use $B_1 = 3\mu$G and $\eta = 10$, noting that a higher B_1 or lower η would yield a higher cutoff energy.

In generating this range of emission spectra, we computed a single non-linear shock solution using the parameters just described (i.e. fixing $E_{\rm max}$) plus $E_{\rm crit} = 0$ and $f_{\rm e} = 1$ for the electron injection (i.e. Model *e* Table 1), and then simply scaled the electron spectral normalization to give the $(e/p)_{10\rm GeV}$ values quoted (this amounts to varying $E_{\rm crit}$ and $T_{\rm e,inj}$) and calculated the photon emission using the densities shown. This approximation will not be accurate for electrons well below 1 GeV, but the *shape* (as opposed to normalization) of the electron spectrum above GeV energies is insensitive to variations in Sedov solution parameters and $E_{\rm crit}$ and $f_{\rm e}$ for a given self-consistent shock solution; hence the gamma-ray components exhibited in Figure 8 are representative of results of self-consistent shock simulation runs. One caveat is that this is not entirely true for the $(e/p)_{10\rm GeV} = 1$ cases, since then it becomes necessary to include the effect of the electrons on the shock dynamics.

It is clear from this set of models that the lack of a prominent pion-decay bump centered at around 67 MeV in the EGRET data for IC 443 (true also for other sources listed in Esposito et al. 1996) can only be matched with $n_{\rm p,1} \gtrsim 3{\rm cm}^{-3}$ and $(e/p)_{10\rm GeV} \gtrsim 0.1$. This $(e/p)_{10\rm GeV}$ ratio is larger than is believed to be the case for galactic cosmic rays: $(e/p)_{10\rm GeV} \sim 0.02$ is inferred from the measured local cosmic ray abundances in the 1-10 GeV range (e.g. Müller et al. 1995), and also from modeling of the diffuse galactic gamma-ray background radiation (Bertsch et al. 1993; Hunter et al. 1997). Thus, the EGRET observations provide significant constraints on the modeling of IC 443. If $(e/p)_{10\rm GeV} \gtrsim 0.1$, then values of $n_{\rm p,1} \gtrsim 3$ cm^{-3} can provide an adequate fit to the *shape* of the observed EGRET spectrum. The slope of the EGRET data argues against parameter regimes that yield a dominant (flat) inverse Compton component, with bremsstrahlung possessing a spectral index appropriate to the data; such a conclusion applies to most of the EGRET unidentified sources in Esposito et al. (1996), and was made by Gaisser, Protheroe, & Stanev (1998). It's also clear from Figure 8 that our models predict fluxes slightly above the Whipple upper limit. However, if we had chosen a larger value of η (i.e., $\eta = 50$–100), or a lower magnetic field, the maximum energy would have been less and the Whipple point could have been comfortably accommodated. On the other hand, as we show below in Figure 9, virtually any $n_{\rm p,1} \gtrsim 1$ cm^{-3} predicts radio emission well below observed fluxes. While this might result if the γ-ray emission volume is considerably less than that inferred for radio, or if there is significant clumping of the magnetic field, it must be emphasized that all of the above conclusions are based on the assumption that the EGRET detection of IC 443 is of *shell-related emission* and this may not be the case.

It is important to note that all of the densities referred to in this paper (such as in Figures 7–10) with a subscript "1" are true upstream ISM values. The simulation produces downstream densities for use in the emissivity calculations, and these are the upstream ISM values multiplied by the total compression ratio. As such, we establish correct normalizations so that the photon emission spectra actually correspond to the stated ISM densities. This contrasts with the work of Gaisser,

Protheroe, & Stanev (1998), and Sturner et al. (1997), who used power-law distributions, with the stated ISM density being used as a *coefficient* for infinite power-laws; no connection between the power-law normalization and the ISM density can be made in these two papers. Drury, Aharonian, & Völk (1994) did introduce bounds to proton distributions, but chose lower limits around 1–10 MeV, well in excess of the thermal values expected from dissipational heating of shocks (e.g. see Figure 5). Thus, their normalizations (say at 1 GeV/nucleon) and corresponding photon fluxes are greater than ours — this can be seen by a comparison of Figure 4 of Drury et al. (1994) and the middle row of Figure 8 here.

4.5. Broad-Band Photon Spectra

Our focus so far has been gamma-ray emission from SNR shells. However, important information and constraints can be gained from broad-band studies of emission throughout the electromagnetic spectrum. This has been the approach of Mastichiadis & de Jager (1996) and de Jager & Mastichiadis (1997), who have examined the remnants SN1006 and W44. While non-thermal nucleons are only important for producing gamma-rays from pion decay, electrons produce photons from radio to gamma-ray energies. In Figure 9 we show all of the various photon spectral components from Model *e* (Table 1) that formed the basis for the array of examples in Figure 8. The individual components are again normalized to $d = 1$ kpc and $V_{\rm SNR} = 1$ pc^3, while the total photon emission (heavy solid line) has been multiplied by 500 for a rough match to the EGRET data. We depict radio and X-ray observations in addition to the previously illustrated EGRET, Whipple, and HEGRA data, but omit the OSSE upper limits in the 50 keV–1 MeV band that are presented in Sturner et al. (1997), since they do not significantly constrain our continuum spectra. It is important to emphasize that in this plot, we are not attempting a detailed fit to the data, but rather aiming to illustrate how the various components relate to one another.

There are several features to observe in Figure 9. First of all, for the particular density of this model ($n_{\rm p,1} = 0.3$ cm^{-3}), inverse Compton (dotted line) emission contributes to the spectral flattening in the EGRET range. Such a flattening, if seen in some source, is therefore not necessarily indicative of the presence of cosmic ray nucleons, unlike a pion decay bump. Second, normalizing the overall continuum to approximately match the flux level for the EGRET unidentified source 2EG J0618+2234 that is associated with IC 443 conflicts slightly with the Whipple upper limit but not the HEGRA array limit (note that the HEGRA imaging telescope upper limits at 500 GeV reported by Hess (1997) are comparable to those of Whipple). This result depends almost totally on the maximum energy obtained (i.e. equations [15], [17], and [20]) which, in turn, is a decreasing function of the parameter η. A large value of η could result from environment effects such as the SNR being contained in a partially ionized region, thereby permitting the shock acceleration model to comfortably accommodate the constraints imposed by atmospheric Čerenkov telescope measurements. Third, the electrons that produce the IC gamma-rays also generate the radio to optical synchrotron emission (light solid line) and the synchrotron spectrum does not extend into

the X-rays, due to the maximum electron energy being in the TeV range. As a consequence, it is actually the bremsstrahlung from non-relativistic electrons that dominates the X-ray signal. This could potentially provide an alternative explanation to synchrotron emission for the non-thermal X-rays seen in IC 443 (Keohane et al. 1997) and Cas A (Allen et al. 1997). We obtain X-ray indices (at around 10 keV) in the 2.3–2.7 range (e.g. see Figure 9), which would nicely describe the index ASCA obtained for IC 443, but are generally flatter than in the X-ray observations of Cas A and SN1006 (~ 3). Furthermore, the absence of X-ray lines in SN1006 (Koyama et al. 1995), normally excited by electron impact, indicates a paucity of electrons with energies of a few keV, whether from thermal or nonthermal distributions.

The flattening bremsstrahlung spectral shape at hard X-ray energies (e.g. see Figure 10 below) strongly contrasts with the sharpness of X-ray synchrotron cutoffs (Reynolds 1996), providing a potential observational discriminant; evidence for this steepening in RXTE data for SN1006 (Allen et al. 1998, in preparation), supports the synchrotron interpretation. However, we caution against automatically assuming that non-thermal X-rays from shells are synchrotron radiation. We can obtain quite steep X-ray bremsstrahlung spectra because of the curvature in the electron distribution that results from our non-linear treatment of the acceleration process; power-law distributions generate much flatter X-ray spectra (e.g. see Sturner et al. 1997), as suggested by the top panel of Figure 7. The curvature in the electron distribution disguises the break that naturally arises in the Bethe-Heitler cross-section at $\varepsilon_\gamma \sim m_e c^2$. It is evident in Figure 9 that the overall steepness of the bremsstrahlung spectrum precludes any attempt to simultaneously fit both EGRET and Ginga data.

Another obvious property of our particular model is that it falls well below the synchrotron radio spectrum of Erickson & Mahoney (1985), and as we mentioned above, this may imply that the γ-ray emission volume is considerably less than the radio. As for the spectral *shape* however, the model can reproduce the unusually flat (~ 0.35) synchrotron radio spectrum, as indicated by the upper dotted line in Figure 9, which is the synchrotron emission multiplied by 6×10^4. Such a flat radio spectral index is also present in W44 (though in virtually none other of the $\sim$ 200 Galactic shell remnants), and was used in the test-particle model of de Jager & Mastichiadis (1997) to argue that it is too flat to be explained by a shock-accelerated electron population. This is not necessarily the case, given that non-linear solutions to the Fermi acceleration problem can generate flat distributions (i.e. flatter than E^{-2}). However, the conjecture of de Jager & Mastichiadis (1997) that a pulsar may inject electrons with the required distribution via its relativistic wind, thereby circumventing the need to invoke Fermi acceleration at the remnant's outer shock, may still be correct. For IC 443, Sturner et al. (1997) retained shock acceleration, but included free-free absorption which produces a flattening at the lower radio frequencies roughly matching the radio data. Presumably, adding free-free absorption could also provide better compatibility between our model and the observed radio emission.

The usefulness of considering broad-band emission comes from the fact that a variation in any single model parameter impacts several wavebands. For example, the radio intensity depends on

the square of the magnetic field, B_1, but increasing B_1, also makes electron losses more severe, lowering the energies where the bremsstrahlung and IC emission cut off. Variations in the ISM density impact all wavebands. As density declines, the maximum particle energy increases, and the gamma-ray continuum extends to higher energies, but the overall flux at sub-TeV energies decreases accordingly. With lower densities the inverse Compton component becomes more prominent in the gamma-ray band, flattening the spectral index. This prominence was emphasized by Mastichiadis and de Jager (1996) and Pohl (1996) in their predictions that SN1006 would be a TeV gamma-ray source. As suggested by Mastichiadis and de Jager (1996), TeV upper limits or positive detections can constrain the parameter $\eta = \lambda r_g$ to values signifying departure from Bohm diffusion (i.e. $\eta \gg 1$). If steep X-ray emission is interpreted as coming from a synchrotron cutoff, this determines $E_{\rm max}^2 B$ and also a combination of B and the electron density. Through Equation (15), η therefore couples to B and the gamma-ray inverse Compton flux must anti-correlate with both B and λ/r_g. Hence lower bounds to η are derivable from TeV observational constraints. These features are illustrated by our cosmic ray knee example shown in Figure 10, whose particle distributions are exhibited in Figure 6.

In addition to all this, of course, is the fact that the SNR environment is likely to be far from homogeneous. Rayleigh-Taylor instabilities behind expanding SNR shocks (e.g. Jun & Norman 1996) may produce localized non-cospatial clumping of the magnetic field and/or density, as exemplified by the complexity of spatial maps of remnants such as Cas A, and different processes (e.g. radio synchrotron and pion-decay) may have different emission volumes. Furthermore, while we assumed that the remnant shock is everywhere plane-parallel, a given remnant shock is expected to be oblique over a sizable fraction of its surface where the downstream (interior to the shock) magnetic field and consequently the synchrotron emissivity are enhanced accordingly. Clearly, the surface brightness of the radio flux is highly sensitive to field or density clumping. Given the complexity of the situation and the interplay of the various parameters, we believe more will be learned about a particular source by combining a general fit to observations over the widest possible frequency band, with detailed fits to narrow band observations.

To conclude this subsection, we display in the top panel of Figure 11 our remnant evolutionary sequence (i.e. the spectra shown in Figure 5) in an $E^2 dN/dE$ format. This illustrates how the highest energy ions dominate the energy density of the system and emphasizes the differences in the electron and proton spectra. The spectra in the top panel are all normalized to $n_{\rm p,1} V_{\rm sk} = 1$ cm^{-2} s^{-1}, and since $V_{\rm sk}$ is decreasing, the population densities decline with time. If we assume, however, that the emission volume is $\propto R_{\rm sk}^3$, a remarkable property emerges. In the bottom panel of Figure 11 we show the total photon spectra with the emission volume set to $V_{\rm SNR} = R_{\rm sk}^3$ (corresponding roughly to a shell between $0.9 R_{\rm sk}$ and $R_{\rm sk}$) and the total emission flux at earth is approximately constant over the time span from 300 yr to 10^4 yr. This result is very similar to the behavior reported by Drury, Aharonian, & Völk (1994), whose time-dependent two-fluid model generated a more-or-less constant luminosity in the Sedov phase, and Berezhko & Völk (1997) (where the integrated γ-ray flux varies by less that a factor of 3 during $1 < t_{\rm SNR}/t_{\rm trans} < 100$) and probably results from the

evolutionary properties of the Sedov solution.

5. DISCUSSION

5.1. Previous Gamma-Ray Models

Reviews of previous models of gamma-ray emission from SNRs can be found in Baring (1997) and de Jager and Baring (1997). Briefly, Drury, Aharonian, & Völk (1994) calculated gamma-ray emission from protons using the time-dependent, two-fluid analysis (thermal ions plus cosmic rays) of Drury, Markiewicz, & Völk (1989). They assumed a power-law proton spectrum with an arbitrary maximum energy cutoff; no self-consistent determination of temporal or spatial limits to the maximum energy of acceleration was made. In some sense, our results can be considered complementary to those of Drury et al., since their model includes global spherical shock dynamics, but does not self-consistently yield an energetic particle spectrum, while our model provides a fairly self-consistent calculation of the total shock acceleration spectrum, but does not treat time-dependent dynamics in detail. We find that during much of Sedov evolution, maximal diffusion length scales are considerably less than a remnant's shock radius, concurring with the findings of Drury, Aharonian, & Völk (1994).

Gaisser, Protheroe, & Stanev (1998) computed emission from bremsstrahlung, inverse Compton scattering, and pion-decay from proton interactions and only slight differences exist between our treatment and theirs of the physics of bremsstrahlung and pion production processes, other than that we include helium. Gaisser et al. did not consider non-linear shock dynamics or time-dependence and assumed test-particle power-law distributions of protons and electrons with arbitrary e/p ratios. In order to suppress the flat inverse Compton component and thereby accommodate the EGRET observations of γ Cygni and IC443, Gaisser et al. assumed a high matter density to enhance the ratio of bremsstrahlung and π^0-decay flux to IC flux. We have shown (Figure 8) that the same effect can be achieved without a high density if the primary e/p ratio is reduced.

A time-dependent model of gamma-ray emission from SNRs using the Sedov solution for the expansion was presented by Sturner et al. (1997). They numerically solved equations for electron and proton distributions subject to cooling by inverse Compton scattering, bremsstrahlung, π^0 decay, and synchrotron radiation and included all the radiation processes of Gaisser, Protheroe, & Stanev (1998) plus synchrotron emission to supply a radio flux. Expansion dynamics and non-linear acceleration effects were not treated, and power law spectra were assumed. One feature of their model is the general dominance of inverse Compton emission. This arises because they often have the same energy density in non-thermal electrons and protons, thereby assuming high e/p ratios; this appears hard to reconcile with galactic cosmic ray observations. Sturner et al.'s work marks a significant advance over previous work by introducing cutoffs in the distributions of the accelerated particles (actually first done by Reynolds 1995, 1996; Mastichiadis & de Jager 1996; de Jager & Mastichiadis 1997), which are defined by the limits on the achievable energies in Fermi acceleration

discussed in Section 2.3. Hence, given suitable model parameters, Sturner et al. can accommodate the constraints imposed by Whipple's upper limits to γ Cygni and IC 443.

To date, the most complete model coupling the time-dependent dynamics of the SNR to cosmic ray acceleration comes from Berezhko & Völk (1997) (based on the model of Berezhko, Yelshin, & Ksenofontov 1996). They numerically solve the gas dynamic equations including the cosmic ray pressure and Alfvén wave dissipation, following the evolution of a spherical remnant in a homogeneous medium. Only pion decay is considered and the gamma ray spectra, spatially integrated over the remnant, exhibit some curvature. There are a number of similarities between this model and ours; we both obtain maximum efficiencies near and above 50% and we both obtain overall compression ratios well above standard Rankine-Hugoniot values. However, Berezhko & Völk argue that systems will naturally be driven to the Bohm limit (i.e. $\eta \sim 1$), giving them higher upper limits to the maximum cosmic ray energy than we estimate. Another important difference between our work and Berezhko & Völk's, comes from the treatment of particle injection: while this is automatic in our Monte Carlo technique, affording an elegant connection between the thermal and non-thermal populations, it is specified by a free parameter in Berezhko & Völk (1997). Berezhko & Ellison (1998, in preparation) demonstrate that, for most parameter regimes of interest, the shock dynamics are relatively insensitive to the efficiency of injection, and furthermore that there is good agreement between the two approaches when the Monte Carlo output specifies injection for the model of Berezhko et al. Output particle spectra produced by the two models are then essentially identical for a remnant's free-expansion phase, though minor differences do arise during the Sedov phase because our Monte Carlo model does not include the influence of particles accelerated prior to the Sedov phase. A significant advance in our work here is the inclusion of electrons.

5.2. The Observational Status Quo

Several questions of interest are raised by the current observational situation, the first being how real are the proposed associations between EGRET unidentified sources and young shell-type remnants like IC 443, W44, γ Cygni, W28, the Monoceros Loop, and CTA 1 (Sturner & Dermer 1995; Esposito et al. 1996; Yadigaroglu & Romani 1997)? Second, if the associations are true, is the gamma-ray emission connected with particle acceleration at the shell? Furthermore, is the signal above 100 MeV produced by cosmic ray ions or electrons?

The sources detected so far above a few hundred GeV are the nebulae surrounding several pulsars, namely the Crab, Vela, PSR 1706-44 and PSR 1509-58, and the high latitude supernova remnant SN1006. With the exception of SN1006, these are likely to be associated with plerionic emission. The situation is, however, more confused in the GeV and sub-GeV ranges. The candidate associations identified by Esposito et al. (1996) all suffer from large uncertainties in the EGRET source positions, localizations that were derived using the point-source assumption. Statistically, the chance probability of spatial coincidence with the candidate remnants is small: 0.1% for IC 443, 1.4% for γ Cygni, 6% for W28, and 7.4% for W44 (Yadigaroglu & Romani 1997). Yet, these

remnants are often found in active star-forming sites, amid numerous massive stars and HII regions, and the chance probability of associating the EGRET source with a close-by OB star or a radio pulsar is equally small or even smaller (Yadigaroglu & Romani 1997). For the unidentified EGRET source 2EG J1801-2312, for example, the chance probability of an association with the OB star Sgr 1c or the pulsar PSR B1758-23 is 1.2% instead of 6% for the remnant W28. The relative dimensions of the remnant and of the gamma-ray error circle may also raise difficulties for the identification of EGRET sources with known remnants. The 95% confidence positions of 2EG J0008+7307 and 2EG J2020+4026, as measured at GeV and super-GeV energies (Brazier et al. 1996, 1998), are constrained to within 11 and 8 arcmin, respectively, so that the sources appear unmistakeably *inside* their respective remnants, namely CTA 1 and γ Cygni, which are much larger. Furthermore, note that systematic errors in the gamma-ray position due to the highly structured background along the lines of sight to the candidate remnants are very likely. These can be reduced by taking advantage of the narrower angular resolution of EGRET above 1 GeV, given the significant flux of the candidates sources above this energy. Reimer et al. (1997) recently adopted this approach to determine more accurate positions that differ by 1 or 2σ from the positions listed in the 2nd EGRET catalogue (Thompson et al. 1995).

Such improved locations led Brazier et al. (1996) to conjecture that 2EG J2020+4026 is perhaps associated with a distinct ROSAT source with no optical counterpart that lies within the EGRET error box: they suggest that this source may be a radio-weak pulsar or a plerion. There is also the recent proposal (Brazier et al. 1998) of a pulsar/plerion counterpart to the CTA 1 remnant's EGRET source 2EG J0008+7307. In addition, de Jager & Mastichiadis (1997) contend that the EGRET source 2EG J1857+0118 associated with W44 may be of plerionic nature due to the presence of a radio pulsar and its wind nebula within the 95% EGRET confidence circle. A pattern seems to be emerging, namely that pulsars or plerionic activity may generate the gamma rays in half of the remnants tentatively associated with EGRET sources. The statistical conceivability that pulsars could account for *most* of the unidentified EGRET sources near the Galactic plane (Kaaret & Cottam 1996; Yadigaroglu & Romani 1997; Mukherjee, Grenier, & Thompson 1997) currently precludes any assertion stronger than just weak suggestions of GeV emission from two shell remnants, namely IC 443 and W 28. For this reason, we have used only data for 2EG J0618+2234 in association with IC 443 in some of our spectral plots, principally as a general guide for the reader in considerations of the emission mechanism.

The spectral properties of the EGRET detections cannot presently determine whether the emission is of ionic or electronic origin. All of the candidate remnants except the source toward CTA 1 present differential photon spectra in the EGRET band quite consistent with E^{-2} (Merck et al. 1996), the source toward CTA 1 being much harder ($E^{-1.58\pm0.18}$, Brazier et al. 1998). Based on the spectra presented in this paper, it seems probable that these slopes exclude inverse Compton emission as the dominant mechanism operating, and furthermore that pion decay emission is not overwhelmingly prevalent. Since all of the candidates are known to have massive clouds in their vicinity and, in some cases, to interact with molecular clouds, perhaps the very proximity of such

gaseous regions can cast light upon the nature of the energetic particles. Besides H_2 line emission, OH maser emission, collisionally excited by H_2 molecules heated by a non-dissipative shock, acts as a good tracer of shock/cloud interactions. In this respect, it is interesting to note that the three closest remnants with OH masers, namely IC 443, W28, and W44, belong to the candidate gamma-ray list (Claussen et al. 1997). The Monoceros loop and γ Cygni are also classical examples of remnants colliding with clouds (Pollock 1985; Huang & Thaddeus 1986). While Drury, Aharonian, & Völk (1994) concluded that, in the EGRET energy range, π^0 decay gamma rays in a 1 cm^{-3} medium would be drowned in the diffuse Galactic emission, the proximity of large target masses may give support to a cosmic-ray origin of the emission and its visibility. Sturner & Dermer (1995) showed that π^0 decay emission meets the bulk energy requirements for IC 443. But enhanced bremsstrahlung gamma-ray emission in the compressed gas has also been advocated by Pollock (1985) to account for the COS-B sources seen toward γ Cygni and W28. Hence, the mere presence of clouds cannot resolve the ambiguity between electronic and hadronic emission.

The complexity of the morphology and broad-band emission properties of shell-type remnants, as exemplified by IC 443, currently precludes a comprehensive understanding of the relationship of shell-associated shock acceleration to the various emission components. However there is one distinctive property of radio emission that can be discussed concisely, namely the observation that the radio spectral index flattens from 0.7–0.6 to around 0.3 with increasing brightness across IC 443 (Green 1986). This correlation is consistent with our model: with increasing density, there is less pressure in the highest-energy particles and the subshock compression ratio increases toward the canonical value of 4. Therefore, the radio-emitting (GeV band) electrons, which sample the length scales not dramatically larger than those on which the subshock is established, present a flatter spectrum concomitant with a rise in synchrotron luminosity. However, it should be noted that while modified shocks can in principle provide radio synchrotron spectra flatter than 0.5, it is difficult (but not impossible) for our model to explain such a large amplitude in spectral index variations in one source.

Turning now to the TeV band, the possibility of either shell-related or plerionic origin of gamma-rays from the EGRET sources quickly propelled the TeV gamma-ray astronomy community into an observational program. The absence of any positive detections from the ensuing monitoring of sources in the Esposito et al. collection, or from other prominent remnants such as Tycho, spawned a number of potentially constraining upper limits first from the Whipple team (Lessard et al. 1995, updated in Buckley et al. 1997), and then from HEGRA (Prosch et al. 1995; Hess 1997 for IC 443; and Prosch et al. 1996 for γ Cygni). As discussed earlier in the results section, SNR shells can generate GeV gamma-rays at flux levels that would be detectable by EGRET without conflicting with TeV upper limits if the SNR resides in a region of the ISM of moderate to high density ($n_{p,1} \gtrsim 1\,cm^{-3}$). Hence, dense remnant environs, as might be expected for most of the low galactic latitude sources in the Whipple and HEGRA surveys, might result in luminous emission in the sub-GeV range coupled with a simultaneous absence of TeV gamma-rays.

Not surprisingly, the first reported detection of probable shell-related TeV emission from a

remnant came from an entirely different type of SNR, SN1006, a southern hemisphere source at high galactic latitude that was accessible to the CANGAROO experiment (Tanimori et al. 1997, described in detail in Tanimori et al. 1998). This impressively symmetric barrel-shaped remnant (see Moffett, Goss, & Reynolds 1993, for example, for a radio image) is probably embedded in a low density, unclumpy medium, presumptions based upon its geometrical symmetry and its high latitude. This source had recently provided the first evidence of the presence of super-100 TeV electrons in SNR shells via the observation (Koyama et al. 1995) of non-thermal X-ray emission by ASCA. Its low environmental density (possibly $\lesssim 0.1\,\mathrm{cm}^{-3}$) clearly enhances the plausibility of Fermi acceleration to such high energies (as described in Section 2.3 here). This fact, combined with the ASCA discovery, prompted Mastichiadis & de Jager (1996) and Pohl (1996) to predict a strong inverse Compton signal in the TeV band for SN1006, motivated by the comparative efficiency of this process. It seems probable that the TeV signal from SN1006 is inverse Compton emission, and therefore confirms the production of cosmic ray electrons by a SNR blast wave, but offers little evidence for cosmic ray ions. The picture for SN1006 is not entirely simple: Tanimori et al. (1998) note that their data is strongly asymmetric, with a positive detection of a flux of $\sim 4.6 \times 10^{-12}$ $\mathrm{cm}^{-2}\ \mathrm{s}^{-1}$ at energies greater than around 1.7 TeV from the NE rim, and an upper limit of less than half this value for emission from the SW rim of the shell. CANGAROO is the first atmospheric Čerenkov telescope to possess such angular resolution capabilities, a property that is crucial to the inference of the shell association of the emission, and which will form a major goal for future experimental design. We note that the recent suggestions of non-thermal super-10 TeV electrons from X-ray observations of Cas A (Allen et al. 1997), IC 443 (Keohane et al. 1997) and W44 (Harrus et al. 1997) may identify them as prime candidates for future searches with atmospheric Čerenkov telescopes.

5.3. Super-TeV Cosmic-Ray Production in Gamma-Ray SNRs?

Two questions are of paramount importance to cosmic ray physicists. First, can individual supernova remnants simultaneously generate GeV gamma rays detectable by EGRET *and* produce cosmic rays to energies above $\sim 10^{14}$ eV? Second, if not, could some remnants be gamma-ray bright while others supply the cosmic ray population? We believe the answer to the first question may be no. Generally, for SNRs in a homogeneous environment, the circumstances that favor intense gamma-ray production in the EGRET and sub-TeV bands (namely high ISM density) limits acceleration of particles to energies well below the knee. Given the total lack of detections in the TeV band of remnants with associated EGRET unidentified sources, combined with the only positive TeV detection coming from a source (i.e. SN1006) with no associated EGRET emission, there seems little doubt that there is an anti-correlation between sub-10 GeV gamma-ray luminosity and super-10 TeV cosmic ray production in individual sources.

For the supernova remnant population as a whole, the situation is much less clear, and the second question above remains open. If those remnants associated with EGRET sources are actually

emitting at such intensities, which may be unlikely given the discussion just above, then they may well represent a bright minority of cosmic-ray producing remnants. Their peculiarity may be coupled to their unusually dense environments (as deduced from optical and microwave band observations), thereby enhancing sub-TeV gamma-ray emission. Thus, since the pion-decay bump at $\sim$ 70 MeV cannot be determined with current EGRET data, there is still no direct for the acceleration of cosmic ray *ions* to energies of 100 TeV or above. However, whether or not any of the EGRET detections amount to observations of shell-related emission, the contention that the vast majority of shell-type remnants can produce cosmic rays out to the knee still remains tenable. It is also possible that the remnants with EGRET identifications may actually be quite representative of the SNR population as a whole, producing energetic cosmic rays, but emitting at flux levels below EGRET's sensitivity; in such a case, alternative origins for the EGRET sources must be sought.

5.4. Issues and Prospects for TeV Gamma-Ray Astronomy of Shell Remnants

Several issues surrounding the comparison of our models with data require clarification. First, we remind the reader that the curves depicted in Figures 8–11 are arbitrarily normalized to an emitting region of 1 pc^3. It is unlikely that the gamma-ray emission in any real source would be confined to such a small volume. The actual angular size of a source affects the detection sensitivity: the sensitivities of telescopes like Whipple and HEGRA are typically 3-4 times better for sources smaller than a few tenths of a degree, which they see as point-like, than for extended ones ($\gtrsim 0.5°$) due to better hadron-rejection capabilities and associated improved sensitivities. Therefore, strictly, the model results for the various components in these figures should be compared with upper limits pertaining to point-sources. However, we note that such subtleties make little impact on most comparisons, since small emission volumes underpredict both point and extended source bounds in the TeV band. Second, observational upper limits are generally *integral limits* above a threshold energy, obtained by assuming a power-law spectrum (typically E^{-2}) for the underlying source. Hence they cannot strictly be compared with flux spectra, but we chose to do so remembering that such upper limits, and their associated flux bounds, may vary with spectral assumptions by factors of at most 2–3. It should be borne in mind that if the source spectra are steeply declining with energy in the sub-TeV and TeV band, as is suggested by a number of our models, then the sensitivity of atmospheric Čerenkov telescopes to such sources drops and the upper limits rise accordingly.

The CANGAROO observations of SN1006 have dramatically bolstered the prospects for future positive detections in the 0.3–1 TeV range, but these will depend on telescope sensitivity, threshold energy, and angular resolution. Improved sensitivities and lower thresholds in future experiments such as CAT (Rivoal 1997), HESS (Hofmann et al. 1997), VERITAS (Weekes et al. 1997), and MAGIC (Lorenz 1997) are obviously desirable requirements. For example, it is anticipated (Aharonian et al. 1997) that the HESS experiment should achieve a conservative 5σ upper limit on IC443 of $3 \times 10^{-12}\,cm^2\ s^{-1}$ above 100 GeV, assuming an emitting region of 0.4° in radius, almost

an order of magnitude below the $\gtrsim 250\,\mathrm{GeV}$ limits of Whipple (Buckley et al. 1997) depicted in Figures 8–11. Given the general property of rapidly declining spectra near the maximum energies of emission in most of our models, lower thresholds are of paramount importance. At the same time, our models and those of Drury, Aharonian, & Völk (1994), yield luminosities that scale with the source volume so that the *total flux* from remnants is virtually constant in time during the Sedov phase (as in Figure 11). Limb-brightening concentrates this flux somewhat towards the extremities of the remnant, less for IC emission than for the other three processes (due to their different density-dependences: this could provide an observational discriminant among the emission mechanisms as gamma-ray imaging capabilities improve). However, as long as the remnant evolution remains roughly self-similar, the surface brightnesses of both rims and remnant interiors will decline similarly with age (basically as $R_{\mathrm{sk}}^{-2} \sim t_{\mathrm{SNR}}^{-4/5}$), so that detectability should be enhanced in younger remnants.

Of equal or greater importance to the resolving of some of the open questions surrounding gamma-ray emission from supernova remnants will be improved telescope angular resolution. This was emphasized by the ability of CANGAROO to unequivocally connect its reported TeV flux from SN1006 to the NW rim of the remnant, a feat that was not generally possible for the EGRET data on other remnants. The most detailed study of the angular resolution for future telescopes is found in Aharonian et al. (1997), with estimates varying from a 0.1° radius for 68% acceptance for gamma rays at 100 GeV down to 0.05° at 1 TeV. This implies that spatial features of the order of 1 to 2 pc that are 1 kpc distant could, in principle, be resolved given reasonable data accumulation times. The CAT, HESS, and VERITAS telescopes will both have angular resolutions close to this. One big difference between the existing single dish telescopes (e.g. CAT, WHIPPLE, CANGAROO, etc.) and future stereo arrays is with the improved hadronic background rejection (as demonstrated by HEGRA, the only existing stereo experiment). An improvement by a factor of 10 to 20 is afforded by stereoscopic techniques, which directly translates into an increase in sensitivity by a factor of ~ 4. Given additional bonuses such as greater mirror area and/or finer imaging resolution, sensitivity increases of factors of 5 to 6 may be attainable. The unquestionable scientific impact of resolving gamma-ray SNR emission should amply motivate developmental programs towards achieving this technical goal.

6. CONCLUSIONS

In this paper we have applied a well-documented and tested steady-state Monte Carlo simulation of non-linear Fermi acceleration at plane-parallel shocks to the problem of gamma-ray and broad-band emission from shell-type supernova remnants. By coupling the simulation to a standard Sedov model, which estimates the spherical shock dynamics as a function of remnant age in a homogeneous environment, we have obtained a reasonably self-consistent description of a spherical SNR as it evolves and accelerates particles. A simple parametric model of electron injection and acceleration allows us to determine, for the first time, complete shock accelerated ion (proton and helium)

and electron distributions, and to use them to predict broad-band emission from synchrotron, pion decay, bremsstrahlung, and inverse Compton processes from radio through the X-ray continuum into the super-TeV gamma-ray band. The uncertainty in ISM parameters provides a broad range of model predictions for individual sources.

Our principal results are as follows. (1) We comprehensively treat non-linear feedback effects between accelerated particles and the shock structure that result in particle spectra (both ion and electron) which deviate significantly from power-laws. Such deviations are not only crucial to overall efficiency considerations, but also impact photon intensities and spectral shapes at all energies, producing GeV/TeV intensity ratios that are quite different from test particle predictions. (2) We address the electron injection problem in the context of SNRs with a simple and coherent prescription for connecting observational inferences of the e/p ratio to quantities that relate to plasma wave and dissipational properties of the shock. The treatment of electrons is particularly important in the light of the recent observations of SN1006, since it now appears that emission (X-ray and TeV gamma-ray in addition to radio) from cosmic ray electrons may dominate those from ions in some (or perhaps most) shell-type remnants. (3) We connect, in a reasonably self-consistent way, the spectral shape and intensity of gamma-ray emission to the ISM density without arbitrary coefficients of infinite or semi-infinite power-laws, and for ions, without ad-hoc injection parameters. (4) We determine the relative acceleration efficiencies of different ion species and find that, generally, the pion-decay contribution from helium (at cosmic abundances) is *comparable to that of protons*, a byproduct of the enhancement of heavy ions in non-linear Fermi acceleration. (5) Our results exhibit a general *anti-correlation* between the maximum energy of gamma-ray emission, and the source luminosity in the super-MeV band; this should be a property of any self-consistent model of particle acceleration and associated radiation at SNR shocks. (6) Finally, we also describe the parameters required to give maximum particle energies of a few TeV for ISM densities near ~ 1 cm^{-3}, so as to provide spectral consistency with current upper limits from the Whipple and HEGRA atmospheric Čerenkov telescopes for remnants with unidentified EGRET source associations. These parameters are fully consistent with Fermi shock acceleration and do not produce unacceptably steep particle spectra. At the same time, we can generate models with low densities (i.e. $n_1 \lesssim 0.01$ cm^{-3}) that accelerate cosmic rays to above 100 TeV, but with fluxes below the EGRET and Whipple sensitivities in the 100 MeV–10 TeV band.

While the results we present here are still preliminary in many ways, we believe they form a basis for future studies of non-linear shock acceleration and gamma-ray emission from shells of supernova remnants. Unresolved issues include the radial extent of emission, the modeling of flat spectrum radio sources, spatial variations in radio, X-ray and gamma-ray spectral indices, the physical processes responsible for the non-thermal X-ray and gamma-ray flux, the role of field obliquity around the shell, the e/p ratio and a more complete description of electron injection, and cosmic ray abundances and production up to the knee. Such studies would anticipate the development of the next generation of space- and ground-based gamma-ray telescopes with greater flux sensitivity and spatial resolution.

We thank Frank Jones for many insightful discussions on shock acceleration and its application to SNRs, and Joe Esposito, Jonathon Keohane, and Glen Allen for informative discussions on the EGRET unidentified sources, and on X-ray and radio observations of remnants. We also thank the anonymous referee for comments helpful to the improvement of the manuscript. DCE and MGB thank the Service d'Astrophysique, CE-Saclay, for hospitality during part of the period when this work was performed. This work was supported by the NASA Space Physics Theory Program.

A. APPENDIX

APPROXIMATIONS TO ELECTRON-ELECTRON BREMSSTRAHLUNG

In this Appendix, we present approximations to the differential cross-section for electron-electron bremsstrahlung that expedite our computations, circumventing use of the unwieldy and lengthy exact results for this process given in Haug (1975). Consider first the relativistic case. We adapt the approximation derived by Baier, Fadin, & Khoze (1967) which has the form

$$\sigma_{e-e}(E_e, \varepsilon_\gamma) \;=\; (\sigma_1 + \sigma_2)\; A(\varepsilon_\gamma, \gamma_e)\;, \tag{A1}$$

where $\gamma_e = (E_e + m_e c^2)/m_e c^2$ is the electron Lorentz factor,

$$\sigma_1 \;=\; \frac{4 r_0^2 \alpha}{\varepsilon_\gamma}\left[1 + \left(\frac{1}{3} - \frac{\varepsilon_\gamma}{\gamma_e}\right)\left(1 - \frac{\varepsilon_\gamma}{\gamma_e}\right)\right]\left\{\log_e\left[2\gamma_e \frac{(\gamma_e - \varepsilon_\gamma)}{\varepsilon_\gamma}\right] - \frac{1}{2}\right\}\;, \tag{A2}$$

and

$$\sigma_2 \;=\; \frac{r_0^2 \alpha}{3\varepsilon_\gamma}\begin{cases} \left[16(1 - \varepsilon_\gamma + \varepsilon_\gamma^2)\log_e\left(\dfrac{\gamma_e}{\varepsilon_\gamma}\right) - \dfrac{1}{\varepsilon_\gamma^2} + \dfrac{3}{\varepsilon_\gamma} - 4 + 4\varepsilon_\gamma - 8\varepsilon_\gamma^2\right. \\ \quad \left. -2(1 - 2\varepsilon_\gamma)\log_e(1 - 2\varepsilon_\gamma)\left(\dfrac{1}{4\varepsilon_\gamma^3} - \dfrac{1}{2\varepsilon_\gamma^2} + \dfrac{3}{\varepsilon_\gamma} - 2 + 4\varepsilon_\gamma\right)\right]\;, & \varepsilon_\gamma \le \frac{1}{2}\;, \\ \dfrac{2}{\varepsilon_\gamma}\left[\left(4 - \dfrac{1}{\varepsilon_\gamma} + \dfrac{1}{4\varepsilon_\gamma^2}\right)\log_e(2\gamma_e) - 2 + \dfrac{2}{\varepsilon_\gamma} - \dfrac{5}{8\varepsilon_\gamma^2}\right]\;, & \varepsilon_\gamma > \frac{1}{2}\;. \end{cases} \tag{A3}$$

Here $r_0 = e^2/(m_e c^2)$ is the classical electron radius, $\alpha \simeq 1/137$ is the fine structure constant, and the ultrarelativistic result of Baier, Fadin, & Khoze (1967) sets $A(\varepsilon_\gamma, \gamma_e) = 1$.

As it stands, this expression is accurate only for ultrarelativistic energies: this can be deduced from Figure 10 of Haug (1975), though it appears that Haug's numerical computations of Baier, Fadin, & Khoze's formula are slightly in error. Therefore, we add a mildly relativistic correction factor to equation (A1):

$$A(\varepsilon_\gamma, \gamma_e) \;=\; 1 - \frac{8}{3}\frac{(\gamma_e - 1)^{1/5}}{\gamma_e + 1}\left(\frac{\varepsilon_\gamma}{\gamma_e}\right)^{1/3}\;. \tag{A4}$$

With this factor included, our expression for σ_{e-e} is well within 10% of the exact result of Haug (1975) for electron energies above 5 MeV.

Equation (A1) is suitable for the consideration of bremsstrahlung contributions to gamma-rays from SNRs. However, it becomes inappropriate for X-ray and lower energies as the electrons become non-relativistic. In such regimes, we adopt a modification of the standard non-relativistic asymptotic forms obtained by Fedyushin (1952) and Garibyan (1953). In the rest frame of the ISM electrons, their expression for the angle-integrated differential (in photon energy) cross-section is

$$\sigma_{NR} \;=\; \frac{4 r_0^2 \alpha}{15\varepsilon_\gamma}\, F\!\left(\frac{4\varepsilon_\gamma}{\gamma_e^2 - 1}\right)\;, \qquad 0 < \varepsilon_\gamma < \frac{1}{4}(\gamma_e^2 - 1)\;, \tag{A5}$$

where, for $0 < x < 1$,

$$F(x) = B(\gamma_e)\left[17 - \frac{3x^2}{(2-x)^2} - C(\gamma_e, x)\right]\sqrt{1-x} + \left[12(2-x) - \frac{7x^2}{2-x} - \frac{3x^4}{(2-x)^3}\right]\log_e \frac{1+\sqrt{1-x}}{\sqrt{x}}\,, \tag{A6}$$

specifically with $B(\gamma_e) \equiv 1$ and $C(\gamma_e, x) \equiv 1$ for extreme non-relativistic energies. Haug (1975) notes that such a form is accurate to a few percent for cosmic ray electron energies below around 10 keV. Accordingly, we add the mildly-relativistic correction factors

$$B(\gamma_e) = 1 + \tfrac{1}{2}(\gamma_e^2 - 1) \;\; ; \;\; C(\gamma_e, x) = \frac{10x\,\gamma_e\beta_e(2+\gamma_e\beta_e)}{1 + x^2(\gamma_e^2 - 1)}\,, \tag{A7}$$

which render the cross-section in equation (A5) accurate (compared with Haug's numerical evaluations of the full cross-section) to within 10% for $E_e < 500\,\mathrm{keV}$, and is also of comparable accuracy for all but the highest photon energies (which yield insignificant contributions to the total bremsstrahlung spectrum) for E_e up to a few MeV. Hence, equations (A5)–(A7), together with equations (A1)–(A4), provide a description of σ_{e-e} that is suitable for the purposes of this paper, for all E_e; we switch between the two asymptotic regimes at $E_e = 2\,\mathrm{MeV}$.

REFERENCES

Achterberg, A., Blandford, R. D., & Reynolds, S. P. 1994, A&A 281, 220.

Allen, G. E. et al. 1997, ApJ 487, L97..

Aharonian, F. A., Hofmann, W., Konopelko, A. K & Völk, H. J. Astropart. Phys. 6, 369.

Amenomori, M., et al. 1997, Proc. 25th ICRC (Durban), 3, 209.

Baier, V. N., Fadin, V. S. & Khoze, V. A. 1967, Sov. Phys. JETP 24, 760.

Balogh, A., et al. 1993, Adv. Space Sci. 13(6), 15.

Baring, M. G. 1997, in Proc. of the Moriond Workshop on Very High Energy Phenomena in the Universe, ed. Trân Thanh Vân, J., et al. (Éditions Frontières, Paris), p. 97, 107.

Baring, M. G., Ellison, D. C. & Jones, F. C. 1993, ApJ 409, 327.

Baring, M. G., Ellison, D. C. & Jones, F. C. 1994, ApJS 90, 547.

Baring, M. G., Ogilvie, K. W., Ellison, D. C., & Forsyth, R. J. 1997, ApJ 476, 889.

Baring, M. G. & Stecker, F. W. 1998, in preparation.

Bell, A. R. 1978, MNRAS 182, 147.

Berezhko, E. G. 1996, Astropart. Phys. 5, 367.

Berezhko, E. G., & Ellison, D. C. 1998, in preparation.

Berezhko, E. G., & Völk, H. J. 1997, Astropart. Phys. 7, 183.

Berezhko, E. G., Yelshin, V., & Ksenofontov, L. 1994, Astropart. Phys. 2, 215.

Berezhko, E. G., Yelshin, V., & Ksenofontov, L. 1996, Sov. Phys. JETP 82, 1.

Bertsch, D. J., et al. 1993, ApJ 416, 587.

Bethe, H. A. & Heitler, W. 1934, Proc. Roy. Soc. A146, 83.

Blandford, R. D. & Cowie, L. L. 1982, ApJ 260, 625.

Blandford, R. D. & Ostriker, J. P. 1978, ApJ221L29

Blondin, J. M., Wright, E. B., Borkowski, K. J. & Reynolds, S. P. 1997, ApJ 500, 324.

Blumenthal, G. R. & Gould, R. J. 1970, Rev. Mod. Phys. 42, 237.

Brazier, K. T. S., et al., 1996, MNRAS 281, 1033.

Brazier, K. T. S., Reimer, O., Kanbach, G. & Carramiñana, A. 1998, MNRAS 295, 819.

Buckley, J. H. et al. 1997, A&A 329, 639.

Cargill, P. J. & Papadopoulos, K. 1988, ApJ 329, L29.

Chan, K.-W. & Lingenfelter, R. E. 1993, ApJ 405, 614.

Chevalier, R. A. 1977, ApJ 213, 52.

Chevalier, R. A. 1981, Fund. Cosmic Phys. 7, 1.

Chevalier, R. A. 1982, ApJ 258, 790.

Cioffi, D. F., McKee, C. F., & Bertschinger, E. 1988, ApJ 334, 252.

Claussen, M. J., Frail, D. A., Goss, W. M. & Gaume, R. A. 1997, ApJ 489, 143.

de Jager, O. C. & Baring, M. G. 1997, Proc. 4th Compton Symposium, ed. Dermer, C. D. & Kurfess, J. D. (AIP Conf. Proc. 410, New York), p. 171.

de Jager, O. C., & Mastichiadis, A. 1997, ApJ 482, 874.

Dermer, C. D. 1986a, ApJ 307, 47.

Dermer, C. D. 1986b, A&A 157, 223.

Draine, B. T. & McKee, C. F. 1993, Ann. Rev. Astron. Astrophys. 31, 373.

Drury, L. O'C. 1983, Rep. Prog. Phys. 46, 973.

Drury, L. O'C., Aharonian, F. A., & Völk, H. J. 1994, A&A 287, 959.

Drury, L. O'C., Markiewicz, W. J. & Völk, H. J. 1989, A&A 225, 179.

Drury, L. O'C., Duffy, P. & Kirk, J. G. 1996, A&A 309, 1002.

Eichler, D. 1984, ApJ 277, 429.

Ellison, D. C., Baring, M. G. & Jones, F. C. 1995, ApJ 453, 873.

Ellison, D. C., Baring, M. G. & Jones, F. C. 1996, ApJ 473, 1029.

Ellison, D. C., Drury, L. O'C., & Meyer, J.-P. 1997, ApJ 487, 197.

Ellison, D. C., & Eichler, D. 1984, ApJ 286, 691.

Ellison, D. C., Jones, F. C., & Eichler, D. 1981, J. Geophys. 50, 110.

Ellison, D. C., Jones, F. C., & Ramaty, R. 1990, Proc. 21st ICRC (Adelaide), 4, 68.

Ellison, D. C., Jones, F. C., & Reynolds, S. P. 1990, ApJ 360, 702.

Ellison, D. C., Möbius, E., & Paschmann, G. 1990, ApJ 352, 376.

Ellison, D. C., & Reynolds, S. P. 1991, ApJ 382, 242.

Elwert, G. 1939, Ann. Physik 34, 178.

Erickson, W. C., & Mahoney, M. J. 1985, ApJ 290, 596.

Esposito, J. A., Hunter, S. D., Kanbach, G. & Sreekumar, P. 1996, ApJ 461, 820.

Fedyushin, B. K. 1952, Zhur. Eksp. Teor. Fiz. 22, 140.

Feynman, R. P. 1969, Phys. Rev. Lett. 23, 1415.

Forman, M. A., and Morfill, G. 1979, in Proc. 16th ICRC (Kyoto) 5, 328.

Fulbright, M. S., & Reynolds, S. P. 1990, ApJ 357, 591.

Gaisser, T. K. 1990, Cosmic Rays and Particle Physics (Cambridge University Press, Cambridge)

Gaisser, T. K., Protheroe, R. J., & Stanev, T. 1998, ApJ 492, 219.

Galeev, A. A., Malkov, M. A. & Völk, H. J. 1995, J. Plasma Phys., 54(1), 59.

Garibyan, G. M. 1952, Zhur. Eksp. Teor. Fiz. 24, 617.

Giacalone, J., Burgess, D., Schwartz, S. J. and Ellison, D. C. 1992, Geophys. Res. Lett. 19, 433.

Green, D. A. 1986, MNRAS 221, 473.

Harrus, I. M., Hughes, J. P. & Helfand, D. J. 1996, ApJ 464, L161.

Haug, E. 1975, Z. Naturforsch. 30a, 1099.

Hess, M. 1997, Proc. 25th ICRC (Durban), 3, 229.

Higdon, J. C. & Lingenfelter, R. E. 1975, ApJ 198, L17.

Hofmann, W., et al. 1997, to appear in Towards a Major Atmospheric Čerenkov Detector, ed. O. C. de Jager (Wesprint, Pochefstroom).

Hoppe, M. M., et al. 1981, J. Geophys. Res. 86, 4471.

Huang, Y.-L. & Thaddeus, P. 1986, ApJ 309, 804.

Hunter, S. D., et al. 1997, ApJ 481, 205.

Jauch, M. M. & Rohrlich, F. 1980, The Theory of Photons and Electrons, (2nd edn. Springer, Berlin)

Jokipii, J. R. 1987, ApJ 313, 842.

Jones, F. C. 1968, Phys. Rev. 167, 1159.

Jones, F. C. 1971, ApJ 169, 503.

Jones, F. C. & Ellison, D. C. 1991, Space Sci. Rev. 58, 259.

Jun, B.-I. & Norman, M. L. 1996, ApJ 465, 800.

Kaaret, P. & Cottam, J. 1996, ApJ 462, L35.

Kang, H., & Jones, T. W. 1991, MNRAS 249, 439.

Keohane, J. W., Petre, R., Gotthelf, E. V., Ozaki, M., & Koyama, K. 1997, ApJ 484, 350.

Kirk, J. G., Duffy, P. & Ball, L. 1995, A&A 293, L37.

Koyama, K. et al. 1995, Nature 378, 255.

Lagage, P. O., & Cesarsky, C. J. 1983, A&A 125, 249.

Lang, K. R. 1980, Astrophysical Formulae, (Springer-Verlag, Berlin)

Lee, M. A. 1982, J. Geophys. Res. 87, 5063.

Lessard, R. W., et al. 1995, Proc. 24th ICRC (Rome) 2, 475.

Levinson, A. 1992, ApJ 401, 73.

Levinson, A. 1996, MNRAS 278, 1018.

Lorenz, E. 1997, Proc. 25th ICRC (Durban), 5, 177.

Lozinskaya, T. A. 1992, Supernovae and Stellar Wind in the Interstellar Medium (AIP, New York)

Malkov, M. A. 1997, ApJ 485, 638.

Malkov, M. A. & Völk, H. J. 1995, A&A 300, 605.

Markiewicz, W. J., Drury, L. O'C. & Völk, H. J. 1990, A&A 236, 487.

Mason, G. M., Gloeckler, G., and Hovestadt, D. 1983, ApJ 267, 844.

Mastichiadis, A. 1996, A&A 305, L53.

Mastichiadis, A., & de Jager, O. C. 1996, A&A 311, L5.

McKenzie, J. F. & Völk, H. J. 1984, A&A 116, 191.

Merck, M., et al. 1996, A&AS 120C, 465.

Meyer, J.-P., Drury, L. O'C., & Ellison, D. C. 1997, ApJ 487, 182.

Moffett, D.A., Goss, W.M., & Reynolds, S.P. 1993, AJ, 106, 1566

Moussas, X., et al. 1992, Sol. Phys. 140, 161.

Müller, D., et al. 1995, Proc. 24th ICRC (Rome), 3, 13.

Mukherjee, R., Grenier, I. A., & Thompson, D. J. 1997, Proc. 4th Compton Symposium, ed. Dermer, C. D. & Kurfess, J. D. (AIP Conf. Proc. 410, New York), p. 394.

Naito, T. & Takahara, F. 1994, J. Phys. G: Nucl. Part. Phys. 20, 477.

Orth, C. D. & Buffington, A. 1976, ApJ 206, 312.

Pacholczyk, A. G. 1970, Radio Astrophysics (Freeman, San Francisco)

Pohl, M. 1996, A&A 307, L57.

Pollock, A. M. T. 1985, A&A 150, 339.

Prosch, C., et al. 1995, Proc. 24th ICRC (Rome), 2, 405.

Prosch, C., et al. 1996, A&A 314, 275.

Reynolds, S. P. 1982, ApJ 256, 38.

Reynolds, S. P. 1995, Proc. 24th ICRC (Rome), 2, 17.

Reynolds, S. P. 1996, ApJ 459, L13.

Reynolds, S. P. 1998, ApJ 493, 375.

Reynolds, S. P., & Ellison, D. C. 1992, ApJ 399, L75.

Reynolds, S. P. & Gilmore, D. M. 1993, AJ 106, 272.

Rivoal, M. 1997, Proc. 25th ICRC (Durban), 5, 89.

Rybicki, G. B. & Lightman, A. P. 1979, Radiative Processes in Astrophysics (Wiley, New York).

Sedov, L. 1959, Similarity and Dimensional Methods in Mechanics (New York: Academic).

Shu, F. H. 1992, The Physics of Astrophysics, II: Gas Dynamics (University Science Books: Mill Valley)

Stecker, F. W. 1971, Cosmic Gamma Rays, NASA SP-249 (NASA, Washington)

Stöstrand, T., & van Zijl, M. 1987, Phys. Rev. D 36, 2019.

Sturner, S. J., & Dermer, C. D. 1995, A&A 293, L17.

Sturner, S. J., Skibo, J. G., Dermer, C. D., & Mattox, J. R. 1997, ApJ 490, 619.

Tan, L. C. & Ng, L. K. 1983, J. Phys. G. Nucl. Phys. 9, 1289.

Tanimori, T., et al. 1997, IAU Circ. 6706.

Tanimori, T., et al. 1998, ApJ 497, L25.

Thompson, D. J. et al. 1995, ApJS 101, 259.

Tsurutani, B. T., Smith, E. J., and Jones, D. E. 1983, J. Geophys. Res. 88, 5645.

Wang, Z. R., et al. 1992, PASJ 44, 303.

Weekes, T. C., et al. 1997, Proc. 25th ICRC (Durban), 5, 173.

Yadigaroglu, I. A. & Romani, R. W. 1997, ApJ 476, 347.

Zimmermann, H. U., Trümper, J. E., & Yorke, H. 1996, Röntgenstrahlung from the Universe, MPE Report 263 (Max-Planck-Institut für Extraterrestrische Physik, Garching)

This preprint was prepared with the AAS LaTeX macros v4.0.

TABLE 1

PARAMETERS FOR EVOLUTIONARY AND COSMIC RAY EXAMPLES

Parameters	Model a	Model b	Model c	Model d	Model e
$\mathcal{E}_{SN}$ [10^{51} erg]	1	1	1	10	1
M_{ej} [$M_\odot$]	1	1	1	10	1
$n_{p,1}$ [cm^{-3}]	1	1	1	10^{-3}	0.3
B_1 [μG]	3	3	3	10	3
η	10	10	10	1	10
t_{SNR} [yr]	300	1000	1×10^4	4×10^4	5000
V_{sk} [km s^{-1}]	4000	2000	490	1340	940
R_{sk} [pc]	3	5	12.5	140	12
r	20	17	11	6.5	11
r_{sub} [a]	2.73	2.68	2.54	4.43	2.65
E_{crit} [keV]	100	100	100	0	0
f_e	1	1	1	0.05	1
$T_{e,inj}$ [K]	4.8×10^6	1.5×10^6	1.9×10^5	1.0×10^6	8×10^5
$(e/p)_{10GeV}$	0.044	0.11	0.13	0.02	0.03
d_{FEB} [ηr_{g1}]	5.8×10^6	4.4×10^7	5.7×10^8	7.2×10^{10}	2.8×10^8
d_{FEB} [pc]	0.26	0.97	3.1	33	3
E_{max} [TeV]	2.9	5.2	4.2	4.1×10^3	8

NOTE.— (a) The subshock compression ratio, r_{sub}, is determined by $r_{sub} = u(x = -1\,\eta\, r_{g1})/V_{sk}$.

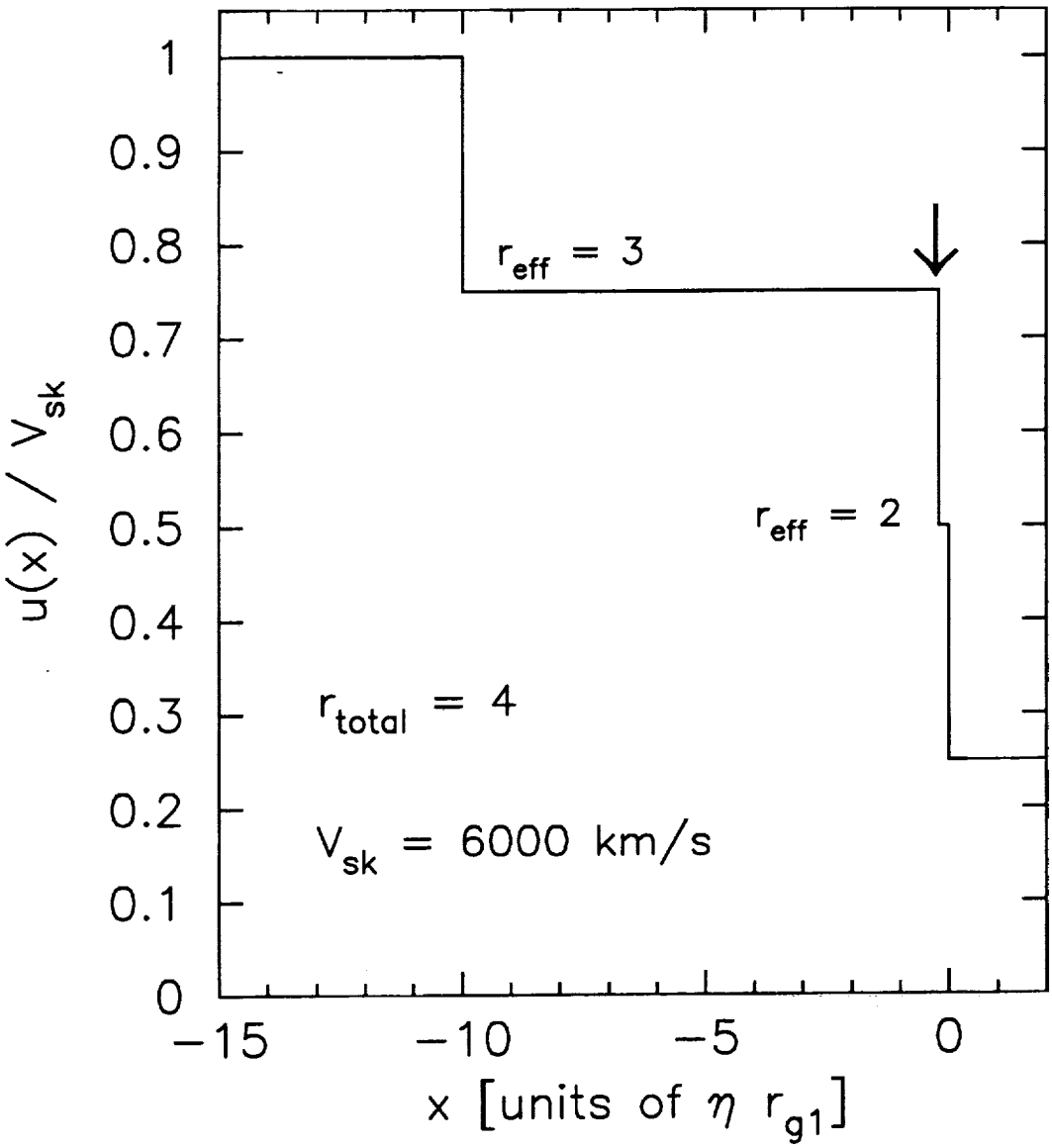

Fig. 1.— A schematic depiction of a non-linear shock profile, which shows the flow speed versus distance normal to the shock in its rest frame. This artificial shock profile has an overall compression ratio of $r_{\rm total} = 4$ and two subshocks with $r_{\rm eff} = 3$ at $x = -10\,\eta r_{\rm g1}$ and $r_{\rm eff} = 2$ at $x = -0.2\,\eta r_{\rm g1}$. The shock speed is $V_{\rm sk} = 6000$ km s^{-1}, which just acts as a scale to the system. The arrow indicates the minimum upstream diffusion length for the $p_{\rm crit} = 1.5 \times 10^{-3}\, m_{\rm p} c$ electron example shown with the dotted line in Figure 2. All electrons from injection energies upward diffuse farther upstream that $-0.2\,\eta r_{\rm g1}$ for this example.

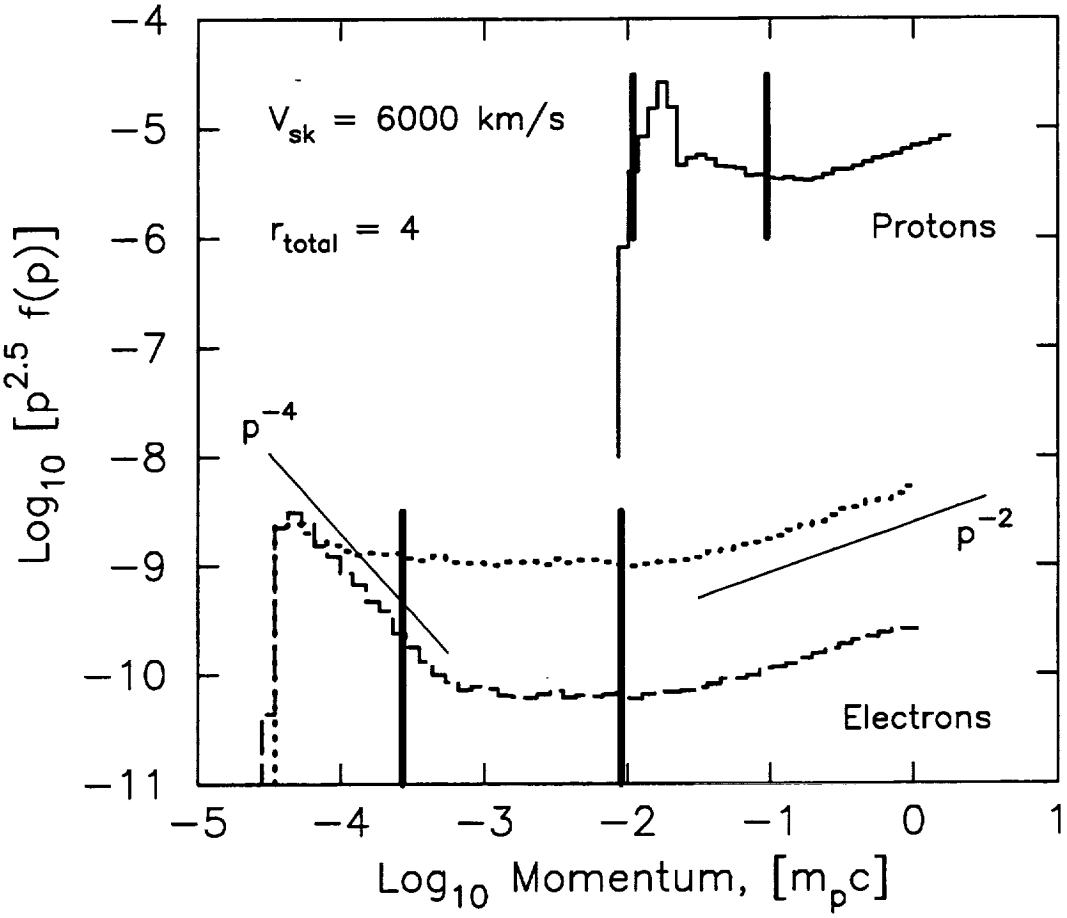

Fig. 2.— The number density in scalar momentum space, $f(|\mathbf{p}|)$, versus $|\mathbf{p}|$. We have plotted $|\mathbf{p}|^{2.5} f(|\mathbf{p}|)$ to flatten the spectra. The momentum is in units of $m_p c$. The upper solid curve is the proton spectrum, while the two lower curves are electron spectra. The dashed electron curve results from $p_{crit} = 0$, while the dotted curve results from $p_{crit} = 1.5 \times 10^{-3} m_p c$, for which e^- injection is more efficient. In all cases, particles are injected at the shock with a δ-function distribution at 1 keV. The heavy vertical lines indicate the momenta corresponding to upstream diffusion lengths, $-L_D = -0.2\,\eta r_{g1}$ and $-10\,\eta r_{g1}$. The slopes of the power-law portions reflect those obtained from equation (4) with the values of r_{eff} in Figure 1.

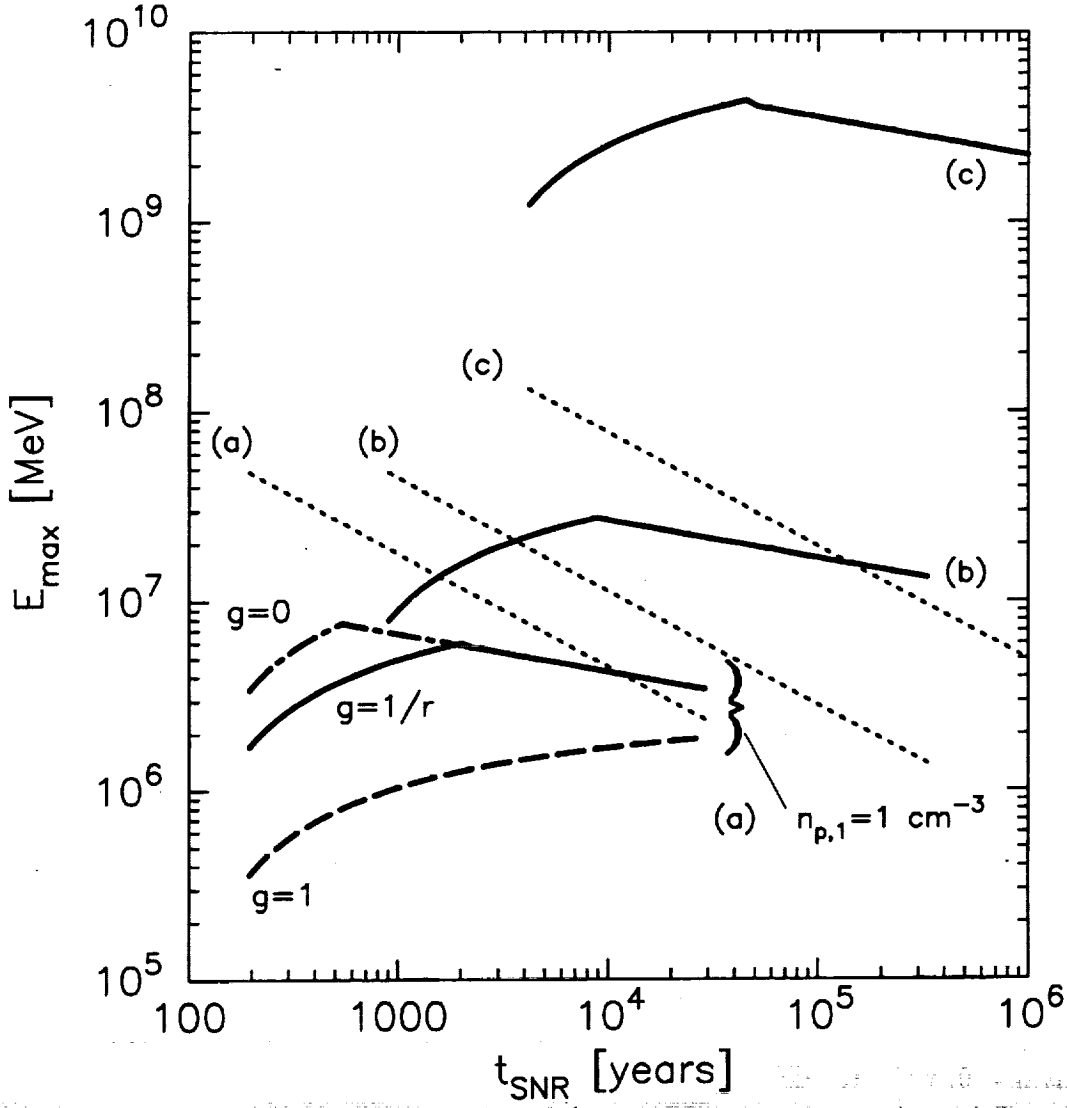

Fig. 3.— Estimates of maximum particle energy during the Sedov phase versus SNR age, $t_{\rm SNR}$. The lower three heavy curves (a) are calculated with $n_{\rm p,1} = 1$ cm^{-3} using $g = 0$ (dot-dashed curve, corresponding to no time spent downstream), $g = 1/r \simeq 0.12$ (solid curve), and $g = 1$ (dashed curve). The heavy curve labeled (b) uses $n_{\rm p,1} = 0.01$ cm^{-3} with $g = 1/r$. The upper most heavy curve has parameters chosen to obtain a high maximum energy. The light dotted lines show the maximum energy versus SNR age electrons will obtain under the influence of synchrotron and inverse Compton losses; see equation (23). The light dotted line at the lower left applies to the lower three heavy curves (a), the middle light dotted line applies to the middle heavy solid line (b), and the rightmost light dotted line applies to the top solid line (c).

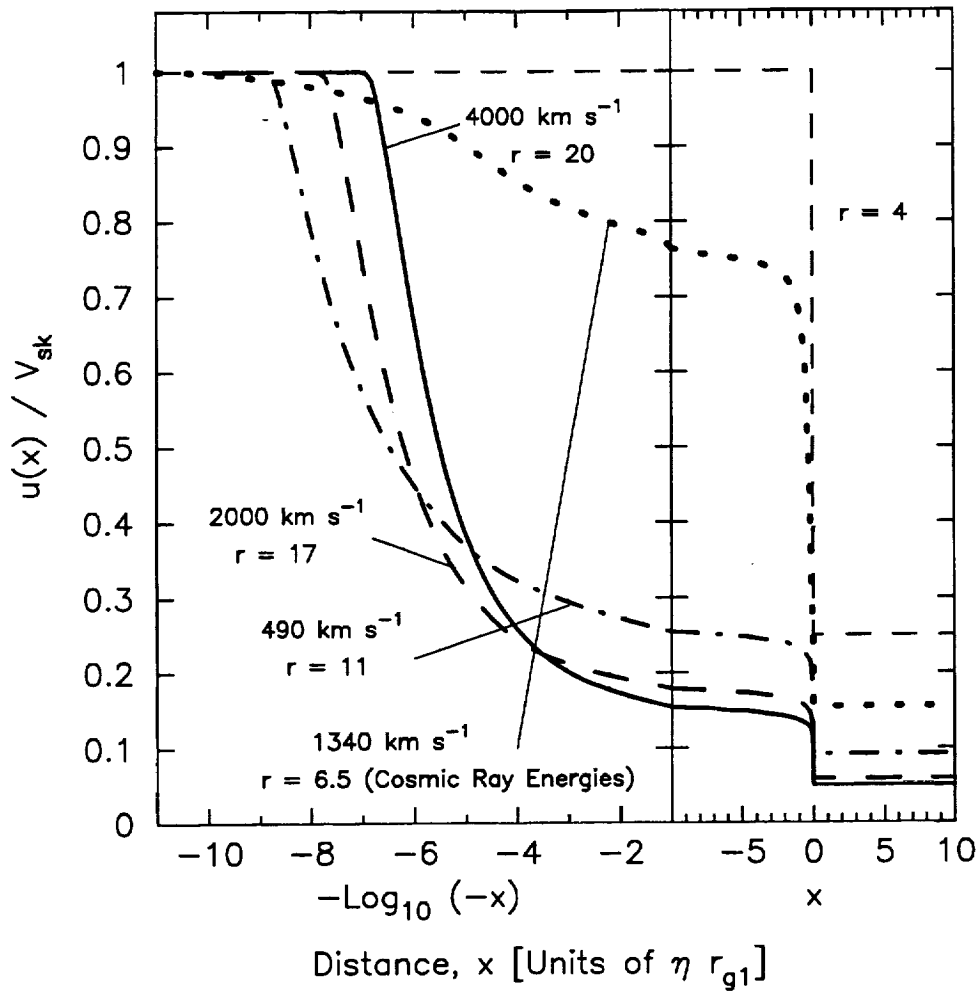

Fig. 4.— The bulk flow speed versus distance (i.e. shock velocity profile), obtained in the Monte Carlo simulation. Three of the four profiles correspond to Sedov evolution of a remnant's shock with given ISM parameters, namely $n_{\rm p,1} = 1$ cm^{-3}, $B_1 = 3\mu$G, and with $\eta = 10$ and $g = 1/r$. These comprise the heavy solid curve (Model *a* in Table 1, with $r = 20$), the heavy dashed curve (Model *b* in Table 1; $r = 17$), and the heavy dot-dashed curve (Model *c* in Table 1; $r = 11$). The shock weakens slightly with time, and for comparison, we depict a standard linear (test-particle) strong shock profile with a compression ratio $r = 4$ as the light dashed step-function. As a separate example, the heavy dotted curve shows the structure for a shock capable of accelerating particles to the cosmic ray "knee" at $\sim 10^{15}$ eV (Model *d* in Table 1), with different ISM parameters. In first three examples, a distinct subshock exists with a compression ratio $r_{\rm sub} \sim 2.5$. The cosmic ray energy shock (dotted line), however, has a much stronger subshock ($r_{\rm sub} \sim 4.4$) due to the strong Alfvén wave heating in the precursor. Notice that the distance is plotted with a logarithmic scale for $x < -10\,\eta r_{\rm g1}$ and a linear scale for $x > -10\,\eta r_{\rm g1}$.

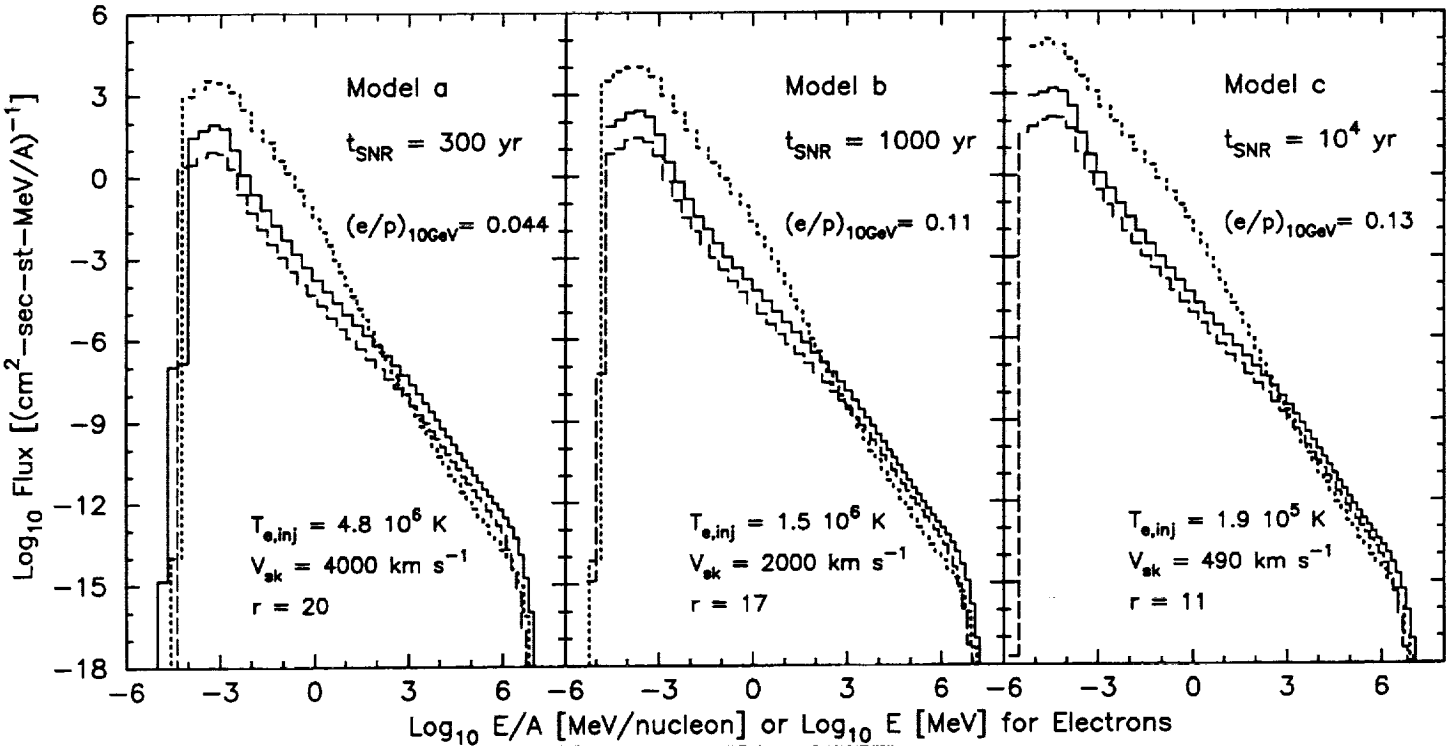

Fig. 5.— Particle omni-directional fluxes, dJ/dE [particles/(cm^2-s-ster-MeV/A)], versus energy per nucleon for ions and versus energy for electrons ($A \equiv 1$ for electrons), obtained from our example of an expanding remnant in the Sedov phase (see Table 1 for model parameters). All spectra are calculated downstream from the shock in the shock rest frame and are obtained as explained in the text with a steady-state approximation. In each panel, the solid and dashed lines show the hydrogen and He^{+2} spectra, respectively, and the dotted line shows the electron spectrum. Both ionic species contribute to the shock smoothing and the far upstream number density of helium is 1/10 that of hydrogen. The curves are normalized such that $V_{sk} n_{p,1} = 1$ cm^{-2} s^{-1}. The electron spectra are obtained with $E_{crit} = 100$ keV and $f_e = 1$. As the remnant evolves, the shock slows and weakens, and the injected electron temperature $T_{e,inj}$ diminishes in accordance with the decline in the dissipative heating of ions (for fixed f_e) in the shock layer.

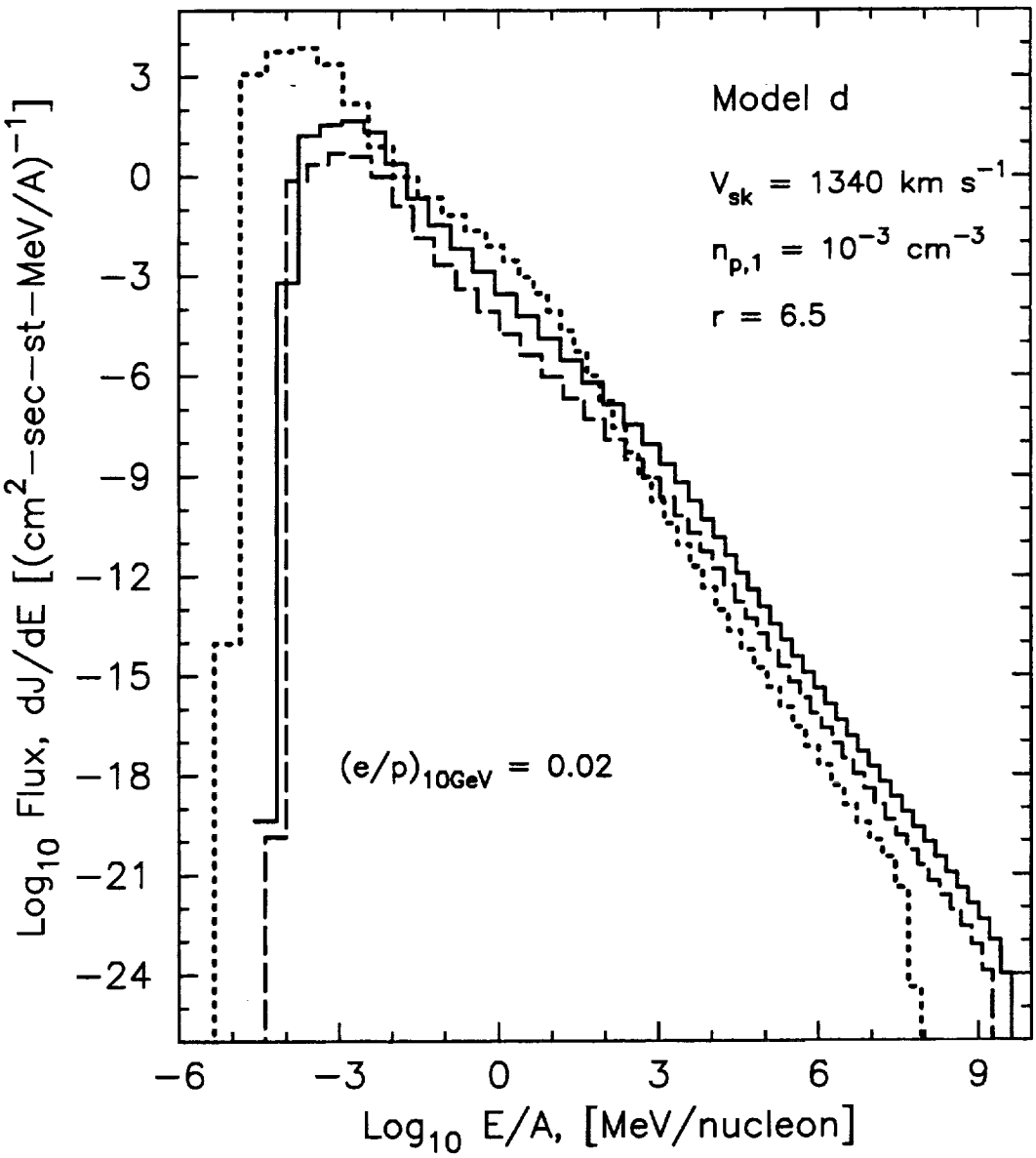

Fig. 6.— Particle spectra, dJ/dE [particles/(cm^2-s-ster-MeV/A)], versus energy per nucleon for ions (or energy for electrons with $A \equiv 1$). The solid line is the proton spectrum, the dashed line is the He^{2+} spectrum, the dotted line is the electron spectrum, and all spectra are calculated downstream from the shock in the shock rest frame. The parameters (i.e. Model *d*) have been chosen to produce particles with energies above 10^{15} eV to account for cosmic rays up to the knee. The electron spectrum cuts off at lower energies than the proton or helium because of significant synchrotron and inverse Compton losses (see Figure 3).

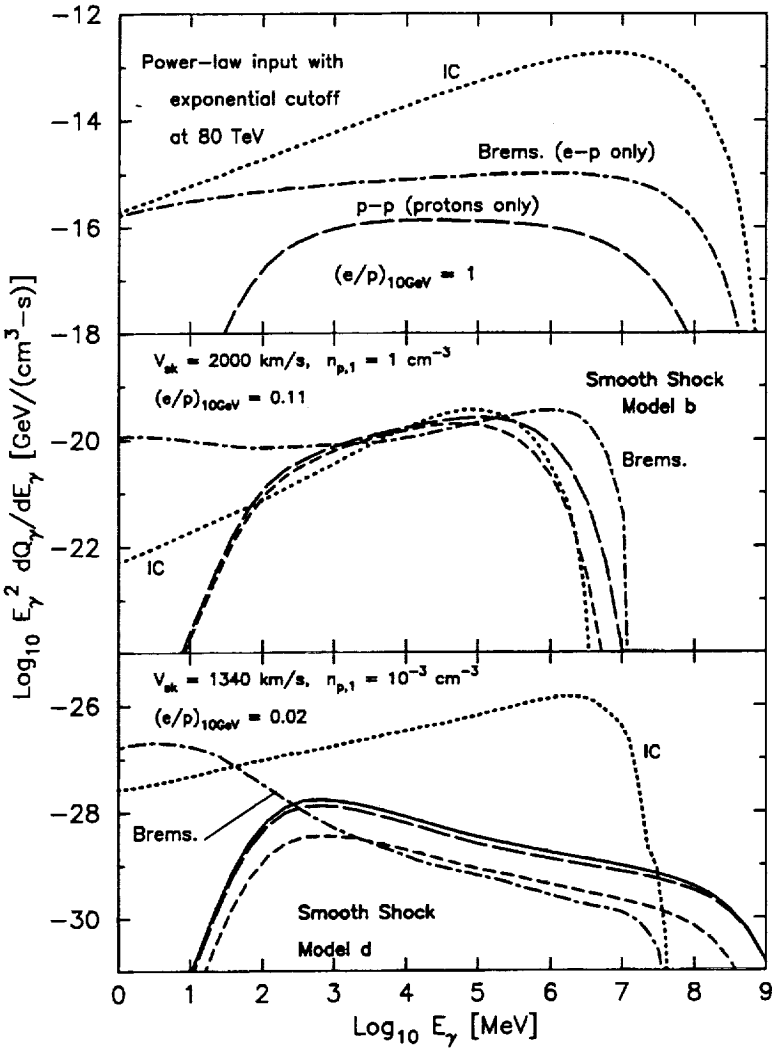

Fig. 7.— Examples of photon emission spectra, plotted as $E_\gamma^2 \, dn_\gamma(E_\gamma)/dt$ to emphasize the peak power of emission. The top panel is produced using power-law electron and ion spectra with identical normalization to that used in Figure 3 of Gaisser, Protheroe, & Stanev (1998). These "template" curves reproduce their results quite well, with small differences in the pion decay emission (p-p) and e-p bremsstrahlung due to different assumptions in modeling these components. The bottom two panels depict sample photon spectra produced by our self-consistent shock-accelerated electron and ion (proton and He^{2+}) distributions. The middle panel is Model *b* of our evolving remnant trio, and the bottom panel is Model *d*, which produces cosmic rays up to the knee. Comparison of these two models indicates that density and other changes can strongly influence the relative importance of inverse Compton scattering versus bremsstrahlung and pion decay radiation. In all panels, dotted lines are inverse Compton (IC), dot-dashed lines are bremsstrahlung, long-dashed lines are pion-decay from protons, short-dashed lines are pion-decay from helium, and the solid line in the bottom panel is the total pion-decay emission.

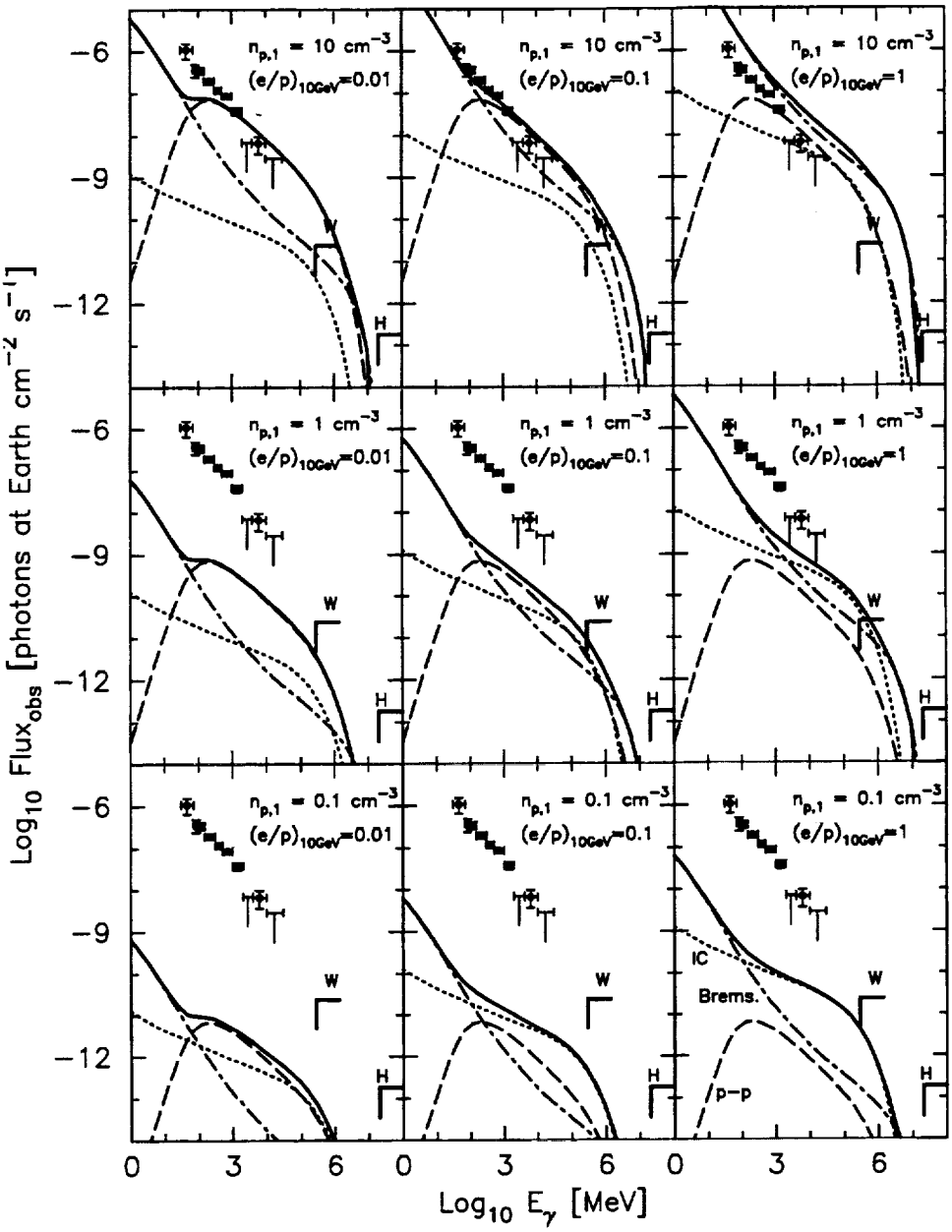

Fig. 8.— An array of emission spectra generated from Model *e* (Table 1), illustrating trends in the parameters $n_{p,1}$ and $(e/p)_{10GeV}$; these are compared with observations of the shell remnant IC 443. The data points are from EGRET observations of 2EG J0618+2234 (Esposito et al. 1996), and the upper limits are from the Whipple imaging telescope (Buckley et al. 1997) and the HEGRA *array* (Prosch et al. 1995) as marked. In all panels, dotted lines are inverse Compton, dot-dashed lines are bremsstrahlung, dashed lines are the total pion-decay emission from protons and helium (denoted hereafter by p-p), and solid lines are the sums of the three components. The model spectra are normalized to a source at 1 kpc with emission volume = 1 pc^3.

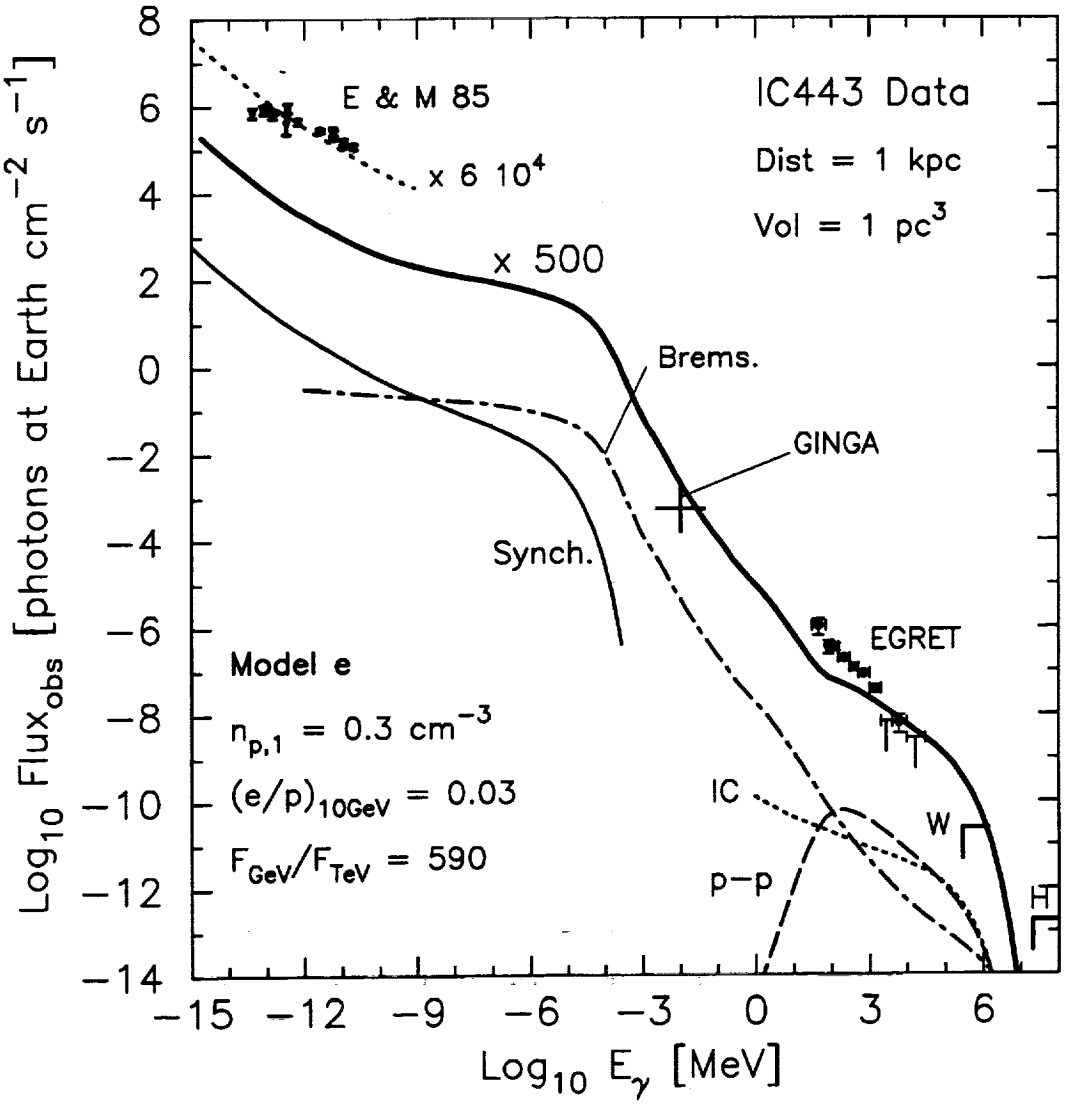

Fig. 9.— Photon spectra for the various emission processes (pion decay from p-p, p-He, *and* He-He collisions [denoted by p-p], bremsstrahlung, inverse Compton, and synchrotron radiation, as labelled, with the same line styles as in Figure 8) for our $n_{p,1} = 0.3$ cm^{-3} Model *e* used to generate the examples in Figure 8. The component spectra are all normalized to a source at 1 kpc with emission volume = 1 pc^3, but the total spectrum (heavy solid line) is multiplied by 500 to roughly match the EGRET flux. Whipple (W) and HEGRA (H) upper limits are referenced in the text and in Figure 8. The Ginga data point is from Wang et al. (1992) and the radio data (labelled E & M 85) are from Erickson & Mahoney (1985). The GeV/TeV flux ratio $F_{\rm GeV}/F_{\rm TeV} = 590$ obtained in this model is slightly lower than that expected for an E_γ^{-1} *flux* power-law due to the prominence of the IC contribution.

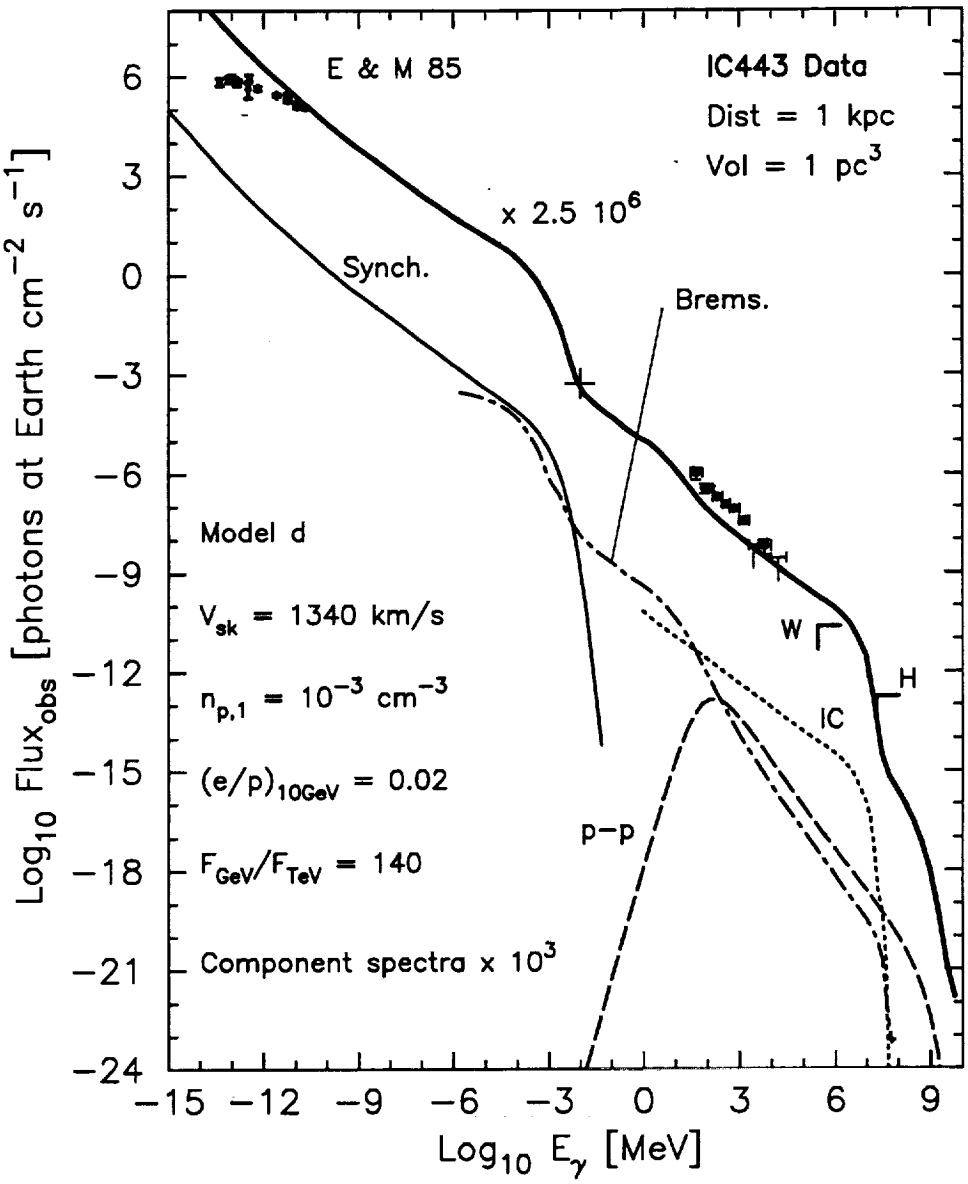

Fig. 10.— Photon spectra for our model producing cosmic rays up to the "knee" (i.e. Figure 6). The line styles for the various component spectra are as in Figure 9, as are the data. The component curves are all normalized to 1000 times a source at 1 kpc with emission volume = 1 pc^3, but the total spectrum (heavy solid line) is multiplied by 2.5×10^6 (bottom panel) to give fluxes more-or-less comparable to the EGRET levels for IC 443. Note that since the density is very low in this example, in order to give a high E_{max}, the inverse Compton component is very prominent, yielding a low F_{GeV}/F_{TeV} flux ratio. As in Figure 9, the p-p pion decay spectrum includes contributions from p-He and He-He collisions.

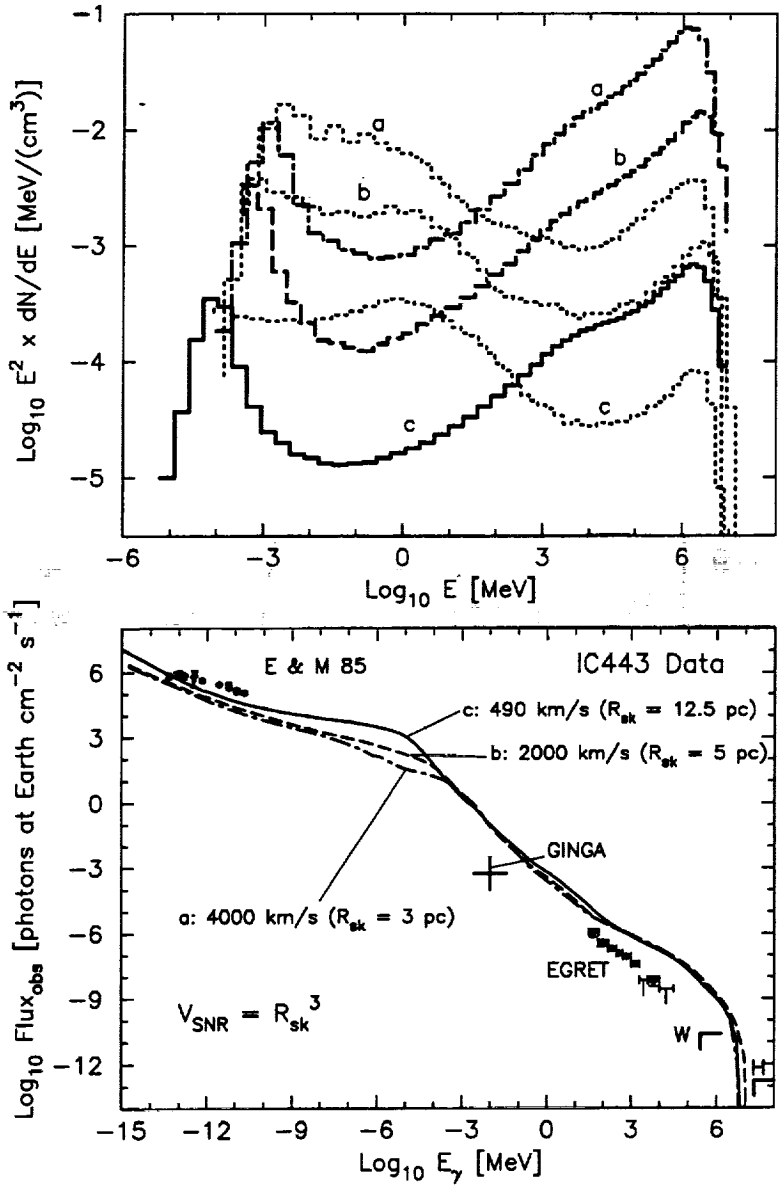

Fig. 11.— The evolutionary sequence corresponding to three of the profiles in Figure 4, and the particle distributions in Figure 5 (i.e. Models *a*, *b*, and *c*). The top panel shows the same proton (solid, dashed, and dash-dot histograms) and electron (dotted histograms) spectra shown in Figure 5, but multiplied by E^2 to illustrate that the maximum energy density is in the highest energy protons. The bottom panel shows the total photon emission (i.e. the sum of the bremsstrahlung, inverse Compton, pion decay, and synchrotron emission) for these models with a source volume, $V_{\rm SNR} = R_{\rm sk}^3$ (for each time) and a source distance $d = 1\,{\rm kpc}$. This illustrates a property, probably the consequence of Sedov evolution of a SNR, that the X-ray to hard gamma-ray photon spectra are virtually independent of time between 300 and 10,000 years of age.